

Systematic Studies on Structural and Optical Properties of Organic Thin Films on Inorganic Substrates

Von der Fakultät für Mathematik, Informatik und Naturwissenschaften
der Rheinisch-Westfälischen Technischen Hochschule Aachen
zur Erlangung des akademischen Grades einer
Doktorin der Naturwissenschaften genehmigte Dissertation

vorgelegt von

M.Sc. Azadeh Farahzadi
aus Ray, Iran

Berichter: Universitätsprofessor Dr. Matthias Wuttig
Universitätsprofessor Dr. Stefan Blügel

Tag der mündlichen Prüfung: 1.Oktober.2007

Diese Dissertation ist auf den Internetseiten der Hochschulbibliothek online verfügbar.

*To my parents, Behjat Golara and Hossein Farahzadi
who instilled in me the love of learning*

Abstract

Molecular organic compounds are employed as active materials in a variety of applications, including organic light emitting diodes (OLEDs) and organic thin film transistor (OTFTs). These devices consisting of sequentially deposited layers of organic materials have been demonstrated with active device thicknesses of only a few hundred nanometers or less. For a better understanding and design of such devices, it is necessary to understand the structural and optical properties of the organic thin films employed.

Polymers based on the family of five-membered thiophene conjugated ring and its derivatives, due to their self-assembling nature, have been considered as one of the most common conducting organic polymers used in OTFT devices. We have studied the adsorption of 3-nitrothiophene/selenophen/tellurophen on Cu(110) surface, utilising *ab initio* calculations. These calculations provide a basic understanding and forecasting of intra- and inter-molecular interactions present in the observed structures. Monolayers of 3-nitrothiophen/selenophen/tellurophen on a Cu(110) surface are well ordered with the aromatic ring perpendicular to the surface, in a close packed structure. Due to the strong lateral interaction between the hydrogen atoms of the neighboring conjugated rings, they rotate relative to the nitro ($-NO_2$) group.

Tris-(8-hydroxyquinoline) aluminum (Alq_3) and N,N'-diphenyl-N,N'-bis(1-naphthyl)-1-1'-biphenyl-4,4''-diamine (α -NPD) are among the most commonly used electron-transport and hole-transport materials suitable for OLED applications. The optical and structural properties of the thin films of these materials deposited by organic vapor phase deposition (OVPD) have been studied by spectroscopic ellipsometry (SE). Employing this technique enables the precise determination of the dielectric function as well as thickness of the organic thin films of each material. This result can be explained by the characteristic features of electronic states in organic molecules.

In order to tailor and modify thin film properties to be suitable for desired applications, e.g. organic light emitting devices (OLED) in this case, it is necessary to study and understand the influence of deposition parameters on thin film growth. Our study is focused on the influence of deposition rate and substrate temperature on (α -NPD) film morphology. A remarkable dependence of the film morphology on deposition rate and substrate temperature is observed. A detailed quantitative morphology analysis provides an excellent description of the growth mechanism of OLED films.

Kurzfassung

Molekulare organische Verbindungen werden als aktive Materialien in einer Vielzahl unterschiedlicher Anwendungen, einschließlich der organischen Leuchtdioden (OLEDs) und organischen Dünnschichttransistoren (OTFTs) eingesetzt. Diese Bauelemente, bestehend aus aufeinanderfolgenden Schichten organischer Materialien, wurden mit aktiven Filmen, die eine Dicke von nur einigen hundert Nanometer oder weniger aufweisen demonstriert. Für das bessere Verständnis und das Design solch einer Anordnung ist es erforderlich die Struktur und die optischen Eigenschaften der bestehenden organischen Schichten zu verstehen.

Polymere, basierend auf die Familien der fünfgliedrigen Thiophene gepaarten Ringe und deren Derivate, werden aufgrund der Natur ihres Eigenaufbaus als eins der häufigsten allgemein behandelten leitfähigen organischen Polymere betrachtet, die in OTFT Anordnungen verwendet werden. Wir haben die Adsorption von 3-nitrothiophene/selenophen/tellurophen auf Kupfer (110) Oberflächen mit der *ab initio* untersucht. Diese Kalkulationen bieten das Basisverständnis und eine Vorausberechnung der intra- und-intermolekulare Wechselwirkungen die in den beobachteten Strukturen bestehen. Monolagen von 3-nitrothiophene/selenophen/tellurophen auf Kupfer(110) Oberflächen sind mit dem aromatischen Ring senkrecht zur Oberfläche gut in einer dicht gepackten Struktur angeordnet. Wegen der starken lateralen Wechselwirkung zwischen den Wasserstoff Atomen der benachbarten konjugierten Ringe, rotieren sie relative zu der Nitro (-NO₂) Gruppe.

Tris-(8-hydroxyquinoline) aluminum (*Alq₃*) und N,N'-diphenyl-N,N'-bis(1-naphthyl)-1-1'-biphenyl-4,4'-diamine (*α-NPD*) sind unter den meisten üblich verwendeten Elektron-Transport und Loch-Transport Materialien für OLED Anwendungen geeignet. Die optischen und strukturellen Eigenschaften dieser dünnen in der organische Gasphaseabscheidung (OVPD) hergestellten Schichten wurde mit der spektroskopischen Ellipsometrie (SE) untersucht. Das Einsetzen dieser Technik ermöglicht die präzise Bestimmung der dielektrischen Funktion ebenso wie der Dicke der organischen Dünnschichten jedes Materials. Dieses Ergebnis kann durch die charakteristische Eigenschaft der elektronischen Zustände in organischen Molekülen erklärt werden.

Für das Maßschneidern und Modifizieren der Dünnschichteigenschaften, um sie für Anwendungs- zwecke, in diesm Fall beispielsweise organische Leuchtdioden (OLED) ist es erforderlich den Einfluss der Dipositionsparameter auf das Dünnschichtwachstum zu untersuchen. Unsere Untersuchung ist auf den Einfluss der Depositionsrate und der Substrattemperatur auf die (*α-NPD*) Schichtmorphologie fokussiert. Es wurde eine bemerkenswert Abhängigkeit der Schichtmorphologie auf Ablagerungsraten und der Substrattemperatur beobachtet. Eine detaillierte quantitative Analyse der Morphology bietet eine ausgezeichnete Beschreibung der Wachstumsmechanismen der OLED Schichten.

Contents

Abstract	V
Kurzfassung	VI
1 Introduction	1
2 First-principles methods	5
2.1 Density functional theory	6
2.1.1 Hohenberg-Kohn theorem	6
2.1.2 The Kohn-Sham formalism	7
2.1.3 Exchange-correlation approximations: LDA and GGA	10
2.1.4 Spin-density functional theory	11
2.2 Density functional theory in a plane wave implementation	12
2.2.1 Periodic supercells	12
2.2.2 Bloch's Theorem	13
2.2.3 k-point sampling	13
2.2.4 Plane-wave basis sets	14
2.3 The pseudopotentials	14
2.3.1 Norm-conserving pseudopotentials	16
2.3.2 Semi-local pseudopotentials and Kleinman-Bylander factorization . .	16
2.3.3 The PAW pseudopotentials	18
3 The EStCoMPP-program	21
3.1 Minimization of the energy functional	21
3.2 Explicit form of the equations	22
3.2.1 The kinetic energy	24
3.2.2 The local energy	24
3.2.3 The non-local part of the energy	26
3.2.4 The Ewald-energy	28
3.2.5 The Hellman-Feynman forces	28
3.3 The loop-structure and the algorithms	30
3.3.1 Iterative Eigenvalue Determination	30
3.3.2 The electronic self-consistency and molecular relaxation loops . . .	32

4	3-nitrothiophene/selenophen/ tellurophen on Cu(110)	33
4.1	Introduction	33
4.2	Free molecules in the gas phase	34
4.2.1	Structure optimization	35
4.3	Adsorption of the molecules on the surface	36
4.3.1	Rotation angle for conjugated rings: selenophen and tellurophen . .	38
4.3.2	Full relaxation of 3-nitrothiophene/selenophen/tellurophen on Cu(110) surface	39
4.4	Anchoring groups nitro versus carboxylate	41
4.5	Summary and conclusions	44
5	Optical properties of organic materials	47
5.1	Different organic compounds	48
5.1.1	Electronic states in conjugated molecules	48
5.2	Electrons in a radiation field	52
5.2.1	Band-to-band optical transitions	53
5.2.2	Connection with the optical constants	55
5.2.3	Indirect band-to-band transitions: general remarks on electron- phonon interaction	57
5.2.4	The Franck-Condon principle	60
5.2.5	Electron-phonon coupling	63
5.3	Exciton effect	65
5.3.1	The concept of excitons	65
5.3.2	Free excitons	66
5.3.3	Frenkel tightly bound excitons	67
5.3.4	Molecular crystals and organic thin films	69
5.4	Optical response of conjugated polymers	70
6	Scientific instruments	73
6.1	Organic vapor phase deposition (OVPD)	73
6.2	Atomic force microscopy (AFM)	75
6.3	X-ray-reflectometry (XRR)	77
6.4	Spectroscopic Ellipsometry (SE)	80
7	Optical properties of organic films of Alq_3 and α-NPD	83
7.1	Introduction	83
7.2	Experiments	84
7.2.1	Spectroscopic ellipsometry measurements	84
7.2.2	XRR and AFM measurements	85
7.3	Results and discussions	86
7.4	Conclusions	92

8	The theory of thin film growth	95
8.1	General concepts of thin film growth	95
8.1.1	Surface free energy	95
8.1.2	Microscopic processes	96
8.2	Quantitative parameters	98
8.2.1	Surface roughness	99
8.2.2	Lateral correlation length	100
8.2.3	Scaling concepts and critical exponents	101
8.3	Different growth models	102
8.3.1	Random deposition	103
8.3.2	Linear theory	104
8.3.3	Nonlinear models	105
8.3.4	Diffusive growth	109
8.3.5	Raible's model for amorphous growth	110
8.4	Quantifying deterministic and random influences on the surface morphology	112
8.4.1	The Markov nature of height fluctuations	113
8.4.2	Governing equation of height fluctuations	113
9	Growth and morphology of α-NPD amorphous thin films	115
9.1	Introduction	115
9.2	Experiments	116
9.3	Results and discussions	116
9.3.1	Quantitative analysis	116
9.3.2	Initial stages of growth	122
9.4	Conclusion and outlook	123
10	Summary and outlook	125
	List of figures	131
	List of tables	133
	Bibliography	141
	Acknowledgements	143
	Curriculum Vitae	145

1 Introduction

During the last decades, organic materials have received considerable attention as potential replacement for their inorganic counterparts in applications such as organic light emitting devices (OLEDs) and organic thin film transistors (OTFTs). Organic materials have the key advantage of simple and low temperature thin film processing and low cost of production. In addition, the flexibility of organic chemistry enables the formation of organic molecules with useful luminescent and conducting properties. [1] Since the first consideration of organic electroluminescence (EL) devices more than 30 years ago [2], organic light-emitting devices (OLEDs) have been widely pursued, and commercial dot-matrix displays have recently been demonstrated [3]. Luminous efficiencies in excess of 30 lm/W and operating voltages as low as 4 V have been reported. [4], [5] In addition to emitting light, the semiconducting properties of some organic materials enable promising technologies for organic field-effect transistors (OFETs). Over the last few years, the carrier mobilities of organic channel layers in OFETs have increased dramatically from 10^{-4} to $1\text{ cm}^2/\text{Vs}$ (comparable to those of amorphous silicon, $1\text{ cm}^2/\text{Vs}$) [6], [7].

Thin films of organic materials are commonly deposited on inorganic surfaces. Such composites, represent a new class of materials that may combine desirable physical properties characteristic of both organic and inorganic components within a single system. Inorganic materials offer the potential for a wide range of electronic properties (enabling the design of insulators, semiconductors, and metals), magnetic and dielectric transitions, substantial mechanical hardness, and thermal stability. Organic molecules, on the other hand, can provide high fluorescence efficiency, large polarizability, plastic mechanical properties, ease of processing, and structural diversity.

The optical and structural properties of organic materials are different from those of the inorganic ones. In contrast to the strong covalent or ionic bonds in inorganic materials, organic molecules are bound to each other by the relatively weak *van der Waals* forces. Conjugated organic molecules, the most interesting class of organic compounds, have the electronic structure based on the π orbitals between the carbon atoms. These electronic states, which are delocalized in the whole molecule, govern the structural as well as the opto-electronical behavior of the materials. Furthermore, in the electronic excitation of organic molecules, the tightly bound excitonic states, i.e. the Frenkel excitons, play an important role. These excitonic states are strongly coupled with the vibrational modes of organic solids. This electron-phonon coupling has a significant effect on the opto-electronic behavior of organic materials. [8] Hence due to these clear differences, the knowledge obtained during the last several decades on the deposition, growth and the

optical properties of inorganic thin films cannot be directly applied to the ones of organic materials.

In general, there are two types of organic substances, *amorphous* materials and *crystalline* ones. For several applications including electronic devices such as transistors, the highest possible electron mobilities are required. This property is only found in the films with ultimate structural order and crystalline properties. For other applications such as light emitting devices, the highest possible quantum yield is most important. This yield depends upon the probability of radiative electron-hole recombination which is highest for amorphous materials where the electron and hole mobilities are low. Therefore, the opto-electronic performance of these materials are strongly dependent on the structural properties of the organic films employed. Hence to design organic thin film based devices a detailed understanding of the mechanisms governing film structure and growth as well as the knowledge of the optical properties is a necessity.

The present work aims at promoting our understanding of structural and optical properties of organic thin films. This should provide a deeper insight into the parameters that determine the molecular interactions, vibronic-electronic transitions and growth modes of organic materials. Therefore, it should help to improve the characteristics and performance of crystalline materials for OTFTs and amorphous materials for OLED applications.

Oligomers based on the family of five-membered thiophene conjugated ring and its derivatives have been considered as one of the most common conducting organic oligomers used in OTFT devices. According to the self-assembling nature of these oligomers, they should produce highly ordered organic thin films with remarkable crystallinity. Such well ordered structures are highly demanded for better electron mobilities in organic transistors. In this work we have studied the structure and the adsorption of 3-nitrothiophene/selenophen/tellurophen on Cu(110) surface utilising *ab initio* calculations. A fundamental new insight into the very detailed geometries and ordering of the molecules on surface and specificity of the interactions that occur between anchored molecules can be obtained by performing *ab initio* calculations. The basis of *ab initio* calculations is the density functional theory (DFT), which have been explained shortly in chapter 2. For the purpose of these calculations EStCoMPP program have been used. Chapter 3 contains the flow diagram of the EStCoMPP-code and the implementation of all theoretical ideas. In chapter 4 we are discussing about our obtained results for the structural and binding properties of the 3-nitrothiophene/selenophen/tellurophen on Cu(110) surface.

As it has been mentioned above, the next and interesting type of organic materials are *amorphous* ones which are being widely used in OLED applications. Chapters 5-9 of this thesis are focused on this type of materials and among them we are studying two specific molecules Tris-(8-hydroxyquinoline) aluminum (Alq_3) and N,N'-diphenyl-N,N'-bis(1-naphthyl)-1-1'-biphenyl-4,4'' diamine (α -NPD). These molecules are among the most commonly used electron-transport and hole-transport amorphous organic materials used for OLED applications. In this work we have investigated the optical and structural

properties of Alq_3 and α - NPD thin films. As it has been briefly mentioned, the optical properties of organic materials are different from the inorganic ones. The theoretical background of optical properties of organic materials is provided in Chapter 5. And chapter 7 contains the obtained results for optical properties of Alq_3 and α - NPD thin films.

For a better understanding and design of organic thin films based devices, in this case OLEDs, it is necessary to characterize and understand the morphology and growth modes of the consisting thin films. Chapter 8 provides the basic knowledge of the thin film growth with the emphasis on the amorphous growth models. Also, it provides the detailed quantitative methods for characterizing the morphology and height fluctuations of thin film surfaces. In this work, in order to determine a quantitative model for growth and morphology of α - NPD thin films, a systematic study on the influence of deposition rate and substrate temperature on film morphology have been done. Our results are demonstrated in Chapter 9.

2 First-principles methods

The electronic structure of atoms, molecules and solids can be described as a many-particle-system of interacting electrons and nuclei. The description of such systems has been an important goal of physics during this century. Analytic solutions of the Schrödinger equation are possible for a few very simple systems, and numerically exact solutions can be found for a small number of atoms and molecules. However, most cases of interest, such as reaction at surfaces or electron-electron interactions in solids, require the use of model Hamiltonians or simplified computational schemes. The development of schemes that provide useful information on real systems continues, and it is the purpose of this chapter to describe one of the them, the density functional theory (DFT). [9]

DFT calculations are widely used in determining the electronic and structural properties of molecular solids and interfaces. In this chapter the basis of the density functional theory (DFT) and *ab initio* methods will be explained.

In the most general form, the total hamiltonian for the system of electrons and nuclei can be written as summation of the kinetic energies of nuclei and electrons, the Coulomb energies due to ion-ion repulsion, ion-electron attraction, and electron-electron repulsion. Due to the large mass difference of electrons and nuclei the two systems can be separated in many cases. If we set the mass of the nuclei to infinity, then the kinetic energy of the nuclei can be ignored. [10] In this Born-Oppenheimer or "adiabatic" approximation the dynamics of electrons has to be treated in a frozen-in configuration of the nuclei. This leads to electronic energies and wave-functions which contain the nuclear coordinates as external parameters. The nuclear motion is then treated separately. It contains the ground-state energy of the electrons $E_0(R_i)$ for each nuclear configuration R_i as part of the potential energy. Finding the eigenfunctions and eigenvalues of the electronic system is still impossible without drastic simplifying assumption. Hartree [11] introduced the "independent electron approximation" in which the many-electron wave function is reduced to a product of single-particle function:

$$\Psi(\mathbf{r}_1, \mathbf{r}_2, \dots) = \Psi_1(\mathbf{r}_1) \cdots \Psi_1(\mathbf{r}_2) \quad (2.1)$$

Each of the functions $\Psi_i(\mathbf{r}_i)$ satisfies a one-electron Schrödinger equation with a potential term arising from the average field of the other electrons:

$$\left[-\frac{\hbar^2}{2m}\nabla^2 + V_{ext} + \Phi_i\right]\Psi_i(\mathbf{r}) = \epsilon_i\Psi_i(\mathbf{r}), \quad (2.2)$$

where V_{ext} is a potential due to the fixed nuclei or other external fields and Φ_i the Coulomb potential due to the electrons which is given by Poisson's equation

$$\nabla^2 \Phi_i = 4\pi e^2 \sum_{j=1, i \neq j}^N |\Psi_j|^2. \quad (2.3)$$

The Hartree approximation was extended by Fock and Slater in 1930 by replacing the product wave function by a single determinant function:

$$\Psi(\mathbf{r}_1, \mathbf{r}_2, \dots) = \frac{1}{\sqrt{N!}} \begin{vmatrix} \psi_1(\mathbf{r}_1) & \cdots & \psi_N(\mathbf{r}_1) \\ \vdots & & \vdots \\ \psi_1(\mathbf{r}_2) & \cdots & \psi_N(\mathbf{r}_2) \end{vmatrix} \quad (2.4)$$

Thus, the wave function of a many-electron system is antisymmetric under exchange of any two electrons as demanded by the Pauli principle. The spatial separation of two electrons with the same spin reduces the Coulomb energy of the system. The energy difference between the Hartree-Fock and Hartree approximation is the "exchange" energy. The Coulomb energy can be reduced below its Hartree-Fock value at the cost of increasing kinetic energy if electrons with opposite spins are also spatially separated. This is introduced by additional correlations between the electrons. The energy difference between the true many-electron energy and the Hartree-Fock approximation is the "correlation energy". In contrast to Hartree-Fock, DFT provides in principle an exact solution of the many-body problem in the electronic ground state as will be shown in the following.

2.1 Density functional theory

2.1.1 Hohenberg-Kohn theorem

In DFT, all ground state properties such as the total energy are expressed as a function of the density distribution. Hohenberg and Kohn have established two remarkable theorems for interacting electrons in an external potential $V(\mathbf{r})$ whose Hamiltonian is

$$H = \sum_{i=1}^N [-\partial_{\mathbf{r}_i}^2 + V(\mathbf{r})] + \sum_{i,j, i \neq j}^N \frac{1}{|\mathbf{r}_i - \mathbf{r}_j|}. \quad (2.5)$$

- 1: The ground-state of an inhomogeneous interacting many-electron system is a unique functional of the ground-state electron density $n_0(\mathbf{r})$.

- 2: There exists an energy-functional $E[n]$ which is minimized by the ground-state density $n_0(\mathbf{r})$ under the condition of charge conservation.

While Hohenberg and Kohn proved their theorems indirectly with the assumption that $n(\mathbf{r})$ is uniquely determined by the external potential (V-representation of $n(\mathbf{r})$), Levy [12] showed more precisely that the energy-functional is minimized by $n_0(\mathbf{r})$, using a variational method. He defined the energy-functional as:

$$E[n] := \min_{\Psi} \langle \Psi | H | \Psi \rangle \quad (2.6)$$

The expectation value of the Hamiltonian operator has to be minimized with respect to the norm conserving, antisymmetric many-particle wave-function Ψ , which reproduces a given electron-density $n(\mathbf{r})$ (Ψ representation of $n(\mathbf{r})$). The ground-state density $n_0(\mathbf{r})$ and the ground-state energy $E[n_0]$ is determined by minimizing the energy-functional:

$$\delta E[n] = 0 \quad (2.7)$$

The subsidiary condition of the particle conservation

$$\int d^3(\mathbf{r}) n(\mathbf{r}) = N, \quad (2.8)$$

is taken into account using the Lagrangian-parameter μ . This leads to the minimization of a modified energy-functional

$$\delta \left\{ E[n] - \mu \left(\int d^3\mathbf{r} n(\mathbf{r}) - N \right) \right\} = 0, \quad (2.9)$$

which yields the following Euler-Lagrange equation:

$$\left. \frac{\delta E[n(\mathbf{r})]}{\delta n(\mathbf{r})} \right|_{n_0(\mathbf{r})} = \mu. \quad (2.10)$$

An explicit form of the energy-functional could not be derived from the approach of Hohenberg and Kohn, nor from Levy's formulation. Thus, additional approximations need to be considered.

2.1.2 The Kohn-Sham formalism

The main idea of the Kohn-Sham formulation is to map the system of N interacting electrons onto an auxiliary system of N non-interacting electrons with the same density as the interacting system. In this case the charge density can be expressed in terms of single particle orbitals Ψ_i

$$n(\mathbf{r}) = \sum_{i=1}^N |\Psi_i(\mathbf{r})|^2. \quad (2.11)$$

With the kinetic energy of the non-interacting particle is given by¹

$$E_{kin}^0[n(\mathbf{r})] = -\frac{1}{2} \sum_{i=1}^N \int d\mathbf{r} \Psi_i^*(\mathbf{r}_i) \nabla^2 \Psi(\mathbf{r}_i) \quad (2.12)$$

The contributions to the total energy of the ground state are formally split-up into four parts

$$E[n(\mathbf{r})] = E_{kin}^0[n] + E_{ext}[n] + E_H[n] + E_{xc}[n], \quad (2.13)$$

where E_{kin}^0 is the functional of the kinetic energy of N *non-interacting* electrons. E_{ext} describes the energy of electrons with the density $n(\mathbf{r})$ in an external potential $V_{ext}(\mathbf{r})$, e.g. the interaction with the nuclei. E_H gives the Coulomb energy in the Hartree approximation, and all unknown many-particle effects, including the corrections to the kinetic energy, are contained in the exchange-correlation functional E_{xc} which is defined by Eq. 2.13. To find an explicit form of the functional $E[n]$ only $E_{xc}[n]$ has to be approximated. The successful and widely used approximations for E_{xc} will be presented in Section 2.1.3. This, however, is only a small contribution to the total electron energy [9].

Within this scheme, the system of interacting particles in an external potential V_{ext} is now replaced by a system of non-interacting particles in an effective potential V_{tot} . The single particle wave functions in Eq. 2.11 are orthogonal to each other and fulfill the norm

$$\langle \Psi_i(\mathbf{r}) | \Psi_i(\mathbf{r}) \rangle = 1. \quad (2.14)$$

If the variational principle for the total energy E is applied with respect to the function Ψ_i , the norm is enforced by the constraint instead of the particle conservation. With the introduction of N independent Lagrangian parameters ϵ_i one can then minimize the functional

$$\tilde{E} = E[n(\mathbf{r})] - \sum_i^N \epsilon_i \left[\int d\mathbf{r} \Psi_i^*(\mathbf{r}_i) \Psi(\mathbf{r}_i) - 1 \right]$$

using

$$\frac{\delta E}{\delta \Psi_i} = \frac{\delta E}{\delta n} \cdot \frac{\delta n}{\delta \Psi_i}. \quad (2.15)$$

¹In the following atomic units will be used, i.e.: $\hbar = 1$, $e = 1$, $m_e = 1$

This yields a simple equation of motion for each of the functions $\Psi_i(\mathbf{r})$ which has the appearance of a single particle Schrödinger equation where the Lagrangian parameter ϵ_i takes the role of the eigenvalue:

$$(-\partial_{\mathbf{r}}^2 + V_{tot}(\mathbf{r}))\Psi_i(\mathbf{r}) = \epsilon_i\Psi_i(\mathbf{r}) \quad (2.16)$$

The potential $V_{tot}(\mathbf{r})$ is an effective single particle potential

$$V_{tot}(\mathbf{r}) = V_{ext}(\mathbf{r}) + V_H(\mathbf{r}) + V_{xc}(\mathbf{r}), \quad (2.17)$$

which contains the contributions:

$$V_{ext}(\mathbf{r}) = \frac{\delta E_{ext}}{\delta n(\mathbf{r})} = V(\mathbf{r}), \quad (2.18)$$

$$V_H(\mathbf{r}) = \frac{\delta E_H}{\delta n(\mathbf{r})} = \int d\mathbf{r}' \frac{n(\mathbf{r}')}{|\mathbf{r} - \mathbf{r}'|}, \quad (2.19)$$

$$V_{xc}(\mathbf{r}) = \frac{\delta E_{xc}}{\delta n(\mathbf{r})}. \quad (2.20)$$

$V_{tot}(\mathbf{r})$ is density dependent and thus a functional of the function $\Psi(\mathbf{r}_i)$. A solution of the Kohn-Sham equations

$$[-\partial_{\mathbf{r}}^2 + V_{ext}(\mathbf{r}) + V_H(\mathbf{r}) + V_{xc}(\mathbf{r})]\Psi_i(\mathbf{r}) = \epsilon_i\Psi_i(\mathbf{r}) \quad (2.21)$$

has to be found by iterating to self-consistency. This Kohn-Sham approach represents a mapping of the interacting many-electron system onto a system of non-interacting electrons moving in an effective potential due to all the other electrons. The self-consistent solution of the Kohn-Sham equation gives the set of wave-functions Ψ_i that minimizes the Kohn-Sham energy-functional. If the exchange-correlation energy functional were known exactly, the functional derivative of the Kohn-Sham equations are formally one-particle energies. However, since they are only Lagrangian parameters in density functional theory, they have strictly speaking no physical meaning. The same argument holds for one-particle wave-functions, which have no physical meaning as well. Nevertheless, following Koopmans-theorem, an interpretation of the ϵ_i and $\Psi_i(\mathbf{r})$ as eigenvalues and one-particle wave-functions is generally possible [9]. For delocalized states, where the correlation effects are relatively small, the spectroscopically measured ionization energies and the energies calculated with the density functional theory are indeed in good agreement. This is not true for strongly localized states (e.g. atomic states). However, the surface-states which are calculated in this thesis are sufficiently delocalized and can be interpreted as physical states.

2.1.3 Exchange-correlation approximations: LDA and GGA

Approximations enter density functional theory due to the fact that the exchange-correlation energy is unknown for inhomogeneous systems. The simplest method of describing the exchange-correlation energy is to use the local-density approximation (LDA), which assumes that the exchange-correlation energy per electron at a point \mathbf{r} in the electron gas $\epsilon_{xc}(\mathbf{r})$, is equal to the exchange-correlation energy per electron in a homogeneous gas that has the same density as the electron gas at point \mathbf{r} . Thus, the exchange-correlation energy density

$$\epsilon_{xc}^{LDA}[n(\mathbf{r})] = \epsilon_{xc}^{hom}(n(\mathbf{r})) \quad (2.22)$$

now is a function and not any more a functional of the density $n(\mathbf{r})$ and spatial integration yields the exchange-correlation energy:

$$E_{xc}^{LDA}[n(\mathbf{r})] = \int d^3\mathbf{r} \epsilon_{xc}^{LDA}(\mathbf{r}) n(\mathbf{r}) \quad (2.23)$$

The V_{xc} -potential is then calculated

$$\begin{aligned} V_{xc}^{LDA}[n(\mathbf{r})] &= \frac{\delta E_{xc}^{LDA}[n(\mathbf{r})]}{\delta n(\mathbf{r})} \\ &= \epsilon_{xc}^{LDA}(n(\mathbf{r})) + n(\mathbf{r}) \left(\frac{d\epsilon_{xc}^{LDA}(n)}{dn} \right)_{n=n(\mathbf{r})}. \end{aligned} \quad (2.24)$$

The Hartree-Fock equation can be solved exactly for a homogeneous electron gas yielding for the exchange energy $\epsilon_x(n)$ the result

$$\epsilon_x(n) = -\frac{3}{2} \left(\frac{3}{\pi} \right) n^{1/3}. \quad (2.25)$$

The ground-state energy as a function of the electron density can be calculated numerically and under the assumption that any correlation beyond exchange is written as:

$$\epsilon_{xc}(n) = \epsilon_x(n) + \epsilon_c(n). \quad (2.26)$$

Now commonly used parameterizations of the LDA are based on the quantum Monte Carlo results by Ceperley and Adler [13] and have been proposed by Perdew and Zunger [14], or Teter et al. [15]. Calculations using these functionals yield good result for the ground state properties for a wide range of materials, Gunnarson et al. [16], [17] pointed out, that this is due to the fact, that only the spherical average of the exchange-correlation hole (the

hole near the origin of the pair distribution function) determines the exchange-correlation potential and that this spherical average is reproduced well by the LDA [17].

An extension of the LDA is the General Gradient Approximation (GGA) which describes the exchange-correlation energy not only as a function of the local density but also of its variation

$$E_{xc}^{(GGA)}[n(\mathbf{r})] = \int d\mathbf{r} n(\mathbf{r}) \epsilon_{xc}^{hom}(n(\mathbf{r})) F_{xc}[n(\mathbf{r}), \nabla n(\mathbf{r})]. \quad (2.27)$$

The enhancement factor $F_{xc}[n(\mathbf{r}), \nabla n(\mathbf{r})]$ has two separate parts due to the exchange and correlation contributions. In common parameterizations ϵ_{xc} is an analytical function designed to satisfy certain conditions e.g. that the exchange hole is negative everywhere and represents a deficit of one electron [105]. Among those GGA's one finds those of Perdew and Wang [18] or Perdew, Burke and Ernzerhof, PBE [19]. The generalized gradient approximation implemented in the code is PBE-GGA in which all parameters other than those due to the correlation contributions are fundamental constants.

2.1.4 Spin-density functional theory

So far we have described the non-polarized form of the density functional theory. To study the magnetic properties like the ferro- or antiferromagnetism of solids and molecules or surface magnetism, spin polarization of the electron density needs to be considered. The expansion of the density-functional for spin-polarized electrons is straightforward. The generalization is achieved by considering the collinear magnetic states. In this case, the Hamiltonian can be written as two diagonal blocks for each spin direction and the electron density $n(\mathbf{r})$ can be replaced by the spin-densities $n^\uparrow(\mathbf{r})$ and $n^\downarrow(\mathbf{r})$ for electrons with spin-up and spin-down, respectively. The electron-density and the magnetisation-density are then defined as

$$\begin{aligned} n(\mathbf{r}) &= n^\uparrow(\mathbf{r}) + n^\downarrow(\mathbf{r}), \\ m(\mathbf{r}) &= n^\uparrow(\mathbf{r}) - n^\downarrow(\mathbf{r}). \end{aligned} \quad (2.28)$$

The energy-functional in the Hohenberg-Kohn theorems is generalized to a functional of two densities

$$E[n] \rightarrow E[n^\uparrow(\mathbf{r}), n^\downarrow(\mathbf{r})]. \quad (2.29)$$

It is minimized by the ground-state densities $n_0^\uparrow(\mathbf{r})$ and $n_0^\downarrow(\mathbf{r})$. The Kohn-Sham equations are obtained by the variation of the energy-functional with respect to the spin-densities. The approximation used most widely is the local spin-density approximation (LSDA), where

$$\epsilon_{xc}^{LSDA}[n^\uparrow(\mathbf{r}), n^\downarrow(\mathbf{r})] = \epsilon_{xc}^{hom}(n^\uparrow, n^\downarrow) \quad (2.30)$$

is the exchange and correlation energy per particle of a homogeneous, spin-polarized electron gas [20].

2.2 Density functional theory in a plane wave implementation

2.2.1 Periodic supercells

With the application of the Kohn-Sham formalism a many-body problem of N interacting particles can be reduced to the calculation of N single-electron equations. We have to define an appropriate basis set to expand the wave-functions, and express the different parts of the Hamiltonian. The systems we want to describe are usually non-periodic, but in order to use well-established band structure methods developed for ideal crystals, one approximates the inhomogeneous system by a periodic continuation of a supercell containing the structural inhomogeneity. For a crystal lattice the elementary cell is defined as the smallest structure, whose periodic continuation describes the crystal. The elementary cell is defined by three basis-vectors \mathbf{a}_1 , \mathbf{a}_2 , \mathbf{a}_3 . Each lattice-vector

$$\mathbf{R}^n = n_1 \mathbf{a}_1 + n_2 \mathbf{a}_2 + n_3 \mathbf{a}_3, \quad \mathbf{n} = (n_1, n_2, n_3), \quad n_i \in \mathbb{Z}, \quad (2.31)$$

points to the position of a different elementary cell and any property of the lattice $f(\mathbf{r})$ ($f(\mathbf{r})$ e.g. potential $V(\mathbf{r})$, electric density $n(\mathbf{r})$) has to be periodic in \mathbf{R}^n :

$$f(\mathbf{r} + \mathbf{R}^n) = f(\mathbf{r}) \quad (2.32)$$

The volume of the elementary cell is

$$\Omega = \mathbf{a}_1 \cdot (\mathbf{a}_2 \times \mathbf{a}_3). \quad (2.33)$$

The basis-vectors of the reciprocal space are defined by

$$\mathbf{b}_i = 2\pi \frac{\mathbf{a}_j \times \mathbf{a}_k}{\Omega}, \quad (2.34)$$

for cyclic i, j, k . The reciprocal space is then spanned by the reciprocal lattice-vectors

$$\mathbf{G}^m = g_1 \mathbf{b}_1 + g_2 \mathbf{b}_2 + g_3 \mathbf{b}_3, \quad (2.35)$$

which ensures that for each \mathbf{G}^m and \mathbf{R}^n

$$e^{i\mathbf{G}^m \cdot \mathbf{R}^n} = 1. \quad (2.36)$$

To describe inhomogeneous systems like molecules or surfaces of solids, a supercell has to be defined which contains the molecule and enough of its neighborhood to be able to describe the required electronic and atomic configuration meaningfully.

2.2.2 Bloch's Theorem

Using the supercell approach, the potential $V(\mathbf{r})$ also has the periodicity of the supercell:

$$V(\mathbf{r}+\mathbf{R}) = V(\mathbf{r}) \quad (2.37)$$

Bloch's theorem states that in a periodic potential each wave-function can be expressed as the product of a cell-periodic part $u_{\nu,\mathbf{k}}(\mathbf{r})$ and a plane-wave part $e^{i\mathbf{k}\mathbf{r}}$

$$\Psi_{\nu,\mathbf{k}}(\mathbf{r}) = e^{i\mathbf{k}\mathbf{r}} u_{\nu,\mathbf{k}}(\mathbf{r}). \quad (2.38)$$

The cell periodic part of the wave function can be expanded using a basis set consisting of a discrete set of plane waves whose wave vectors are reciprocal lattice vectors

$$u_{\nu,\mathbf{k}}(\mathbf{r}) = \sum_{\mathbf{G}} c_{\nu,\mathbf{G}} e^{i\mathbf{G}\cdot\mathbf{r}}. \quad (2.39)$$

Therefore, each electronic wave-function can be written as a sum of plane waves

$$\Psi_{\nu,\mathbf{k}} = \sum_{\mathbf{G}} c_{\nu,\mathbf{k}+\mathbf{G}} e^{i(\mathbf{k}+\mathbf{G})\cdot\mathbf{r}}. \quad (2.40)$$

The wave-vector \mathbf{k} can always be confined to the first Brillouin zone (1.BZ), because any \mathbf{k}' outside the 1.BZ can be written as

$$\mathbf{k}' = \mathbf{k} + \mathbf{G}, \quad (2.41)$$

where \mathbf{G}^m is a reciprocal lattice vector and \mathbf{k} lies in the first Brillouin zone. Since there are many solutions for a given \mathbf{k} the band index ν has to be used to fully characterize the wave-functions.

2.2.3 k-point sampling

By imposing appropriate boundary conditions (e.g. Born-von Karman [or periodic] boundary conditions) on the wave functions, it can be shown that the wave vector \mathbf{k} must be real, and electronic states are only allowed at a discrete set of \mathbf{k} -points. The electronic wave-functions $\Psi_{\nu\mathbf{k}}$ are continuous functions of \mathbf{k} . Thus, it is possible to represent the wave-function over a region of \mathbf{k} -space approximately by the wave-function at a single \mathbf{k} -point. In this case the electronic states at only a finite number of \mathbf{k} -points are required to calculate the electronic potential. The distribution of these \mathbf{k} -points in the

first Brillouin-zone, which yield accurate results for calculation of the electronic potential, have been studied by a number of groups ([21], [22], [23]). In the EStCoMPP-program the Monkhorst-Pack method is used to generate the special \mathbf{k} -point set. Using these \mathbf{k} -point sets, the BZ integration can be done, yielding an accurate approximation for the electronic potential and the total energy, by calculating the electronic states at only a small number of \mathbf{k} -points. Thus, the convergence of the total energy has to be checked by a series of calculations with increasing \mathbf{k} -point density. With a set of special \mathbf{k} -point the integration over the first Brillouin-zone is replaced by a weighted summation over the \mathbf{k} -points:

$$\int_{1.BZ} d^3\mathbf{k} \cdots \rightarrow \sum_{\mathbf{k}} \omega_{\mathbf{k}} \cdots \quad (2.42)$$

where $\omega_{\mathbf{k}}$ is the weight of the \mathbf{k} -point, which are also given by the Monkhorst-Pack method.

2.2.4 Plane-wave basis sets

In the plane wave expansion the KS wave functions are represented in terms of discrete plane-wave basis sets, as it has been stated by Bloch's theorem, Eq.2.40. In principle, an infinite basis set is required to expand the electronic wave-functions. However, since we want to describe rather smooth valence wave-functions the importance of the coefficients $c_{\nu, \mathbf{k}+\mathbf{G}}$ decreases with increasing $|\mathbf{k}+\mathbf{G}|$. Thus, the plane-wave basis set can be truncated to include only plane waves that have kinetic energies less than some particular cutoff-energy $E_{cut} = |\mathbf{k}+\mathbf{G}_{cut}|^2$. The error for the calculation of the total energy with a particular plane-wave basis can be reduced by increasing the cutoff-energy. As for the \mathbf{k} -points, the appropriate cut-off has to be checked by a series of calculations with increasing cutoff-energy.

2.3 The pseudopotentials

Pseudopotentials were originally introduced to simplify electronic structure calculations by eliminating the need to include atomic core states and the strong potentials responsible for binding them. [24] Under the assumption that the charge-densities of the core-electrons do not overlap with neighboring atoms, it is possible to treat them as frozen-in. They shield the strong ionic potential, and it should be possible to replace the true potential by a weaker pseudopotential for the valence electrons. Outside the core region, i.e. beyond a cutoff radius r_c , the true all-electron potential and the pseudopotential are identical, see Fig. 2.1. The weaker pseudopotential should ideally remove the rapid oscillation of the valence wave-functions in the core region. For density functional calculations one has to construct norm-conserving pseudopotentials, which guarantee charge conservation. Two

contradictory criteria determine the usefulness of a pseudopotential: (i) the pseudopotential should be "soft", i.e. only a small number of plane-wave basis states should be necessary to describe the wave-functions, and (ii) the pseudopotentials should be transferable, which means that the potential should give the correct ground-state energy of the valence electrons in different chemical environments. Condition (i) can easily be met by using a large cutoff radius while condition (ii) requires a small cutoff radius. In the actual construction a compromise has to be found in each case.

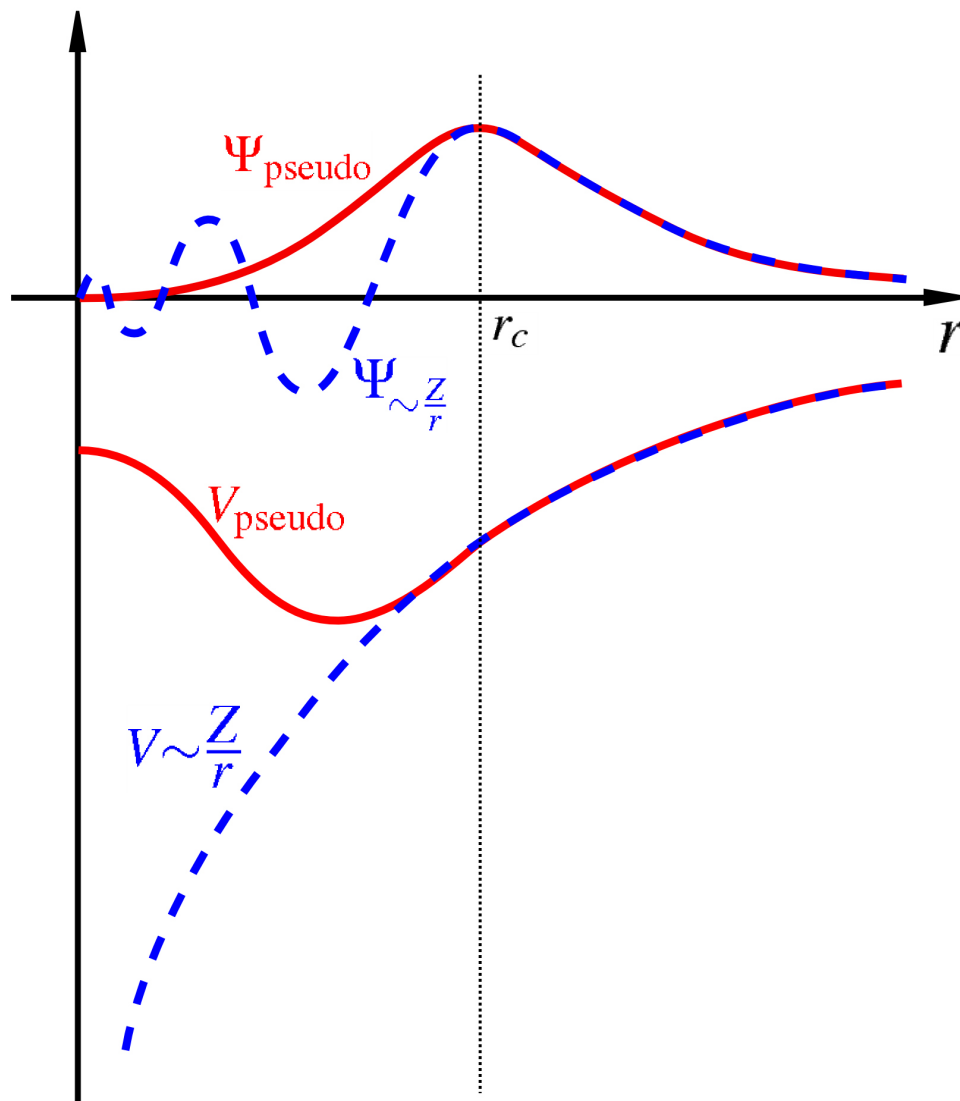


Figure 2.1: Schematic illustration of an all-electron (dashed lines) and pseudoelectron (solid lines) valence wave-function and potentials. Beyond the cutoff radius r_c , the scattering from the two potentials is indistinguishable.

2.3.1 Norm-conserving pseudopotentials

Generating a norm-conserving pseudopotential proceeds as follows [24]. All-electron calculations for an isolated atom in its ground-state and some excited states are performed. Then one chooses a cutoff radius $r_{c,l}$ and constructs a pseudo (ps) wave-function $\Psi_{ps,l}$ and pseudopotential $V_{ps,l}(\mathbf{r})$ with adjustable parameters, which deviate from the true all-electron functions only inside of the cutoff radius. The pseudo wave-functions and pseudopotentials are constructed in such a way, that the following conditions are fulfilled [25]

- (1) The pseudo-eigenvalues have to be equal to the all-electron valence-eigenvalues.
- (2) The pseudo wave-functions $\Psi_{ps,l}(\mathbf{r})$ has to be node-less and continuously differentiable.
- (3) Charge conservation is guaranteed if $\Psi_{ps,l}(\mathbf{r})$ fulfills the norm-conserving condition

$$\int_0^r d\mathbf{r} |\Psi_{ps,l}(\mathbf{r})|^2 = \int_0^r d\mathbf{r} |\Psi_l(\mathbf{r})|^2 \quad \forall r \geq r_{cut}. \quad (2.43)$$

Since outside r_c the wave-functions are identical by construction, norm conservation is then guaranteed in the entire space.

- (4) The logarithmic derivatives of the true all-electron and pseudo wave function and their first energy derivatives agree for $r \geq r_{cut}$

$$\frac{\partial(\ln \Psi_{ps,l}(\mathbf{r}, r))}{\partial r} = \frac{\partial(\ln \Psi_l(\mathbf{r}, r))}{\partial r} \quad \forall |\mathbf{r}| \geq r_{cut}. \quad (2.44)$$

This condition ensures that the scattering properties are accurately described.

2.3.2 Semi-local pseudopotentials and Kleinman-Bylander factorization

In its the most general form, the semi-local pseudopotential is given by

$$V^{PS}(\mathbf{r}) = \sum_l V_l^{PS}(r) \hat{P}_l, \quad (2.45)$$

where \hat{P}_l is a projection-operator for the angular momentum component l . Since all potentials show the same long-range Coulomb-behavior, a common local potential can be separated:

$$\begin{aligned}
V^{PS}(\mathbf{r}) &= \sum_l V_l(r) \hat{P}_l + \sum_l (V_l^{SL}(r) - V_{loc}(r)) \hat{P}_l \\
&= V_{loc}(r) + \sum_l \Delta V_l^{SL}(r) \hat{P}_l
\end{aligned} \tag{2.46}$$

The semi-local, l -dependent potentials $\Delta V_l^{SL}(r)$ are limited to the core-region. Using a plane-wave basis, a matrix element of such a semi-local pseudopotential would have the form

$$\begin{aligned}
\Delta V_l^{SL}(\mathbf{k} + \mathbf{G}, \mathbf{k} + \mathbf{G}') &:= \frac{1}{\Omega} \langle e^{i(\mathbf{k} + \mathbf{G})\mathbf{r}} | \Delta V_l^{SL}(r) \hat{P}_l | e^{i(\mathbf{k} + \mathbf{G}')\mathbf{r}} \rangle \\
&= \frac{4\pi}{\Omega} (2l + 1) P_l(\cos \gamma_{\mathbf{k} + \mathbf{G}, \mathbf{k} + \mathbf{G}'}) \\
&\times \int dr j_l(|\mathbf{k} + \mathbf{G}|r) \Delta V_l^{SL}(r) j_l(|\mathbf{k} + \mathbf{G}'|r) r^2,
\end{aligned} \tag{2.47}$$

where j_l is a spherical Bessel-function, P_l a Legendre-polynomial, Ω the volume of the cell and $\gamma_{\mathbf{k} + \mathbf{G}, \mathbf{k} + \mathbf{G}'}$ the angle between $(\mathbf{k} + \mathbf{G})$ and $(\mathbf{k} + \mathbf{G}')$. Hence, the pseudopotential contribution to the Hamiltonian is a matrix with the dimension $N \times N$, where N is the number of plane waves. The computational effort for diagonalization of such a matrix scales with N^3 . Such calculations are very time consuming, for large systems.

The choice of V_{loc} is arbitrary and if it is made equal to one of the V_l this avoids the need for the corresponding set of angular momentum projectors. Kleinman and Bylander proved that each semi-local pseudopotential can be transformed into a fully non-local pseudopotential. With $\Delta V_l^{SL}(r) = V_l^{SL}(r) - V_{loc}(r)$ and the pseudo-wave function, $\Psi_{lm}(\mathbf{r})$, the Kleinman-Bylander form is

$$\Delta V_l(r) \hat{P}_l \cong \Delta V_l^{KB} = \sum_{m=-l}^{+l} \frac{|\Delta V_l(r) \Psi_{lm}\rangle \langle \Psi_{lm} \Delta V_l(r)|}{\langle \Psi_{lm} | \Delta V_l(r) | \Psi_{lm} \rangle}, \tag{2.48}$$

where Ψ_{lm} are the pseudo wave-functions which were used for the construction of the semi-local pseudopotential $\Delta V_l(r)$. The application of the Kleinman-Bylander pseudopotential to the pseudo wave-function yields the same results as the application of the semi-local pseudopotential by construction. Using the lm -representation of Ψ_{lm} in the form $\Psi_{lm} = \frac{g_l(\mathbf{r})}{r} Y_{lm}(\theta, \varphi)$, the plane-wave matrix element of $\Delta V_l(r)$ is given by

$$\begin{aligned}
\Delta V_l^{KB}(\mathbf{k} + \mathbf{G}, \mathbf{k} + \mathbf{G}') &:= \frac{1}{\Omega} \langle e^{i(\mathbf{k}+\mathbf{G})\mathbf{r}} | \Delta V_l^{KB}(r) \hat{P}_l | e^{i(\mathbf{k}+\mathbf{G}')\mathbf{r}} \rangle \\
&= \frac{4\pi}{\Omega} (2l+1) P_l(\cos \gamma_{\mathbf{k}+\mathbf{G}, \mathbf{k}+\mathbf{G}'}) \\
&\times \frac{T_l^*(|\mathbf{k} + \mathbf{G}|) T_l(|\mathbf{k} + \mathbf{G}'|)}{W_l},
\end{aligned} \tag{2.49}$$

Using this form of the pseudopotential, it is found that if the pseudo wave function is expanded in plane waves the double sum over \mathbf{G} and \mathbf{G}' becomes separable, and the computation of the non-local part of the potential scales like $N \cdot \log(N)$ if iterative diagonalization schemes are used.

2.3.3 The PAW pseudopotentials

The basic idea of the projector augmented wave method (PAW) has been developed in Blöchl [26] and W. Kromen [27] works. The PAW method combines the concept of the pseudopotential (PS) and linear augmented plane wave method (LAPW) in a way that all-electron valence wave functions are reconstructible.

To sketch the basic ideas of the definition of the PAW method for an atom, one can define a smooth part of valence wave function $\tilde{\Psi}_i^v(\mathbf{r})$ and a linear transformation $\Psi^v = T\tilde{\Psi}^v$. This transformation relates the set of all-electron valence functions $\Psi_j^v(\mathbf{r})$ to the smooth pseudo wave functions $\tilde{\Psi}_i^v(\mathbf{r})$, not necessary norm-conserving. The transformation is assumed to be unity except with a sphere centered on the nucleus, $T = \mathbf{1} + T_0$. For simplicity, we omit the superscript v , assuming that the Ψ s are valence states, and the labels, i, j . Adopting the Dirac notation, the expansion of each smooth function $|\tilde{\Psi}\rangle$ in partial waves m within each sphere can be written,

$$|\tilde{\Psi}\rangle = \sum_m c_m |\tilde{\Psi}_m\rangle, \tag{2.50}$$

with the corresponding all-electron function,

$$|\Psi\rangle = T |\tilde{\Psi}\rangle = \sum_m c_m |\Psi_m\rangle. \tag{2.51}$$

Hence, the full wave function in all space can be written

$$|\Psi\rangle = |\tilde{\Psi}\rangle + \sum_m c_m \{|\Psi_m\rangle - |\tilde{\Psi}_m\rangle\}, \tag{2.52}$$

If the transformation T is required to be linear, then the coefficients must be given by a projection

$$c_m = \langle \tilde{p}_m | \tilde{\Psi} \rangle, \tag{2.53}$$

for some set of projection operators \tilde{p} . [10] If the projection operators satisfy the biorthogonality condition,

$$\langle \tilde{p}_m | \tilde{\Psi}'_m \rangle = \delta_{m,m'}, \quad (2.54)$$

then the one-center expansion $\sum_m |\tilde{\Psi}_m\rangle \langle \tilde{p}_m| \tilde{\Psi}\rangle$ of the smooth function $\tilde{\Psi}$ equals $\tilde{\Psi}$ itself. Finally, the transformation can be written as

$$T = \mathbf{1} + \sum_m \{ |\Psi_m\rangle - |\tilde{\Psi}_m\rangle \} \langle \tilde{p}_m|. \quad (2.55)$$

The general form of the PAW equations can be cast in terms of transformation (Eq. 2.55). For any operator \hat{A} in the original all-electron problem, one can introduce a transformed operator $\hat{\tilde{A}}$ that operates on the smooth part of the wave functions

$$\hat{\tilde{A}} = T^\dagger \hat{A} T = \hat{A} + \sum_{m,m'} |\tilde{p}_m\rangle \{ \langle \Psi_m | \hat{A} | \Psi'_m \rangle - \langle \tilde{\Psi}_m | \hat{A} | \tilde{\Psi}'_m \rangle \} \langle \tilde{p}'_m|. \quad (2.56)$$

The expressions for physical quantities in the PAW approach follow from Eq. 2.55) and Eq. 2.56). For example, the density is given by

$$n(\mathbf{r}) = \tilde{n}(\mathbf{r}) + n^1(\mathbf{r}) - \tilde{n}^1(\mathbf{r}) \quad (2.57)$$

where $\tilde{n}(\mathbf{r})$ represents the charge over the entire space due to the extended pseudo wave functions (it is the charge due to the plane wave expansion of the smooth pseudo wave functions throughout the space), $\tilde{n}^1(\mathbf{r})$ is the charge due to the smooth pseudo wave functions inside of the augmentation sphere, and $n^1(\mathbf{r})$ represents the 'true' charge within the augmentation sphere (it is the charge due to the all electron wave functions inside of augmentation sphere).

3 The EStCoMPP-program

The Electronic Structure Code for Materials Properties and Processes , EStCoMPP, was created by S. Blügel and K. Schroeder and developed by B. Engels, P. Richard, R. Berger, W. Kromen, A. Antons and N. Atodiresei in the framework of their PhD-Theses ([28], [29], [30], [27], [31], [32]). The following chapter is a brief introduction into the methods and algorithms used in the EStCoMPP program for calculating total energy and forces.

3.1 Minimization of the energy functional

In order to calculate the physical properties of a system for a given atomic configuration, the electronic states that minimize the Kohn-Sham energy have to be determined. To achieve this, an iterative scheme is used, where starting from a trial electron-density, the eigenvalue equations are solved (also by iterative methods), and a new electron-density is generated successively until self-consistency is reached. The energy-functional consist of the electronic energy (Eq. 2.13) and the Ewald-energy $E_{Ew}[n]$, due to the Coulomb interaction of the ions. There are several contributions due to the Coulomb interaction, i.e. Hartree energy, local pseudopotential energy and ion-ion interaction, which diverge separately. But one can combine the contributions to non-divergent expressions by adding and subtracting appropriate compensating charges. When the energy scale is fixed in such a way that the average electronic potential of the system is set to zero, a constant contribution to the total energy, called $E_{loc}[n]$, has to be taken into account:

$$E_{tot}[n(\mathbf{r})] = E_{kin}[n] + E_{ext}[n] + E_H[n] + E_{xc}[n] + E_{Ew}[n] + E_{loc}[n] \quad (3.1)$$

Depending on the functional form of the operators in the Hamiltonian, the matrix-vector products $H|\Psi\rangle$ are either solved in real-space or in \mathbf{k} -space. All contributions to the total energy are finally summed up in \mathbf{k} -space. To avoid questionable convergence of the self consistency iterations due to oscillations of states close to the Fermi-level (i.e. states that are occupied in one iteration step but empty in the next) oscillations are damped by using a Fermi-distribution at a finite temperature T . The occupation numbers of the states with eigenenergies $\epsilon_{\nu,\mathbf{k}}$ are defined as:

$$f_{\nu,\mathbf{k}} = \frac{1}{\exp(\epsilon_{\nu,\mathbf{k}} - \epsilon_F)/k_B T + 1}. \quad (3.2)$$

This yields a smooth variation of the occupation numbers around the Fermi-energy, but simultaneously introduces a temperature dependence of the total energy, which can define the total energy of the electron system

$$F = E - TS, \quad (3.3)$$

where the entropy-term for independent electrons can be expressed by

$$S = -2k_B \sum_{\nu, \mathbf{k}} \omega_{\mathbf{k}} (f_{\nu, \mathbf{k}} \ln f_{\nu, \mathbf{k}} + (1 - f_{\nu, \mathbf{k}}) \ln (1 - f_{\nu, \mathbf{k}})), \quad (3.4)$$

with the factor 2 from spin-degeneracy. The free energy converges faster than the total energy at a given temperature T . For low temperature T the total energy E and the free energy F can be expressed by the ground state energy E_0

$$\begin{aligned} F &= E_0 - \gamma T^2, \\ E &= E_0 + \gamma T^2, \end{aligned} \quad (3.5)$$

Hence, the ground-state energy at $T = 0$ can be approximated by

$$E_0 = \frac{1}{2}(E + F). \quad (3.6)$$

The iteration cycle should start at a sufficiently high temperature, so that the density and the free energy F converge smoothly. Afterwards, the temperature can be decreased to assure that the extrapolation to the ground-state energy is accurate. The iterative method to reach ground-state electron-density (and ground state-energy) is demonstrated in the flowchart of Fig. 3.1.

3.2 Explicit form of the equations

The explicit form of the equations, used in the EStCoMPP code, are shortly presented in the following subsections. The detailed description of the pseudopotential generation code and the program used for solid state calculations can be found in the PhD-theses of B. Engels, P. Richard, R. Berger and W. Kromen ([28], [29], [30], [27]).

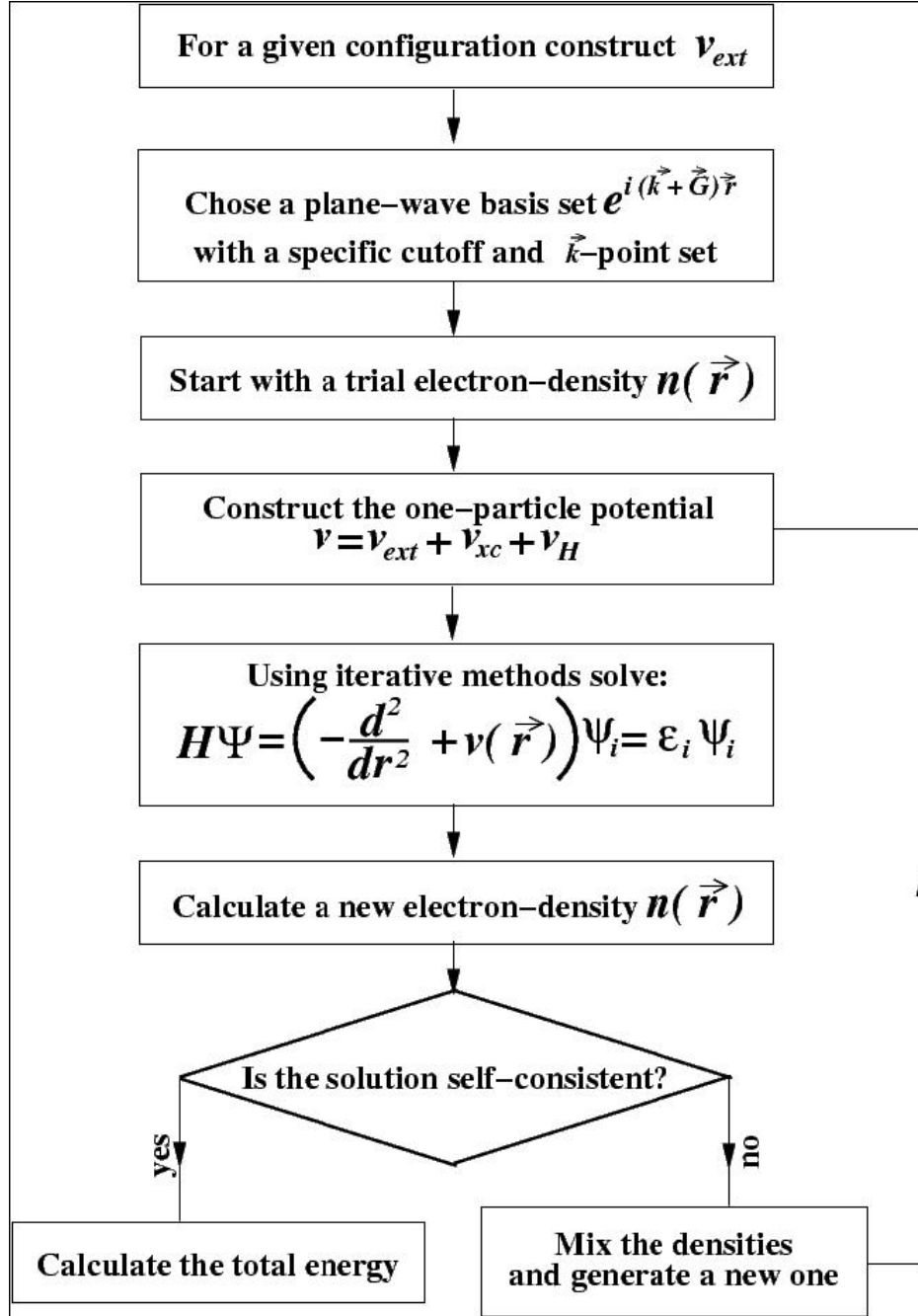


Figure 3.1: Flowchart of the iterative procedure for the calculation of the electronic energy.

3.2.1 The kinetic energy

The Kinetic-energy functional is diagonal in \mathbf{k} -space, and thus can be evaluated by

$$\begin{aligned} E_{kin}[n(\mathbf{r})] &= \langle \Psi | -\partial_r^2 | \Psi \rangle_{\Omega} = \sum_{\nu, \mathbf{k}} \omega_{\mathbf{k}} f_{\nu, \mathbf{k}} \langle \Psi_{\nu, \mathbf{k}} | -\partial_r^2 | \Psi_{\nu, \mathbf{k}} \rangle_{\Omega} \\ &= \sum_{\nu, \mathbf{k}} \sum_{\mathbf{G}} \omega_{\mathbf{k}} f_{\nu, \mathbf{k}} |\mathbf{k} + \mathbf{G}|^2 u_{\nu, \mathbf{k}}^*(\mathbf{G}) u_{\nu, \mathbf{k}}(\mathbf{G}). \end{aligned} \quad (3.7)$$

The matrix-vector products reveals

$$\langle \mathbf{r} | E_{kin} | \Psi_{\nu, \mathbf{k}} \rangle_{\Omega} = \frac{1}{\sqrt{\Omega}} \sum_{\mathbf{G}} |\mathbf{k} + \mathbf{G}|^2 u_{\nu, \mathbf{k}}(\mathbf{G}) e^{-i(\mathbf{k} + \mathbf{G}) \cdot \mathbf{r}} \quad (3.8)$$

with the following matrix-elements:

$$\langle \mathbf{k} + \mathbf{G} | E_{kin} | \Psi_{\nu, \mathbf{k}} \rangle_{\Omega} = |\mathbf{k} + \mathbf{G}|^2 u_{\nu, \mathbf{k}}, \quad (3.9)$$

$$\langle \mathbf{k}' + \mathbf{G}' | E_{kin} | \mathbf{k} + \mathbf{G} \rangle_{\Omega} = |\mathbf{k} + \mathbf{G}|^2 \delta_{\mathbf{k}, \mathbf{k}'} \delta_{\mathbf{G}, \mathbf{G}'}. \quad (3.10)$$

3.2.2 The local energy

The local energy consists of the exchange-correlation part, the local part of the pseudopotential and the Hartree contribution. The local potentials are applied to the wave-function in real-space to avoid the calculation of convolution-equations. The transformation from reciprocal-space to real-space is obtained via fast-fourier transformations (FFT's). The Hartree-potential is determined by Poissons' equation :

$$\Delta V_H(\mathbf{r}) = -8\pi n(\mathbf{r}) \quad (3.11)$$

The Fourier transformation yields

$$\begin{aligned} V_H(\mathbf{G}) &= \frac{1}{\Omega} \int_{\Omega} d^3\mathbf{r} V_H(\mathbf{r}) e^{i\mathbf{G} \cdot \mathbf{r}} \\ &= \frac{1}{\Omega} \frac{8\pi}{G^2} n(\mathbf{G}). \end{aligned} \quad (3.12)$$

Thus the Hartree-potential is calculated in reciprocal space. The matrix-vector products are given by

$$\langle \mathbf{r} | V_H | \Psi_{\nu, \mathbf{k}} \rangle_{\Omega} = \frac{1}{\sqrt{\Omega}} \sum_{\mathbf{G}} \left(\sum_{\mathbf{G}'} V_H(\mathbf{G}') u_{\nu, \mathbf{k}}(\mathbf{G} - \mathbf{G}') \right) e^{-i(\mathbf{k} + \mathbf{G}) \cdot \mathbf{r}}, \quad (3.13)$$

with the matrix-elements

$$\langle \mathbf{k}' + \mathbf{G}' | V_H | \mathbf{k} + \mathbf{G} \rangle_{\Omega} = \sum_{\mathbf{G}'} V_H(\mathbf{G}'). \quad (3.14)$$

The exchange-correlation energy in the local density approximation is defined as

$$E_{xc}^{LDA}[n(\mathbf{r})] = \int d^3\mathbf{r} \epsilon_{xc}^{LDA} n(\mathbf{r}). \quad (3.15)$$

The matrix-vector products are calculated in real-space as

$$\langle \mathbf{r} | V_{xc} | \Psi_{\nu, \mathbf{k}} \rangle_{\Omega} = V_{xc}(n(\mathbf{r})) \Psi_{\nu, \mathbf{k}}(\mathbf{r}). \quad (3.16)$$

The local part of the pseudopotential consists of the spherical-symmetric contributions of the atoms at the position $\mathbf{R} + \tau_{\mu}$. Thus the local pseudopotential is given by

$$V_{loc}(\mathbf{r}) = \sum_{\mu} V_{loc}^{\alpha(\mu)}(\mathbf{r} + \tau_{\mu}). \quad (3.17)$$

Here we have used the fact that all chemically identical atoms (of kind α) are described by the same pseudopotential $V_{loc}^{\alpha(\mu)}$. With the Fourier transformation

$$V_{loc}(\mathbf{r}) = \sum_{\mu, \mathbf{G}} S_{\tau_{\mu}}(\mathbf{G}) V_{loc}^{\alpha(\mu)}(\mathbf{G}) e^{-i\mathbf{G} \cdot \mathbf{r}}, \quad (3.18)$$

this transforms to

$$V_{loc}(\mathbf{G}) = \sum_{\mu} S_{\tau_{\mu}}(\mathbf{G}) V_{loc}^{\alpha(\mu)}(\mathbf{G}), \quad (3.19)$$

where

$$V_{loc}^{\alpha(\mu)}(\mathbf{G}) = \frac{1}{\Omega} \int_{\Omega} d\mathbf{r} V_{loc}^{\alpha(\mu)}(\mathbf{r} + \tau_{\mu}) e^{-i\mathbf{G} \cdot \mathbf{r}}, \quad (3.20)$$

and the structure-factors are

$$S_{\tau_\mu}(\mathbf{G}) = e^{-i\mathbf{G}\cdot\tau_\mu}. \quad (3.21)$$

The expressions for the matrix-vector products are

$$\langle \mathbf{r} | V_{loc} | \Psi_{\nu,\mathbf{k}} \rangle_\Omega = \sum_{\mathbf{G},\mathbf{G}'} \sum_{\mu} \frac{1}{\Omega} S_{\tau_\mu}(\mathbf{G}') V_{loc}^{\alpha(\mu)}(\mathbf{G}) \times u_{\nu,\mathbf{k}}(\mathbf{G} - \mathbf{G}') e^{-i(\mathbf{k}+\mathbf{G})\cdot\mathbf{r}}, \quad (3.22)$$

$$\langle \mathbf{k} + \mathbf{G} | V_{loc} | \Psi_{\nu,\mathbf{k}} \rangle_\Omega = \sum_{\mathbf{G}'} V_{loc}(\mathbf{G}') u_{\nu,\mathbf{k}}(\mathbf{G} - \mathbf{G}'). \quad (3.23)$$

The electron-ion Coulomb interaction leads to a long-range term $\approx -2Z/r$ for each of the local pseudopotentials. To allow the numerical integration of $\nu_{loc}^{\alpha(\mu)}$ in \mathbf{k} -space, the long-range part has to be separated and solved analytically.

3.2.3 The non-local part of the energy

The non-local contribution of the pseudopotential consists of the l -dependent part of the total energy. This energy is evaluated by different expressions for the norm- and non-norm-conserving (PAW) pseudopotentials. For the case of Kleinman-Bylander pseudopotentials (see section 2.3.2) the non-local parts are expressed as follows:

$$\begin{aligned} V_{KB} &= \sum_{\mathbf{R}} \sum_{\mu} \sum_{l=0}^{l_{max}} \sum_{m=-l}^{+l} E_{KB}^{l,\alpha(\mu)} T_{\mathbf{R},\tau_\mu} |t_{l,m,\alpha(\mu)}\rangle \langle t_{l,m,\alpha(\mu)}| \\ &= \sum_{\mu} \sum_{l=0}^{l_{max}} \sum_{m=-l}^{+l} E_{KB}^{l,\alpha(\mu)} T_{\tau_\mu} |t_{l,m,\alpha(\mu)}\rangle \langle t_{l,m,\alpha(\mu)}| \end{aligned} \quad (3.24)$$

where T_{τ_μ} is the translation-operator, which shifts the non-local part of the pseudopotential to the position τ_μ of the ions. For the matrix vector products the following expressions are derived

$$\begin{aligned} \langle \mathbf{r} | V_{KB} | \Psi_{\nu,\mathbf{k}} \rangle_\Omega &= \sum_{\mu} \sum_{l=0}^{l_{max}} \sum_{m=-l}^{+l} \left(\sum_{\mathbf{G}'} T_{l,m,\mu}^*(\mathbf{k},\mathbf{G}') u_{\nu,\mathbf{k}}(\mathbf{G}') \right) E_{KB}^{l,\alpha(\mu)} \\ &\quad \times \frac{1}{\Omega} \sum_{\mathbf{G}} T_{l,m,\mu}(\mathbf{k},\mathbf{G}) e^{-i(\mathbf{k}+\mathbf{G})\cdot\mathbf{r}}, \end{aligned} \quad (3.25)$$

$$\begin{aligned} \langle \mathbf{k} + \mathbf{G} | V_{KB} | \Psi_{\nu, \mathbf{k}} \rangle_{\Omega} &= \sum_{\mu} \sum_{l=0}^{l_{max}} \sum_{m=-l}^{+l} T_{l,m,\mu}(\mathbf{k}, \mathbf{G}) E_{KB}^{l,\alpha(\mu)} \\ &\times \left(\sum_{\mathbf{G}'} T_{l,m,\mu}^*(\mathbf{k}, \mathbf{G}') u_{\nu, \mathbf{k}}(\mathbf{G}') \right), \end{aligned} \quad (3.26)$$

where

$$T_{l,m,\mu}(\mathbf{k}, \mathbf{G}) = S_{\tau_{\mu}}(\mathbf{G}) \Upsilon_{lm}(\theta_{\mathbf{k}+\mathbf{G}}, \varphi_{\mathbf{k}+\mathbf{G}}) t_{l,\alpha(\mu)}(|\mathbf{k} + \mathbf{G}|), \quad (3.27)$$

and

$$t_{l,\alpha(\mu)}(|\mathbf{k}, \mathbf{G}|) = \frac{4\pi}{\sqrt{\Omega}} \int_{\infty}^0 dr r t_{l,\alpha(\mu)}(r) j_l(|\mathbf{k} + \mathbf{G}| r). \quad (3.28)$$

Due to the dyadic structure of the KB pseudopotentials, the evaluation of the expectation values in reciprocal space is favorable.

The non-local part of the non-norm-conserving pseudopotentials (PAW) is expressed in \mathbf{k} -space as [27]:

$$\langle \mathbf{k} + \mathbf{G} | \nu_{NL} | \mathbf{k} + \mathbf{G}' \rangle = \sum_{\mu; \gamma, \gamma'} \langle \mathbf{k} + \mathbf{G} | \tilde{\mathbf{P}}_{\gamma}^{\mu} \rangle \mathbf{D}_{\gamma, \gamma'} \langle \tilde{\mathbf{P}}_{\gamma}^{\mu} | \mathbf{k} + \mathbf{G}' \rangle \quad (3.29)$$

$$\langle \mathbf{k} + \mathbf{G} | \nu_{NL} | \tilde{\Psi}_{\mathbf{k}, \nu} \rangle = \sum_{\mu; \gamma} \langle \mathbf{k} + \mathbf{G} | \tilde{\mathbf{P}}_{\gamma}^{\mu} \rangle \sum_{\gamma} \mathbf{D}_{\gamma, \gamma'} \langle \tilde{\mathbf{P}}_{\gamma}^{\mu} | \tilde{\Psi}_{\mathbf{k}, \nu} \rangle \quad (3.30)$$

for which the $\langle \mathbf{k} + \mathbf{G} | \tilde{\mathbf{P}}_{\gamma}^{\mu} \rangle$ and $\langle \tilde{\mathbf{P}}_{\gamma}^{\mu} | \mathbf{k} + \mathbf{G}' \rangle$ are evaluated in reciprocal space:

$$\langle \mathbf{k} + \mathbf{G} | \tilde{\mathbf{P}}_{\gamma}^{\mu} \rangle = i^l e^{i \cdot \mathbf{k} \cdot \tau_{\mu}} S^{\mu}(\mathbf{G}) \tilde{\mathbf{P}}_{l,i}^{\alpha(\mu)}(|\mathbf{k} + \mathbf{G}|) \sqrt{4\pi} \cdot Y(\mathbf{k} + \mathbf{G}) \quad (3.31)$$

$$\langle \Psi_{\mathbf{k}, \nu} | \tilde{\mathbf{P}}_{\gamma}^{\mu} \rangle = \sum_{\mathbf{G}} \langle \Psi_{\mathbf{k}, \nu} | \mathbf{k} + \mathbf{G} \rangle \langle \mathbf{k} + \mathbf{G} | \tilde{\mathbf{P}}_{\gamma}^{\mu} \rangle \quad (3.32)$$

where

$$\tilde{\mathbf{P}}_{\gamma}^{\mu}(\mathbf{r}) = \frac{1}{\mathbf{r}} Y_L(\hat{\mathbf{r}}) \tilde{\mathbf{P}}_{l,i}^{\alpha(\mu)}(\mathbf{r}) \quad (3.33)$$

$$\tilde{\mathbf{P}}_{l,i}^{\alpha(\mu)}(\mathbf{k} + \mathbf{G}) = \sqrt{\frac{4\pi}{\Omega}} \int_0^{\mathbf{R}_{\mu}} \mathbf{r} \cdot j_l(|\mathbf{k} + \mathbf{G}|) \tilde{\mathbf{P}}_{l,i}^{\alpha(\mu)}(\mathbf{r}) d\mathbf{r} \quad (3.34)$$

$S^\mu(\mathbf{G})$ represents the structure factors, $\alpha(\mu)$ is the type of atom μ , $\tilde{\mathbf{P}}_\gamma^{\alpha(\mu)}$; $\gamma = (l, i)$ are the projector functions localized in the augmentation sphere of the type of atom μ ; Υ_L are the spherical harmonics, j_l the spherical Bessel-functions, L represent the (\mathbf{l}, \mathbf{m}) -channels and \mathbf{i} represent the index of the projectors belonging to the same atom and \mathbf{l} -channel, but generated at different energies.

3.2.4 The Ewald-energy

The Coulomb interaction of the ions μ at the positions $\mathbf{R}^n + \tau_\mu$ is described by the Ewald-energy E_{Ew} . This term can be expressed in real or reciprocal space

$$\begin{aligned} E_{Ew} &= \frac{1}{2} \sum_{\mathbf{R}^n} \sum_{\mu, \mu'} \frac{Z_\mu Z'_\mu}{|\tau_\mu - (\mathbf{R}^n + \tau'_\mu)|} (1 - \delta_{\tau_\mu, \mathbf{R}^n + \tau'_\mu}). \\ &= \frac{1}{2} \sum_{\mathbf{G} \neq 0} \sum_{\mu, \mu'} Z_\mu Z'_\mu \frac{1}{\Omega} \frac{4\pi}{\mathbf{G}^2} e^{-i\mathbf{G}(\tau_\mu - \tau'_\mu)}. \end{aligned} \quad (3.35)$$

A faster convergence of the sums is achieved by applying Ewald summation formula [33] yielding a splitting of the sums with contributions from real and reciprocal space which include damping factors. The separately divergent terms for the $(|\mathbf{G}| = 0)$ components of the Hartree-energy, the local pseudopotential and the Ewald-energy compensate each other. Since, we use an energy scale for the eigenvalue problem where the sum of the average Hartree and local pseudopotential is set to zero we have to consider a constant term [34], [29] to the total energy

$$E_{loc}^{const} = \frac{N^\nu}{\Omega} \sum_{\mu} \int_{\infty} d^3\mathbf{r} \left(V_{loc}^{\alpha(\mu)}(r) + \frac{2N_{\alpha(\mu)}(r)}{r} \right), \quad (3.36)$$

where

$$N^\nu = \int_{\Omega} d^3\mathbf{r} n(\mathbf{r}) = n(\mathbf{G})|_{\mathbf{G}=0}. \quad (3.37)$$

3.2.5 The Hellman-Feynman forces

In the Born-Oppenheimer approximation the total energy of the system is explicitly parametric dependent on the coordinates of the ions τ_μ . Thus, the forces on the ions can be calculated by the derivative of the energy-functional $E_{tot}[n(\mathbf{r}), \{\tau_\mu\}]$ with respect to the

coordinates of atoms τ_μ , where μ numbers the ions. In the Born-Oppenheimer approximation the energy-functional consists of the ground-state electronic-energy $E_{el}[n(\mathbf{r}), \{\tau_\mu\}]$ and the Coulomb-interaction of the ions:

$$E_{ion}[\tau_\mu] = \frac{1}{2} \sum_{\mu'} \frac{Z_\mu Z_{\mu'}}{|\tau_\mu - \tau_{\mu'}|} \quad (3.38)$$

Thus, the forces are given by

$$F = -\partial_{\tau_\mu} E_{el}[n(\mathbf{r}, \tau_\mu)] - \partial_{\tau_\mu} E_{ion}[\tau_\mu]. \quad (3.39)$$

While the forces on the ions due to the Coulomb-interaction can easily be calculated analytically

$$F_{ion}(\tau_\mu) = -\frac{1}{2} \partial_{\tau_\mu} \sum_{\mu'} \frac{Z_\mu Z_{\mu'}}{|\tau_\mu - \tau_{\mu'}|}, \quad (3.40)$$

the forces due to the electronic ground-state energy are given by

$$F_{el}(\tau_\mu) = -\partial_{\tau_\mu} \langle \Psi(\tau_\mu) | H | \Psi(\tau_\mu) \rangle, \quad (3.41)$$

where H is the Hamiltonian-operator of the electronic system. The evaluation of this expression is complicated, since, the wave functions depend implicitly on the atom coordinates. In Born-Oppenheimer approximation this equation is reduced to the Hellman-Feynman force

$$\begin{aligned} F_{HF} &= -\partial_{\tau_\mu} \langle \Psi(\tau_\mu) | H | \Psi(\tau_\mu) \rangle = -\langle \Psi(\tau_\mu) | -\partial_{\tau_\mu}(H) | \Psi(\tau_\mu) \rangle - E \partial_{\tau_\mu} \langle \Psi(\tau_\mu) | \Psi(\tau_\mu) \rangle \\ &= -\langle \Psi(\tau_\mu) | -\partial_{\tau_\mu}(H) | \Psi(\tau_\mu) \rangle \end{aligned} \quad (3.42)$$

Under the subsidiary condition of charge conservation this functional is minimal for the ground-state density $n(\mathbf{r})$. The functional derivative of the electronic energy-functional with respect to the density yields the chemical potential μ :

$$\mu = \frac{\partial E[n(\mathbf{r}), \tau_\mu]}{\partial n(\mathbf{r})} \quad (3.43)$$

Thus, the force resulting from the electronic contribution to the total force is given by:

$$\begin{aligned}
F_{el}(\tau_\mu) &= -\partial E_{el}[n(\mathbf{r}), \tau_\mu] - \int d^3\mathbf{r} \left(\frac{\partial E[n(\mathbf{r}), \tau_\mu]}{\partial n(\mathbf{r})} \right) \partial_{\tau_\mu} n(\mathbf{r}, \tau_\mu) \\
&= -\partial E_{el}[n(\mathbf{r}), \tau_\mu] - \mu \int d^3\mathbf{r} \partial_{\tau_\mu} n(\mathbf{r}, \tau_\mu) \\
&= -\partial E_{el}[n(\mathbf{r}), \tau_\mu] - \underbrace{\mu \partial_{\tau_\mu} N}_{=0}
\end{aligned} \tag{3.44}$$

As conclusion, the electronic contribution to the forces on the atoms are simply given by the partial derivative of the energy-functional with respect to the coordinates of the atoms.

3.3 The loop-structure and the algorithms

In the last sections, the theoretical aspects of density functional theory and the pseudopotential method were discussed. In order to determine the atomic and electronic structure of a system one needs to proceed with the following steps:

- Calculate the electronic structure
- Calculate the forces on the atoms
- relax the atoms towards the equilibrium positions.

In the EStCoMPP code, all these steps are done using iterative procedures in nested loops as shown in Fig 3.2

3.3.1 Iterative Eigenvalue Determination

The electronic states that minimize the Kohn-Sham energy have to be determined for a given ionic configuration. For a typical calculation of interest in this work, supercells with about 200 atoms are being treated for which a high-energy cutoff may be required (about 150 plane waves per atom). Due to this large dimension and the fact that only the lowest 2-10% of the eigenvalues ϵ_i and eigenvectors have to be determined, the preferred method is to iteratively improve upon initial functions.

Among different methods available to carry out the iterative eigenvalue determination, the Davidson-Kosugi algorithm ([35], [36]) is the method implemented in the EStCoMPP

code. This method is an extended version of the Davidson and then of the Block-Davidson algorithm with a fixed dimension of the sub-space to avoid memory problems. The original Davidson algorithm is developed for the calculation of a single eigenvalue and eigenvector. It begins with a starting vector, to which in each iteration, one correction vector is added. For calculating more eigenvectors, Block-Davidson algorithm has been used. A correction-vector for each eigenvector is calculated in each iteration and added to the sub-space. Thus the dimension of the sub-space is increase in each iteration. To avoid this memory problems, the Davidson-Kosugi algorithm, in which the dimension of the sub-space is fixed, is used. In each iterations, if all unit-vectors are filled, the oldest correction-vectors will be replaced instead until the eigenvalue problem is converged. The iterative procedure consists of the following steps:

- guess the starting vectors $|\Psi_i\rangle^{(0)}$
- solve the matrix products $|H\Psi_i\rangle^{(j)} = H |\Psi_i\rangle^{(j)}$
- construct the correction-vectors $|\Psi_i^{corr}\rangle^{(j)}$
- calculate the new starting vectors $|\Psi_i^{corr}\rangle^{(j+1)}$
- iterate until the norm of the correction-vectors is smaller than a given quality criterion

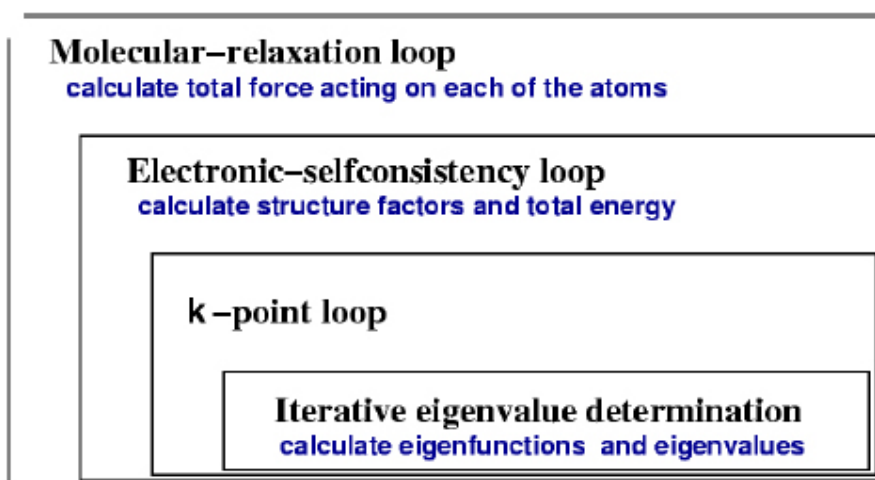


Figure 3.2: Loop-structure schemes in the EStCoMPP -program.

3.3.2 The electronic self-consistency and molecular relaxation loops

The degrees of freedom of the system can be separated into electronic and ionic degree of freedoms, within the Born-Oppenheimer approximation. Hence, the energy functional can be divided into two parts:

- electronic degrees of freedom, i.e. the density $n(\mathbf{r})$, resp. the effective potential $V_{eff}[n(\mathbf{r})]$.
- The ionic degrees of freedom, i.e. the positions of the ions τ_μ

The energy-functional is minimized with respect to the electronic degrees of freedom (and fixed ion-positions) by a self-consistent calculation. This results in the ground-state density, ground state potential and the ground state energy for fixed ion positions. Thus, starting with a density $n^i(\mathbf{r})$ resp. a potential $V[n^i(\mathbf{r})]$ the Kohn-Sham equations are formulated. In general, the new density and potential for the next iteration step can be written as

$$n^{i+1}(\mathbf{r}) = F\{n^i(\mathbf{r})\}$$

and

$$V[n^{i+1}(\mathbf{r})] = F'\{V[n^i(\mathbf{r})]\}. \quad (3.45)$$

Hence, at the fixed points of $F\{n(\mathbf{r})\}$ and $F'\{V[n(\mathbf{r})]\}$ the energy-functional will be minimized. Furthermore, for the molecular-relaxation, the energy-functional has to be minimized with respect to the atomic coordinates. Hence, a similar fix point scheme can be formulated for the ionic degrees of freedom using the atomic coordinates and Hellman-Feynman forces. In the EStCoMPP-program, both fixed point problems are solved with the iterative Quasi-Newton method [37].

4 3-nitrothiophene/selenophen/ tellurophen on Cu(110)

4.1 Introduction

Organic electronics, a technology that uses carbon-based semiconductors, is viewed as a promising complement to silicon-based electronics. [38] One particular device that is being developed using organic semiconductors is the organic thin film transistor (OTFT). These devices are currently receiving a great deal of attention, as their performance has reached levels comparable to that of transistors based on amorphous silicon. [39] The realization that the performance of these devices is intimately connected to the structure and morphology of the organic film has motivated numerous studies of organic thin film growth, which has revealed interesting physics. [40], [41], [41] For several applications including electronic devices such as transistors, the highest possible electron mobilities are required. This property is only found in the films with ultimate structural order and crystalline properties. In contrast to the strong atomic binding forces in inorganic crystals and thin films, organic molecules, as building blocks of organic solids, are bound to each other by the relatively weak van der Waals forces. Furthermore, for the case of the organic molecules based on aromatic hydrocarbons which generally possess extended anisotropic shapes, specific molecular orientation and order for the crystal and thin film nucleation are required. Therefore, the knowledge obtained during the last several decades on the deposition and growth of inorganic thin films can not be directly applied to the growth and nucleation of organic films. [42] Nevertheless, it has been realized that the molecule-substrate interaction plays a crucial role in determining the molecular orientation [43], growth mode [44], film morphology [43], and even the crystal structure [45]. However, the complete description of the mechanisms by which the molecule-substrate interaction affects the film properties still remain unclear.

Considerable work is now being undertaken in molecular self-assembly experiments leading to growth of oriented organic films. [46] Detailed investigations of bonding, interaction and orientation of these molecule-substrate interfaces are necessary. Such investigations can be performed both experimentally by utilizing techniques such as high resolution electron energy spectroscopy (HREELS), low energy electron diffraction (LEED), scanning tunneling microscopy (STM) and theoretically by *Ab initio* calculations. [47] With such information it should be possible to fabricate a specific molecular-surface structure whose chemistry and physics can be controlled and optimized to achieve a desired goal.

In this work we have studied the adsorption of 3-nitrothiophene/selenophen/tellurophen on Cu(110) surface, utilising *ab initio* calculations. Polythiophene and its derivatives have played an important role as a prototypical conducting polymer. The self-assembling nature of thiophene derivatives can produce highly ordered organic films with remarkable crystallinity. [32], [47] The experimental studies of the similar molecules (containing thiophene ring or benzen one) such as 3-thiophene carboxylate [32], [47], benzoate [48], nitrobenzen [49] using HREELS shows that at high coverage the molecules are adsorbed on the surface perpendicularly. The (2×1) super structure that is formed is confirmed also by the LEED experiments. The overall behavior of 3-nitrothiophene/selenophen/tellurophen is similar to benzoate [48], nitrobenzen [49] and 3-thiophene carboxylic acid [47], [32], adsorbing on Cu(110) in an upright orientation near saturation coverage. The perpendicular orientation found here for these molecules allows for a higher surface coverage, which may lead to greater possibilities for crystallisation within organic films of related compounds. Thus such molecules can be considered as good candidates for self assembled organic thin films.

In this chapter, we will present the result of our investigation on the (2×1) structure of 3-nitrothiophene/selenophen/tellurophen on Cu(110) surface. For this purpose we have used the EStCoMPP computer program (Chapter 3). These calculations provide a basic understanding of intra- and inter-molecular interactions present in the observed structures. These results will be compared with the ones obtained for 3-thiophene/selenophen/tellurophen carboxylic acid [50] on the same substrate.

4.2 Free molecules in the gas phase

In order to investigate the adsorption process of 3-nitrothiophene/selenophen/tellurophen, we need first to optimize the structure of each single molecule in the gas phase.

As shown in Fig. 4.1, each molecule contains a π -conjugated ring (thiophene/selenophen/tellurophen) and a strong electron-withdrawing nitro ($-NO_2$) group. The π -conjugated ring in this molecule is formed by four sp^2 -hybridized carbon atoms and an atom of sulfur/selenium/tellurium. The ring structure can be assumed to derive from a benzene molecule by replacing two of CH groups with sulfur. In this five-membered ring the sulfur/selenium/tellurium atoms act as an electron donating heteroatom. Hence, they contribute two electrons to the aromatic ring, and consequently this π -conjugated ring (thiophene/selenophen/tellurophen) is considered as an electron-rich heterocycle. [32] Furthermore, the anchoring nitro($-NO_2$) group is a strong electron-withdrawing substituent. [49] Hence, these molecules don't have a centrosymmetric electron distribution and they possess a considerable dipole moment.

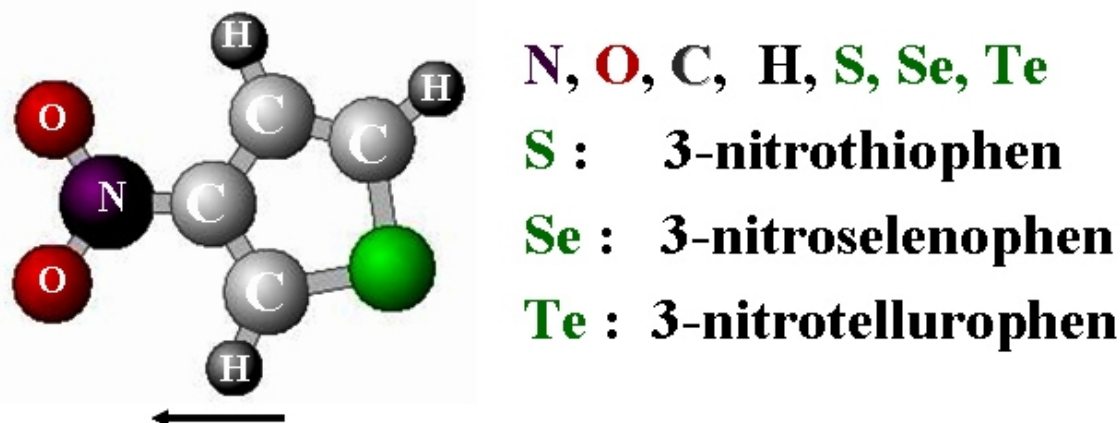


Figure 4.1: Schematic view of the 3-nitrothiophene/selenophen/tellurophen molecule. Each molecule contains a nitro ($-NO_2$) group and a π -conjugated ring consisting of four carbon atoms and an atom of sulfur/selenium/tellurium. S/Se/Te-green, C-gray, O-red, N-purple, H-dark gray. The array shows the dipole direction of the molecule.

4.2.1 Structure optimization

The atomic structure of the 3-nitrothiophene/selenophen/tellurophen (3NTh/Se/Te) free molecules, have been optimized using the PBE-GGA functional for the exchange-correlation function. The calculation has been performed in a box of $12 \times 11.5 \times 6.5 \text{ \AA}^3$ using a $3 \times 3 \times 3$ k-point set and a energy cutoff of 25 Ry. The corresponding pseudopotentials of the atoms were generated [32] using the same PBE-GGA scheme.

The structure of 3-thiophene carboxylate radical, optimized by N. Atodiresei [32] has been considered as the starting configuration in our calculations. To reach the optimized structure, the atoms of the 3-nitrothiophene/selenophen/tellurophen (3NTh/Se/Te) have been allowed to relax till the energy minimum is reached. These calculations show that, in the final relaxed configuration molecules have a planar geometry. This means that the π -conjugated ring and nitro group are in the same plane. Figure 4.2 shows the optimized structures of the three molecules of 3-nitrothiophene/selenophen/tellurophen. The result of the calculated bonds are presented in Table 4.1 and Table 4.2.

According to these results single molecules in the gas phase have a planar geometry and in the final relaxed configuration the conjugated ring and nitro group of the molecules are in the same plane. Moreover, it is possible to compare the bond length and bond angles for these three molecules according to Fig. 4.2, Table 4.1, Table 4.2. This comparison shows that C-S bond in the thiophene ring has the smallest length and going from sulfur to selenium and tellurium, the C-S/Se/Te bond length increases. Furthermore, the angle between these bonds in the thiophene ring (C-S-C) with the ones in the selenophen and the tellurophen rings (C-Se/Te-C) have been compared. This comparison shows that thiophene ring has the largest angle and respectively selenophen and tellurophen have smaller angles. This observation that has been demonstrated in Fig.

Bond (\AA)	thiophene	selenophen	tellurophen
$N_8 - O_6$	1.31	1.31	1.31
$N_8 - O_5$	1.31	1.31	1.31
$N_8 - C_1$	1.44	1.44	1.44
$C_1 - C_2$	1.39	1.38	1.38
$C_1 - C_3$	1.43	1.43	1.44
$C_3 - C_4$	1.38	1.38	1.37
$C_4 - S_7$	1.75	1.91	2.12
$C_2 - S_7$	1.72	1.87	2.09
$C_2 - H_9$	1.11	1.11	1.11
$C_3 - H_{10}$	1.11	1.11	1.12
$C_4 - H_{11}$	1.11	1.11	1.11

Table 4.1: The bond lengths in the conjugated ring and the nitro group for the optimized configurations of single molecules.

Angle (degree)	thiophene	selenophen	tellurophen
$O_6 - N_8 - O_5$	124	124	124
$C_2 - C_1 - C_3$	114	116	119
$C_3 - C_4 - S_7$	112	112	112
$C_2 - S_7 - C_4$	92	87	81
$C_1 - C_2 - S_7$	111	111	111
$C_1 - C_3 - C_4$	111	114	117

Table 4.2: The angles in the conjugated ring and the nitro group for the optimized configurations of single molecules.

4.2, can be explained by considering the fact that with increasing the atomic radius, from sulfur (1.03 \AA) to selenium (1.19 \AA) and tellurium (1.42 \AA) atoms, atomic electronegativity decreases. Therefore, their corresponding bond lengths increases though the angle between these bonds decreases.

4.3 Adsorption of the molecules on the surface

After structure optimization of the single molecules, we continue calculations for the structure and the nature of the bondings of the adsorbed molecules on the surface. The experimental results show that for monolayers of molecules such as 3-thiophene carboxylic acid [47], nitrobenzene [49] and benzoate [48] on Cu(110), at high coverage, molecules are well oriented with the aromatic ring perpendicular to the surface. However, to our knowledge there has not been a study, before ours for the case of 3-

nitrothiophene/selenophen/tellurophen (3NTh/Se/Te). Figure. 4.3 shows the high coverage adsorption process of 3NTh/Se/Te molecules on Cu(110) surface.

Ab initio calculations of 3-nitrothiophene/selenophen/tellurophen molecules on Cu(110)-substrate have been performed. In these calculations, the dense packed structure ((2×1) unit cell) has been considered. The exchange-correlation functional used in these calculation is PBE-GGA and the pseudopotentials are generated with the same PBE-GGA functional.

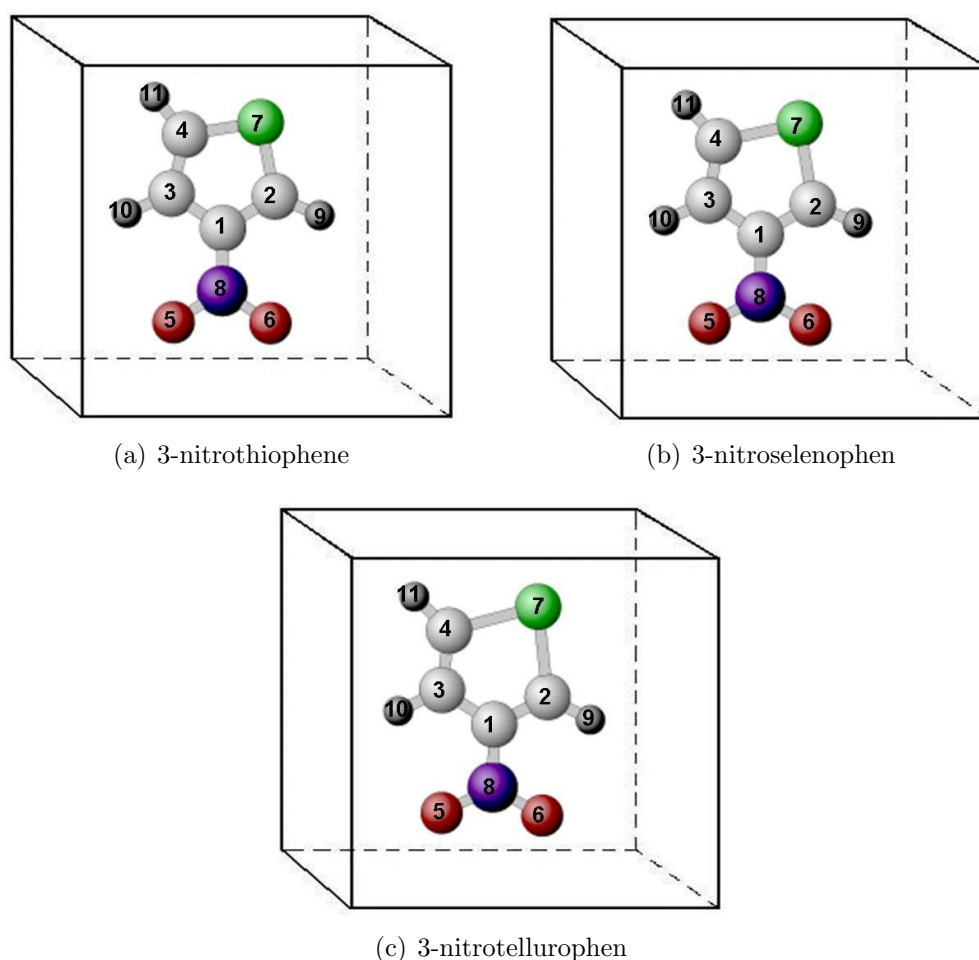


Figure 4.2: Schematic view of the optimized structures of single 3-nitrothiophene/selenophen/tellurophen molecules in the gas phase. S/Se/Te-green, C-gray, O-red, N-purple, H-dark gray.

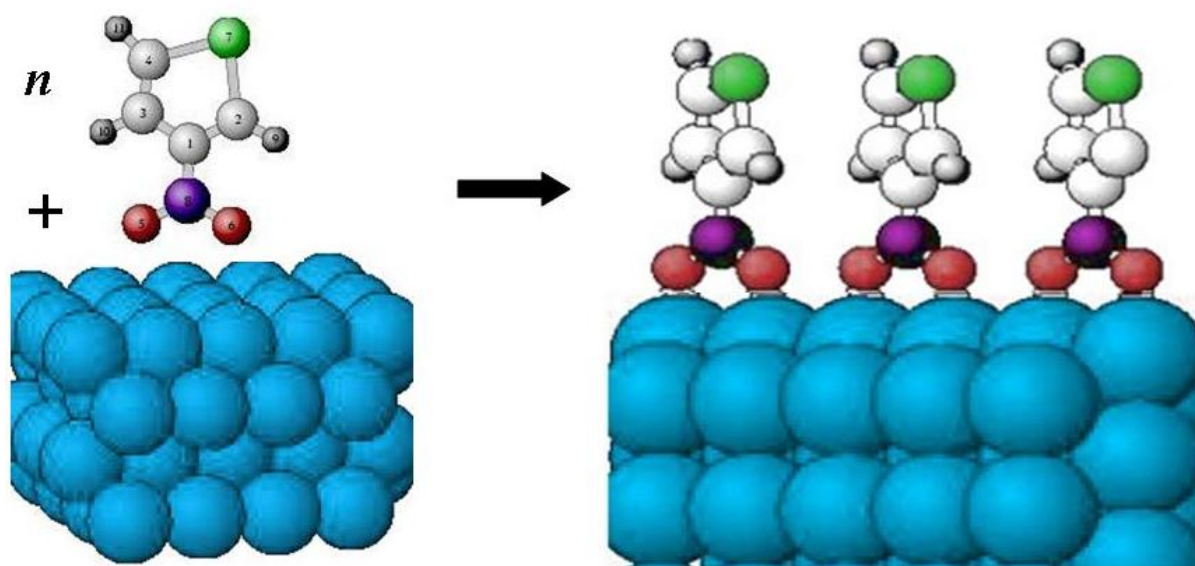


Figure 4.3: Schematic view of the high coverage adsorption of 3-nitrothiophene/selenophen/tellurophen on Cu(110) surface.

4.3.1 Rotation angle for conjugated rings: selenophen and tellurophen

The previous studies, [32], [47], have indicated that the thiophene conjugated ring is rotated with respect to the anchoring group (carboxylate). In this study, the rotational angle of the other two conjugated rings, selenophen and tellurophen, has been determined. This rotation is mainly due to the interaction of the rings with each other. Therefore, we expect the rotational behavior to be affected by changing the ring. However, changing the anchoring group dose not have a considerable influence on the ring rotation. The purpose of this angle determination is to find a good starting positions for a full structure optimization.

In order to determine the optimum rotational angle, a series of calculations has been performed for selenophen and tellurophen rings in carboxylate molecules. In these calculations, the copper atoms have been placed in the same plane as the carboxylate group and under its oxygen atoms. During calculations, the copper atoms are kept fixed at the nearest neighbors distance along the $[1\bar{1}0]$ direction of the Cu(110) surface, and only the molecule is allowed to relax. The calculations have been performed in the (2×1) cell which contains 2 layers of copper (4 atoms) and a molecule on each side (2×11 atoms) of the copper slab. Since in this part we are mainly focused on the interaction of the conjugated rings with neighboring ones and according to the test calculations, considering only 2 layers of Copper atoms should be sufficient. The inversion symmetry of the system has been included in the calculations. The dimension of the unit cell is $7 \cdot a \cdot \sqrt{2}$ (vertical), $a \cdot \sqrt{2}$, a (lateral). $a = 3.641 \text{ \AA}$ is the copper-fcc lattice constant fitted for bulk calculations

using $12 \times 12 \times 12$ k-point set. The calculations have been done using $1 \times 3 \times 4$ k-points and an energy cutoff of 25 Ry. With this arrangement a series of calculations have been done to estimate the optimum rotational angle of each ring. Without relaxing the atom distances each selenophen and tellurophen ring has been rotated from 0° up to 90° (in steps of 5°) relative to carboxylate group. The energy (with respect to the minimum) of each configuration is shown in Fig. 4.4. These results indicates that the minimum is located in the interval $20^\circ - 30^\circ$. Further series of calculations has been done for this interval, using smaller step of 1° . These calculations show (Fig. 4.4 and Table 4.3) that the minimum energy is corresponding to the rotation angle of 23° for thiophene, 25° for selenophen and 26° for the tellurophen ring, with respect to the $[1\bar{1}0]$ direction. Moreover, Fig. 4.4 indicates that the total energy of the rings consisting of larger atoms (selenium and tellurium) is more sensitive to the angle of rotation.

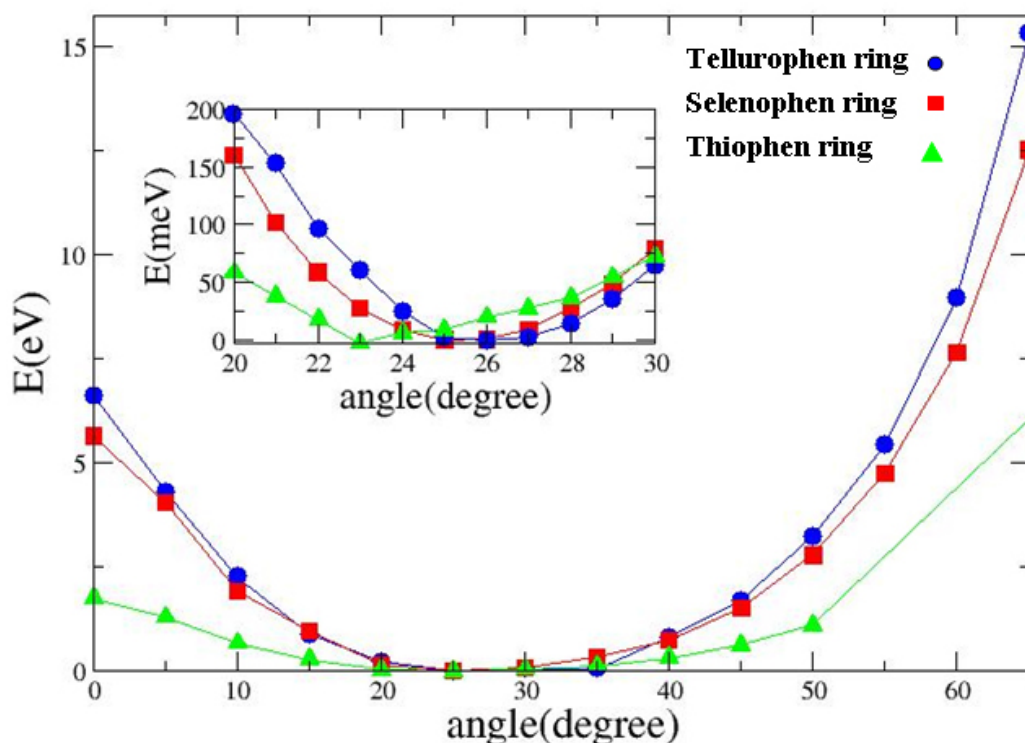


Figure 4.4: Energy (with respect to the minimum) vs. rotation angle. Thiophene ring-green, selenophen ring-red, tellurophen ring-blue.

4.3.2 Full relaxation of 3-nitrothiophene/selenophen/tellurophen on Cu(110) surface

In order to perform a full relaxation of the molecules on the substrate, the optimum configuration from the ring rotation calculations has been used as the starting posi-

tions. These calculations have been done for a dense packed (2×1) structure of 3-nitrothiophene/selenophen/tellurophen on Cu(110) substrate. The supercell contains 7 layers of Cu (14 atoms) and two molecules each on one side of the copper slab. The inversion symmetry of the system has been included in the calculations. The vacuum region above the molecules has a thickness of about 6.6 \AA (vertical distance between two adjacent molecules). In these calculations the size of the unit cell and the number of k-points are the same as in the rotation angle optimization.

3-nitrothiophene/selenophen/tellurophen are adsorbed on the surface in two most probable configurations, named as 'bridge' and 'top'. As shown in Fig. 4.7 these configurations refer to the position of the C-atom with respect to the Cu layer. In the 'bridge' position both oxygen atoms of each molecule are placed on top of the two nearest-neighbor copper atoms in a form that the nitro group make a bridge between the copper atoms. 'Top' position is the configuration in which the nitrogen atom of the nitro group is placed on top of the copper surface and the oxygen atoms are placed in the bridge position between two copper atoms of the nearest-neighbors. In these calculations, the structure optimization has been done by relaxing the first two copper layers and the adsorbed molecule. The optimization has been done until the minimum energy is reached. The ring rotation for the two configurations 'bridge' and 'top' is demonstrated in Fig. 4.5 and Fig. 4.6. In these figures, the oxygen atoms are bounded to the Cu atoms, the nitro group is in a plane parallel to the $[1\bar{1}0]$ direction, and the ring is rotated away from the $[1\bar{1}0]$.

The relaxed structures of the 3-nitrothiophene/selenophen/tellurophen adsorbed on Cu(110) substrate are shown in Fig. 4.7, Fig. 4.8 and Fig. 4.9. 'Bridge' configuration in comparison with 'top' position is energetically more favorable with almost 1 eV lower in total energy of the whole system. The relative stability of the different configurations can be explained in terms of the chemical bonding of the copper surface with the oxygen atoms of the nitro group. In Table 4.5 the "Cu-O" bond length for the optimized configuration of all these three molecules are given. "Cu-O" bond length in 'bridge' configuration is shorter comparing with the ones in 'top' position. Hence, the bridge configuration is more stable than the top one.

The bond lengths and the angles in the thiophene/selenophen/tellurophen rings and in the nitro group for the optimized structures of both the 'bridge' and the 'top' positions are given in Table 4.5 and Table 4.4. These results show that for each conjugated ring, the bond lengths and angles are just slightly changed from the 'bridge' position to the 'top' one. Moreover, the comparison of the different rings (thiophene/selenophen/tellurophen)

Ring name	Optimum rotation angle
thiophene	23°
selenophen	25°
tellurophen	26°

Table 4.3: Optimum rotation angle for the thiophene, selenophen and tellurophen rings.

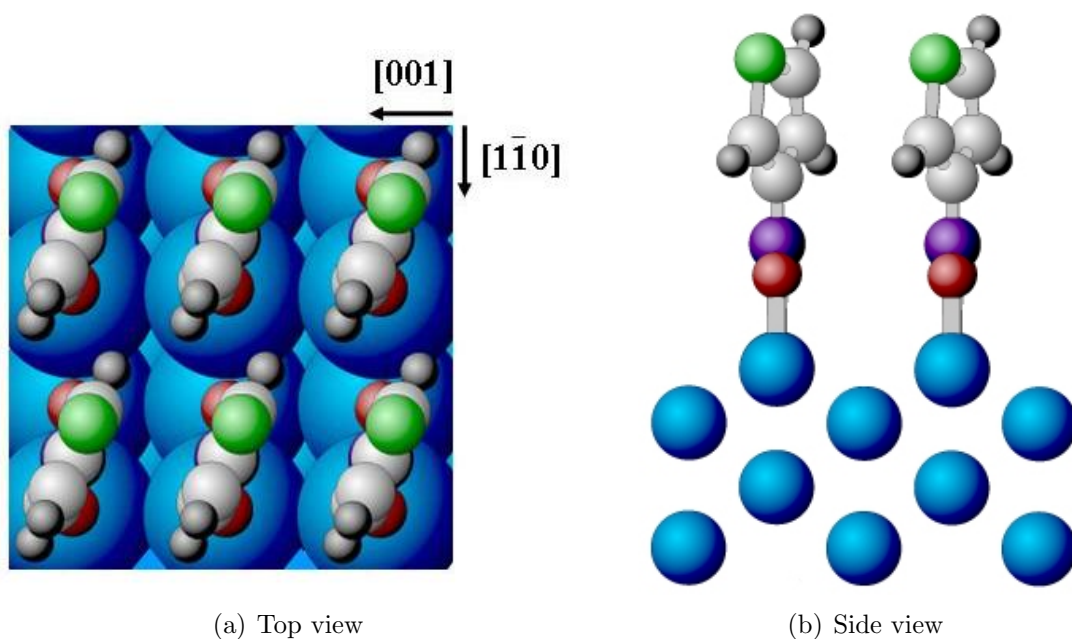


Figure 4.5: Rotation of the thiophene ring with respect to the $[1\bar{1}0]$ direction for the 'bridge' configuration. (a) Top view and (b) Side view

show the same trend as the one obtained for the single molecular case. Therefore, by increasing the atomic radius, from sulfur to selenium and tellurium atoms, the C-S/Se/Te bond length increases and the angle between them decreases.

ring	thiophene		selenophen		tellurophen	
Angle (degree)	bridge	top	bridge	top	bridge	top
$O_{24} - N_{30} - O_{26}$	124	121	124	121	123	120
$C_{20} - C_{16} - C_{18}$	114	114	116	116	119	119
$C_{22} - C_{20} - C_{16}$	112	112	114	114	117	117
$S_{28} - C_{22} - C_{20}$	112	112	112	112	112	112
$C_{16} - C_{18} - S_{28}$	111	111	111	110	111	111
$C_{18} - S_{28} - C_{22}$	92	92	87	87	82	81

Table 4.4: The angles in the conjugated ring and the nitro group for the optimized configurations of the adsorbed molecules of the adsorbed molecules.

4.4 Anchoring groups nitro versus carboxylate

In this section two anchoring groups, carboxylate and nitro, will be compared. For the anchoring nitro group, the results of the relaxed structures of the adsorbed molecules

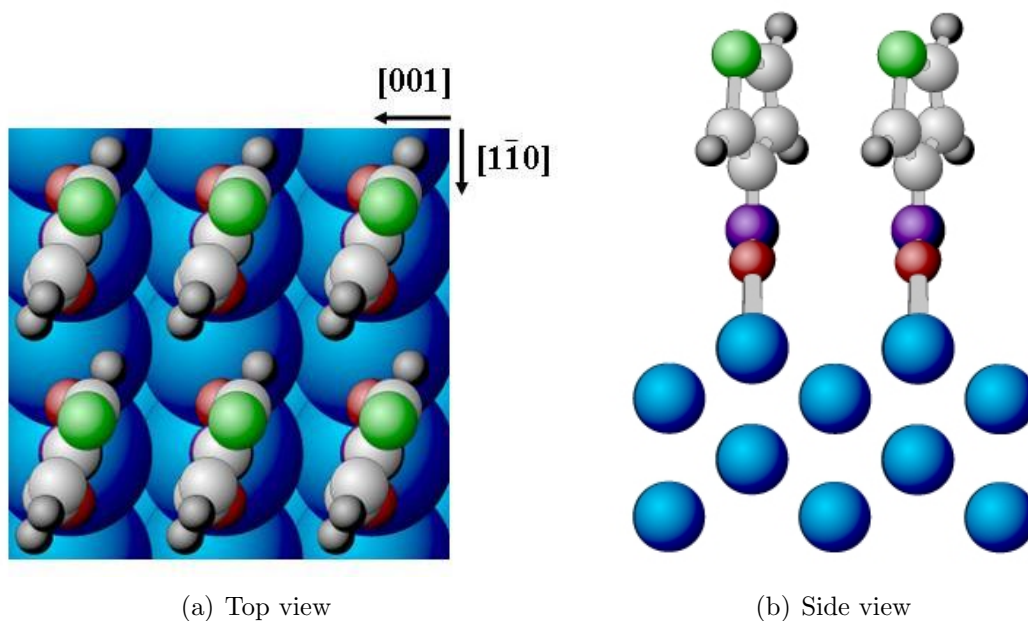


Figure 4.6: Rotation of the thiophene ring with respect to the $[1\bar{1}0]$ direction for the 'top' configuration. (a) Top view and (b) Side view

3-nitrothiophene/selenophen/tellurophen on Cu(110), Sec. 4.3.2, have been considered. These results are compared with the optimized configuration of the molecules with carboxylate group, 3-thiophene/selenophen/tellurophen carboxylate on Cu(110), [50]. For this comparison we have considered the structures of the 'bridge' configuration, since it is the more stable configuration. Table 4.6 contains the bond lengths in each group and the bonds between each group and the substrate. Furthermore, the adsorption enthalpy of the molecules with both nitro and carboxylate attached groups have been calculated using

$$\Delta H_{adsorption}|_{T=0} = \Delta E_{adsorption} = E_{total}(adsorbed\ molecule) - (E_{Cu(110)} + E_{single\ molecule}). \quad (4.1)$$

These calculations show that, the adsorption enthalpy for the molecules with anchoring nitro ($-NO_2$) group is larger than that of the molecules with carboxylate ($-CO_2$) group.

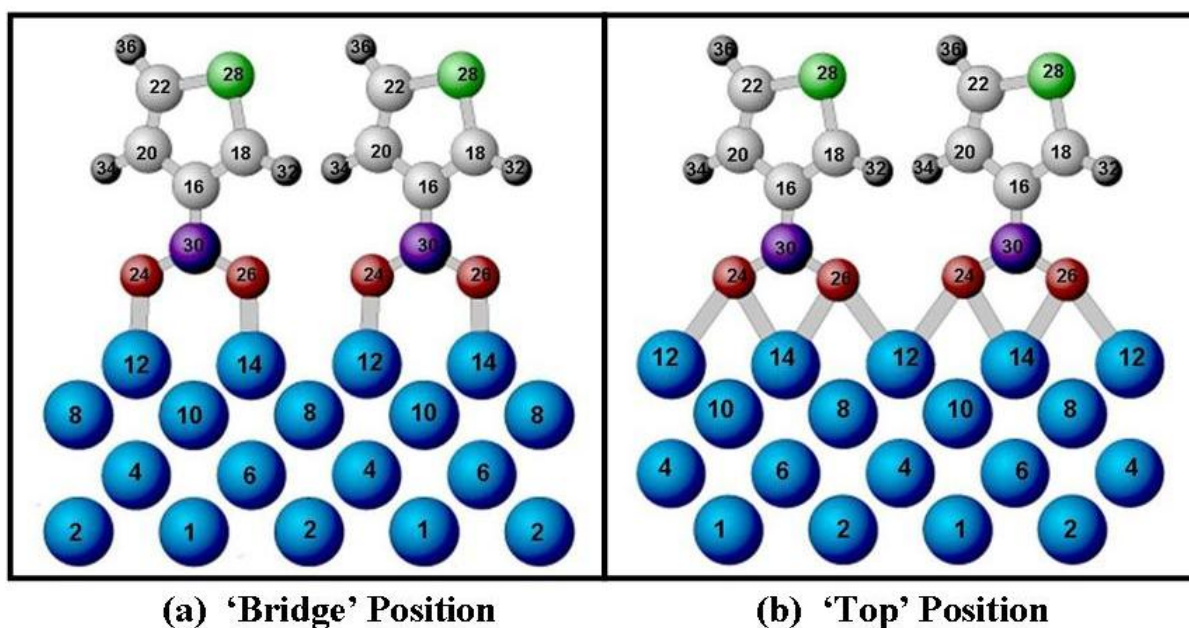


Figure 4.7: Side view ([100] direction) of the adsorbed 3-nitrothiophene on Cu(110). S-green, C-gray, O-red, N-purple, H-dark gray, Cu-blue.

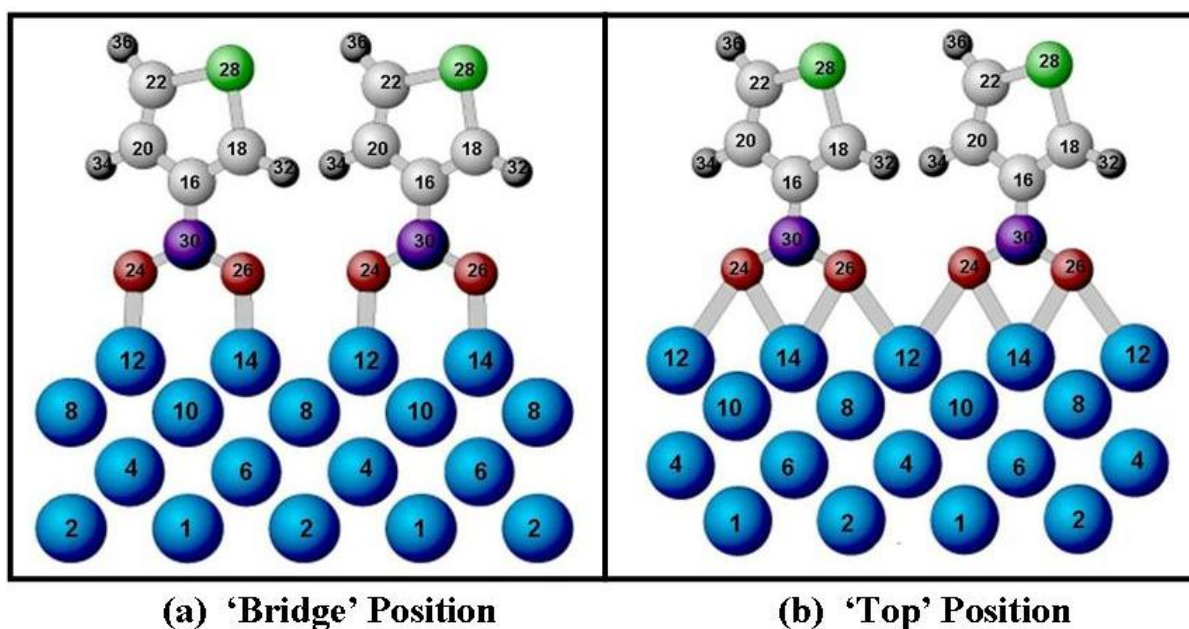


Figure 4.8: Side view ([100] direction) of the adsorbed 3-nitrothiophene on Cu(110). Se-green, C-gray, O-red, N-purple, H-dark gray, Cu-blue.

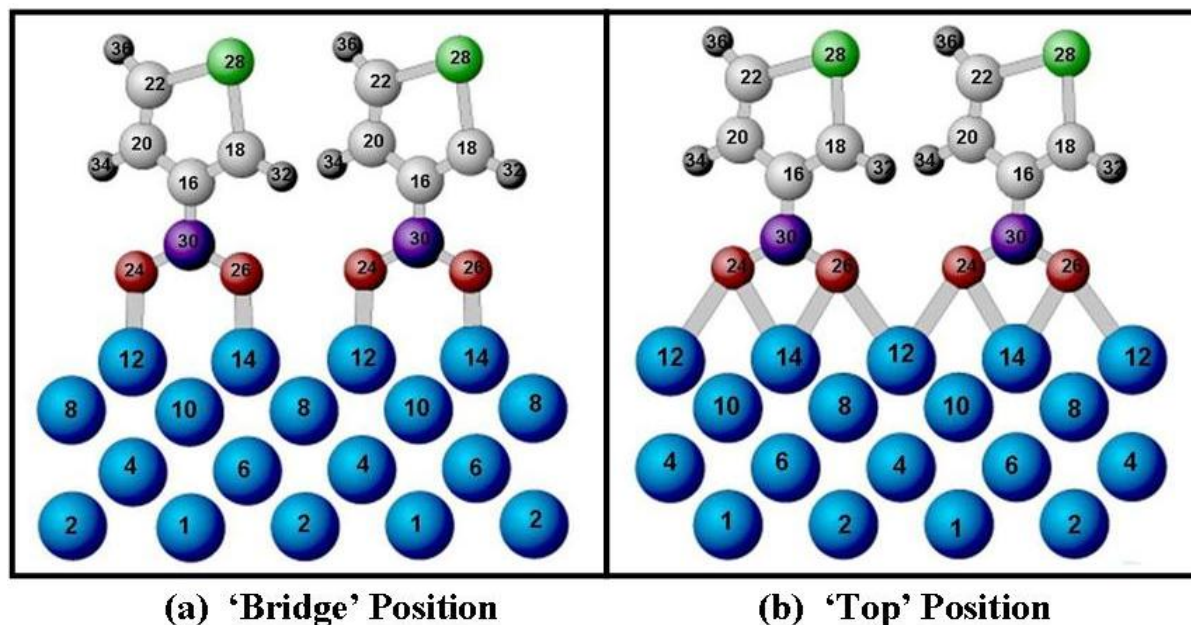


Figure 4.9: Side view ([100] direction) of the adsorbed 3-nitrothiophene on Cu(110). Te-green, C-gray, O-red, N-purple, H-dark gray, Cu-blue.

4.5 Summary and conclusions

These results show that the single molecules of 3-nitrothiophene/selenophen/tellurophen in the gas phase have a planar geometry. The comparison of the different conjugated rings (thiophene/selenophen/tellurophen) indicates that by increasing the atomic radius, from sulfur to selenium and tellurium atoms, the C-S/Se/Te bond length increases while the angle between these bond decreases. Our results show that C-S bond in the thiophene ring has the smallest length and C-S-C angle has the largest value.

Monolayers of 3-nitrothiophene/selenophen/tellurophen on Cu(110) surface are well ordered with the aromatic ring perpendicular to the surface, in the dense packed structure. Adsorption of the molecules on the surface breaks the planarity of single molecules. Due to the strong lateral interaction between the hydrogen atoms of the neighboring conjugated rings, they rotate relative to the nitro ($-NO_2$) group. The optimum rotation angles are obtained as 23° (for thiophene ring) to 25° (for selenophen ring) and 26° (for tellurophen ring). The optimization calculations show that the total energy of the rings consisting of larger atoms (selenium, tellurium) is more sensitive to the rotation angle of the ring.

Molecules are adsorbed on the surface in the two most probable configurations: 'bridge' and 'top'. The 'bridge' configuration is more stable with the 1 eV difference in the total energy. The detailed structures and binding information of these two configurations have been evaluated. The comparison of the two anchoring groups, nitro ($-NO_2$) and

ring	thiophene		selenophen		tellurophen	
Bond (\AA)	bridge	top	bridge	top	bridge	top
$O_{24} - N_{30}$	1.34	1.34	1.34	1.34	1.34	1.34
$O_{26} - N_{30}$	1.34	1.34	1.34	1.34	1.34	1.34
$O_{24} - Cu_{12}$	2.21	2.39	2.24	2.46	2.27	2.44
$O_{24} - Cu_{14}$	3.27	2.49	3.29	2.54	3.31	2.56
$O_{26} - Cu_{14}$	2.12	2.41	2.12	2.39	2.11	2.34
$O_{26} - Cu_{12}$	2.84	3.82	2.84	3.81	2.81	3.75
$N_{30} - C_{16}$	1.40	1.39	1.40	1.40	1.40	1.40
$C_{20} - C_{16}$	1.42	1.42	1.43	1.43	1.44	1.43
$C_{16} - C_{18}$	1.39	1.39	1.39	1.39	1.39	1.39
$C_{22} - C_{20}$	1.38	1.38	1.37	1.37	1.37	1.37
$C_{20} - C_{16}$	1.42	1.42	1.43	1.43	1.44	1.43
$S_{28} - C_{22}$	1.75	1.75	1.90	1.09	2.12	2.11
$C_{22} - C_{20}$	1.38	1.38	1.37	1.37	1.37	1.37
$C_{16} - C_{18}$	1.39	1.39	1.39	1.39	1.39	1.39
$C_{18} - S_{28}$	1.73	1.73	1.88	1.88	2.09	2.10
$C_{20} - H_{34}$	1.11	1.11	1.11	1.11	1.11	1.11
$C_{22} - H_{36}$	1.11	1.11	1.11	1.11	1.11	1.11
$C_{18} - H_{32}$	1.11	1.11	1.11	1.11	1.11	1.11

Table 4.5: The bonds in the conjugated ring and the nitro group for the optimized configurations of the adsorbed molecules.

ring	thiophene		selenophen		tellurophen	
group	$-NO_2$	$-CO_2$	$-NO_2$	$-CO_2$	$-NO_2$	$-CO_2$
Bond length (\AA)						
N/C-O	1.34	1.32	1.34	1.32	1.34	1.32
Cu-O	2.21	1.93	2.24	1.94	2.27	1.96
Angle (degree)						
O-N/C-O	124	127	124	128	123	128
$\Delta H_{adsorption}(eV)$	-0.72	-0.27	-0.31	-0.06	-0.58	+0.85

Table 4.6: Comparison of the two anchoring groups, nitro and carboxylate.

carboxylate ($-CO_2$), show that the adsorption enthalpy for the molecules with anchoring nitro ($-NO_2$) group is larger than the ones with carboxylate ($-CO_2$) group.

5 Optical properties of organic materials

The optical properties of organic materials have become a foremost topic since the 1990s, mainly as a result of technological advances that have led to the development of a whole range of organic electroluminescent devices and organic light emitting diodes (OLEDs). The optical properties of organic materials are different to that of the inorganic ones. For the case of inorganic materials, the solid is held with strong covalent or ionic bonds. This yields broad bands with delocalized electronic states. However, the organic solids are held together by weak van der Waals type interactions. These interactions are relatively weak compared to the covalent bond between the atoms within the molecule. Therefore, the electronic and vibrational states of the solids are mainly localized near each single molecule. On the contrary, the optical properties of the inorganic materials are governed by the delocalized states. The optical properties of organic solids are determined by the electronic states of the individual molecules. The optical transition simultaneously changes the electronic and vibrational state of the molecule. The same as electronic states, vibrational states are also mainly localized on each single molecule. The most important phonons of molecular solids are localized modes with discrete frequencies. Strong covalent bonds hold the atoms in each molecule together. Hence, the atoms in a molecule can vibrate about their bonds, which gives the molecule vibrational energy in addition to its electronic energy. These are essentially just the vibrational modes of the constituent molecules, perhaps with their frequencies slightly altered in the condensed phase. There will, of course, be delocalized phonon bands present in organic solids, but these play a secondary role in the optical properties in most instances. [8]

It should be noted that, the localized nature of the electronic and vibrational states means that the optical properties of the solid are similar to those of the single molecules. Hence, in order to explain the optical properties of organic solids, we need to understand the electronic and vibronic transitions in individual molecules. In the following sections, we will first start the chapter with a brief summary of the chemical structures of organic compounds. We then consider the basic principle of optical transitions. Then, we continue further with the basic principles of vibronic transitions in isolated molecules. These will provide us with the knowledge that leads us to the goal of explaining the physical principle of organic optoelectronics.

5.1 Different organic compounds

As we have mentioned above, the knowledge about organic molecules is necessary before we can understand molecular solids in any detail. In this section we will give an overview about different types of organic molecules which are classified depending on type of bonding in the molecule as well as their structures. In general, organic compounds can be classified into either saturated or conjugated systems.

In saturated compounds, the valence electrons are held in strong localized bonds between neighboring atoms. This means that all the electrons are tightly held in their bonds, and can only respond at high frequencies in the ultraviolet spectral range. Therefore, they are usually colorless and do not absorb in the visible region. Their optical properties is not significantly different to that of insulators or glasses. Plastics are an example of saturated compounds.

Organic molecules, like benzene, with alternating double and single bonds are named as conjugated molecules. Conjugated molecules have much more interesting properties. The chemistry of these molecules is based on the π orbitals between the carbon atoms in the whole molecule. These delocalized π orbitals are formed by the electrons from the p -like atomic states of the carbon atoms. π electrons are less tightly bonded than the ones in saturated molecules. Therefore, they can respond to lower frequencies. As the standard example, benzene (C_6H_6) molecule, have the ring-like π orbitals above and below the molecular plane. The absorption edge in benzene is placed in the ultraviolet, but for the other large molecules it is shifted to the visible range. Therefore, these molecules are good candidates for the technological applications such as LEDs.

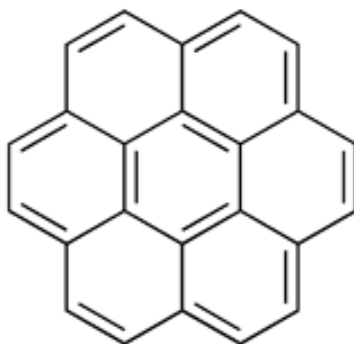
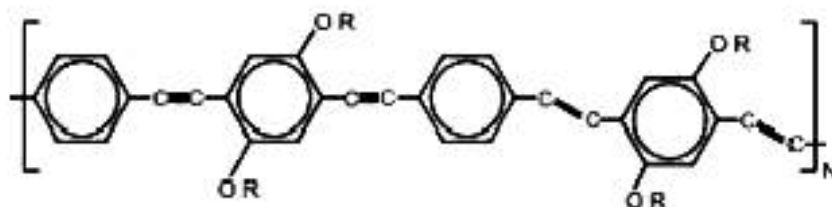
Conjugated organic compounds can be classified into two main groups (Fig.5.1) , according to their structures:

- conjugated polymers
- aromatic hydrocarbons

Conjugated polymers, are long chain molecules made by bonding many individual molecular units ('monomers') together. In these molecules π electrons are delocalized along the chain, and they have linear conjugation. The aromatic hydrocarbons, on the other hand, are carbon-hydrogen compounds containing benzene rings in their structure. The aromatic hydrocarbons have cyclic periodicity of the electron wave-function and cyclic conjugation.

5.1.1 Electronic states in conjugated molecules

In this section we will present a brief summary of the electronic states that determine the optical properties of conjugated molecular solids. In fact, the covalent bonds between the

(a) Coronene($C_{24}H_{12}$)

(b) DE15:poly(1,4-phenyleneethyne-1,4-(2,5-didodecyloxyphenylene)-1,4-phenyleneethene-1,2-diyl-1,4-(2,5-didodecyloxyphenylene)ethene-1,2-diyl)

Figure 5.1: Examples of an aromatic hydrocarbon (a) and a conjugated polymer (b).

carbon atoms of organic molecules are controlling the chemistry of these molecules. Each carbon atom has six electrons with four electrons in valence state ($n=2$) and the electronic configuration of $1s^2 2s^2 2p^2$. In organic solids, carbon atoms may form, single, double, or triple bonds between adjacent carbon atoms. In molecules with double or triple bonds, the valence electrons are divided between the σ bonds and the π bonds. Now, the simple aromatic molecule, benzene (C_6H_6) is considered (Fig. 5.2). This is a planar molecule with the six carbon atoms arranged as a hexagon. Each carbon atom is bonded to one hydrogen atom, and has a double bond with the adjacent two carbon atom. From the valence electrons of each carbon atom, the one $2s$ electrons hybridize with one one of the $2p$ ones to form three sp^2 bonds. They form σ bonds with one hydrogen atom and two neighboring carbon atoms. The other $2p$ electron from the valence state, form π orbitals derived from the $2p_z$ atomic orbital. The wave functions of these π electrons have a ring shape above and below the molecular plane. The π electrons are shared equally between the two bonds on either side of each carbon atom.

In the small scales of the order of the few molecules, the optical properties of solids depend on their size. This has been explained as the quantum confinement theory. This theory is based on the Heisenberg uncertainty principle which indicates for a particle confined to a region of length Δx , there is an uncertainty in its momentum, given by $\Delta p_x \sim \hbar/\Delta x$.

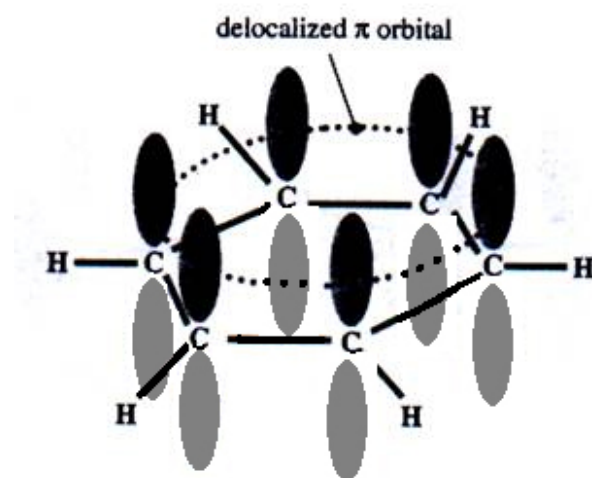


Figure 5.2: The benzene molecule (C_6H_6). The π electrons form a delocalized ring orbital above and below the plan of the hexagon defined by the six carbon atoms.

For a free particle with mass m , the confinement energy is

$$E_{\text{confinement}} = \frac{(\Delta p_x)^2}{2m} \sim \frac{\hbar^2}{2m(\Delta x)^2}. \quad (5.1)$$

In the molecular conjugated compounds, π electrons are spread in large delocalized orbitals. The spreading of the π electron wave function leads to a reduction in the energy. Increasing the number of these delocalized π electrons, can reduce the confinement energy. As an example, one may compare the lowest electronic transition energy of ethylene with the equivalent transition in benzene. This transition occurs for ethylene with two π orbitals at 6.9 eV while for benzen with six π orbitals at 4.6 eV. Using larger conjugated molecules can reduce the transition energy even more, and push it down into visible spectral region. This arises particular interests to the transitions of the π electrons in large conjugated molecules. In general, the reduction in the transition energy for the larger molecules (such as benzen) in comparison with the smaller ones (such as ethylene) can be explained by considering the ideas of quantum confinement theory. However, the exact quantitative description of the difference between the lowest transition energies of these two molecules can not be explained completely only by considering Eq. 5.1. The other important terms that contributes in the transition energies of molecular compounds are the HOMO-LUMO band gap (Fig. 5.3), the excitonic effect and the strong electron-phonon coupling. The strength of these effects is different for different organic molecules, and depends on the number of the π states of the molecule. These effects will be explained in more detail in the following sections of (5.3),(5.2.3) and (5.2.5).

Figure 5.3 shows a schematic diagram of the electronic states of a typical conjugated molecule. The molecular orbitals are filled up by the electrons of the constituent atoms, all paired off in bonds. The highest occupied molecular orbital (HOMO) is the highest

filled energy state. The first energy state above the HOMO is called LUMO which is lowest unoccupied molecular orbital. In conjugated molecules, HOMO level will be a π orbital, since the σ bonds consist of the tightly bound electrons. For these molecules, LUMO will be an excited configuration of π orbitals, labeled as π^* state. Therefore, the lowest electronic transition occurs as a π electron is promoted to a π^* state. On the other hand, transitions of the σ electrons to the σ^* excited states occur at much higher energies, because it takes a large amount of energy to break a σ bond.

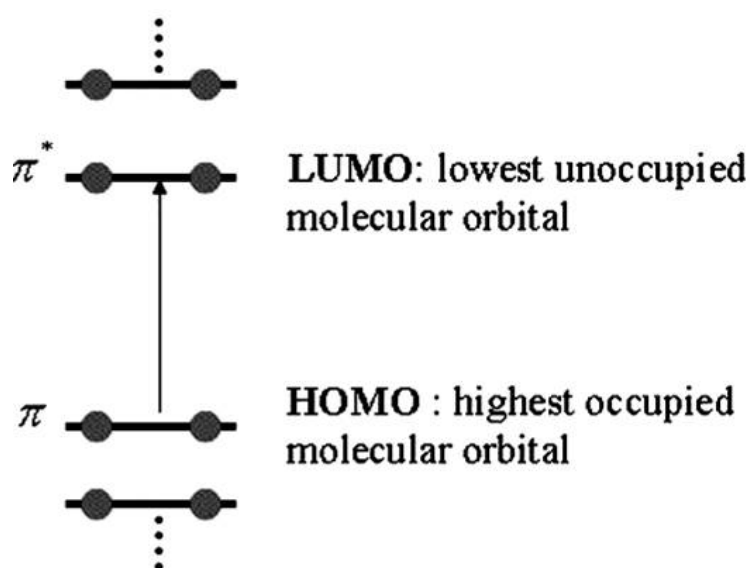


Figure 5.3: Schematic energy level diagram for a conjugated molecule. The lowest energy electronic transition takes place between the HOMO (highest occupied molecular orbital) and the LUMO (lowest unoccupied molecular orbital) state. This is a $\pi \rightarrow \pi^*$ transition.

The ground state of a molecule, HOMO level, is a singlet state, since all its electrons are paired off with their spin antiparallel. However, the excited state could be either a singlet or triplet. This is due to the fact that the excitation process puts an unpaired electron in the excited state and leaves an unpaired electron in the HOMO state. (fig. 5.4) According to the spin selection rule, the main optical transition is $S_0 \rightarrow S_1$ singlet-singlet transition. However, spin-orbit coupling allows some probability of triplet-singlet transitions. The single excited states have a short lifetime of order 1-10 ns due to the dipole-allowed transitions to the S_0 ground state. The low probability of the $T_1 \rightarrow S_0$ transition, on the other hand, leads to a long radiative lifetime of the triplet state. In order to distinguish these two types of transitions, the fast singlet-singlet transition is noted as *fluorescence* while the slow singlet-triplet transition is named **phosphorescence** (Fig. 5.5).

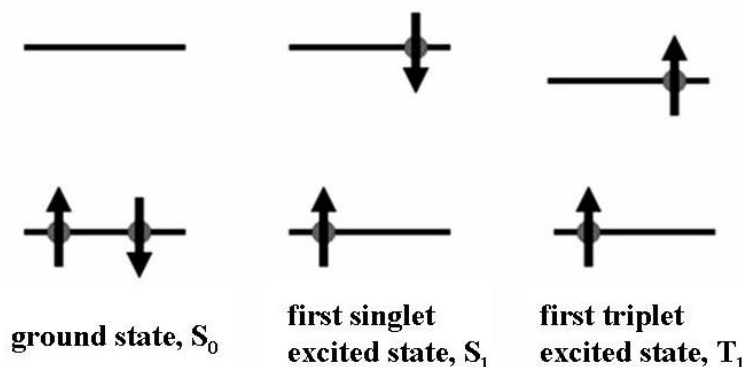


Figure 5.4: The unpaired electrons of an excited molecule can either have their spins antiparallel or parallel. The states with antiparallel spins have spin quantum number $S=0$ and are called singlets after their multiplicity. The states with parallel spins have $S=1$ and are called triplets. The ground state is always a singlet. [8]

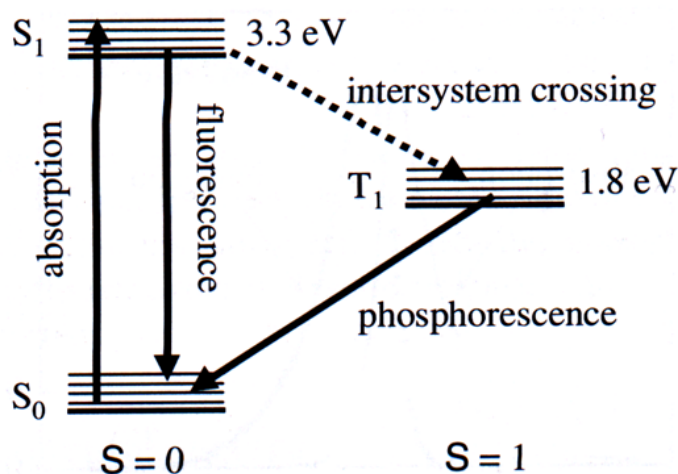


Figure 5.5: Level diagram for the anthracene molecule. Absorption and fluorescence transitions can occur between the S_0 excited state. Phosphorescent transitions from T_1 state to the ground state occur on a slow time scale. Electrons in the S_1 state have a small probability of transferring non-radiatively to the T_1 state by intersystem crossing. [8]

5.2 Electrons in a radiation field

In order to explain the optical properties of molecules in different spectral regions, we need to understand the general basis of the effect of a radiation field on the electronic states. In this section we will start with a general theoretical basis for direct band-to-band, electronic, transitions. Then, we continue to study the indirect band-to-band, vibrational-electronic, transitions and electron-phonon coupling. [51]

5.2.1 Band-to-band optical transitions

The effect of a radiation field on the electronic states of the solid can be expressed by the following Hamiltonian: [52]

$$H_{eR} = \frac{e}{mc} \sum_{i=1}^N \mathbf{A}(\mathbf{r}_i, t) \cdot \mathbf{P}_i. \quad (5.2)$$

where e is the absolute value of the electron charge, \mathbf{A} is the vector potential of the electro-magnetic field and P_i is the momentum of a charged particle.

The effect of a radiation field on the electronic states of a solid can be studied by treating H_{eR} as a time dependent perturbation acting on the electronic states. This time dependent term will cause electrons to make transitions between occupied and empty bands. From the transition probability rate, the relationship between the electronic structure and phenomenological optical constants can be derived.

From elementary quantum mechanics we know that, to first order perturbation theory, the probability per unit time that a perturbation induces a transition from the initial state $|i\rangle$ of energy E_i to the final state $|f\rangle$ of energy E_f is

$$\mathcal{P}_{i \rightarrow f} = \frac{2\pi}{\hbar} |\langle f | \mathcal{L} | i \rangle|^2 \delta(E_f - E_i \mp \hbar\omega). \quad (5.3)$$

where, $\mathcal{L}e^{-i\omega t}$ is the time dependent perturbation. The above relation declare that a perturbation $\mathcal{L}e^{-i\omega t}$ induces transitions with absorption of a quantum $\hbar\omega$, while a perturbation $\mathcal{L}e^{i\omega t}$ gives rise to emission of a quantum $\hbar\omega$. If the initial state is the ground state, the emission term makes expression Eq. 5.3 to vanish. Thus only the absorption term needs to be considered in order to discuss the optical excitation spectrum of a solid in the ground state. The emission term in Eq. 5.3 is relevant in discussing the radiative emission due to electrons in excited states (luminescence, phosphorescence, and pair recombination at impurity centers). We will neglect the emission term in the present treatment, keeping in mind that it could be considered, when needed, just by putting the appropriate sign into the argument of the δ function.

To the second order, the transition probability rate is

$$\mathcal{P}_{i \rightarrow f} = \frac{2\pi}{\hbar} \left| \sum_{\beta} \frac{\langle f | \mathcal{L} | \beta \rangle \langle \beta | \mathcal{L} | i \rangle}{E_{\beta} - E_i \mp \hbar\omega} \right|^2 \delta(E_f - E_i \mp \hbar\omega \mp \hbar\omega). \quad (5.4)$$

where $|\beta\rangle$ indicates all intermediate states including initial and final states. The matrix elements appearing in Eq. 5.4 can be regarded as a result of two successive processes, firstly, the system makes a transition from the state $|i\rangle$ to the state $|\beta\rangle$, and, secondly,

from $|\beta\rangle$ to $|f\rangle$. Energy is not conserved in the intermediate transition; it is only conserved between the initial and the final states.

We now calculate the contribution to the optical constants due to a couple of valence and conduction bands. The ground state of the electronic system, Ψ_0 , can be considered (in the adiabatic and one-electron approximation) as a Slater determinant of the single electron wave functions in the valence band. A trial excited state Ψ' is the same state as Ψ_0 , only having one excited electron for which the conduction wave function is replaced by the valence wave function. The matrix elements of the operator H_{eR} (defined in Eq. 5.2) between the ground state and the excited states needs to be calculated. Since H_{eR} is a sum of one-particle operators, the non-vanishing matrix elements connect the ground state Ψ_0 with states Ψ' having only one electron which is excited. Hence, we can write

$$\langle \Psi' | H_{eR} | \Psi_0 \rangle = \frac{e}{mc} \langle \psi_{ck_f s_f} | \mathbf{A} \cdot \mathbf{P} | \psi_{vk_i s_i} \rangle = \frac{e}{mc} \delta_{s_i, s_f} \langle \psi_{ck_f} | \mathbf{A} \cdot \mathbf{P} | \psi_{vk_i} \rangle. \quad (5.5)$$

Here, s is the spin index, \mathbf{A} is the vector potential with a frequency ω and polarization vector \mathbf{e} in the direction of the electric field.

Considering the direct transition, and since \mathbf{k}_i and \mathbf{k}_f are confined to the first Brillouin zone, we may write

$$\mathbf{k}_i \simeq \mathbf{k}_f \quad (5.6)$$

We thus arrive at the result that only "vertical" transitions can be induced in an energy band diagram by the radiation field. [51] We can therefore simplify the expression for the probability per unit time as

$$\mathcal{P}_{vks \rightarrow cks} = \frac{2\pi}{\hbar} \left(\frac{eA_0}{mc} \right)^2 |\mathbf{e} \cdot \mathbf{M}_{cv}(\mathbf{k})|^2 \delta(E_c(\mathbf{k}) - E_v(\mathbf{k}) - \hbar\omega), \quad (5.7)$$

where

$$\mathbf{e} \cdot \mathbf{M}_{cv}(\mathbf{k}) = \langle \psi_{c\mathbf{k}} | \mathbf{e} \cdot \mathbf{p} | \psi_{v\mathbf{k}} \rangle = \mathbf{e} \cdot \int_{\text{volume}} \psi_c^*(\mathbf{k}, \mathbf{r}) (-i\hbar \nabla) \psi_v(\mathbf{k}, \mathbf{r}) d\mathbf{r}. \quad (5.8)$$

To obtain the number of transitions $W(\omega)$ per unit volume induced by light with frequency ω , we must sum Eq. 5.7 over all possible states in the unit volume, i.e. we must sum over \mathbf{k} , the spin variable s , and over the band indices v (occupied) and c (empty). Since the allowed \mathbf{k} vectors are distributed in the Brillouin zone with a density $V/(2\pi)^3$ (V being the crystal volume),

$$W(\omega) = \frac{2\pi}{\hbar} \left(\frac{eA_0}{mc} \right)^2 \sum_{v,c} \int_{BZ} \frac{2d\mathbf{k}}{(2\pi)^3} |\mathbf{e} \cdot \mathbf{M}_{cv}(\mathbf{k})|^2 \delta(E_c(\mathbf{k}) - E_v(\mathbf{k}) - \hbar\omega), \quad (5.9)$$

where the integral extends over the first Brillouin zone and the factor of 2 arises from the integration of spin variables.

5.2.2 Connection with the optical constants

The optical constants which are used phenomenologically to describe the optical properties of matter, could be related to the expression of Eq. 5.9 if all relevant transitions are included. [53], [52], [54] Optical properties can be described in terms of the complex dielectric function $\epsilon = \epsilon_1 + i\epsilon_2$ or the complex refraction index $N = n + ik$, where n is the ordinary refraction index and k is known as the extinction coefficient. The optical constants ϵ and N are connected by the relation $\epsilon = N^2$, and the absorption coefficient α depends on the above optical constants via

$$\alpha = \frac{2k\omega}{c}, \quad (5.10)$$

$$\alpha = \frac{\omega}{nc} \epsilon_2. \quad (5.11)$$

The average density u in a medium of a radiation field described by the vector potential \mathbf{A} , is related to the optical constants through the relation

$$u = \frac{n^2 A_0^2 \omega^2}{2\pi c^2}. \quad (5.12)$$

It is also known that the radiation in the medium propagates with velocity c/n . Using Eq. 5.9 we can now obtain microscopic expressions for the absorption coefficient and the other band constants. The absorption coefficient is by definition the energy absorbed in the unit time in the unit volume divided by the energy flux

$$\alpha(\omega) = \frac{\hbar\omega W(\omega)}{u \times (c/n)}, \quad (5.13)$$

where $\hbar\omega W(\omega)$ is the energy absorbed per unit volume and time, and the energy flux $u \times (c/n)$ is the product of the energy density by the velocity of propagation in the medium. We thus obtain for the absorption coefficient

$$\alpha(\omega) = \frac{4\pi^2 e^2}{ncm^2\omega} \sum_{v,c} \int_{BZ} \frac{2d\mathbf{k}}{(2\pi)^3} |\mathbf{e} \cdot \mathbf{M}_{cv}(\mathbf{k})|^2 \delta(E_c(\mathbf{k}) - E_v(\mathbf{k}) - \hbar\omega). \quad (5.14)$$

Using Eq. 5.11

$$\epsilon_2(\omega) = \frac{4\pi^2 e^2}{m^2\omega^2} \sum_{v,c} \int_{BZ} \frac{2d\mathbf{k}}{(2\pi)^3} |\mathbf{e} \cdot \mathbf{M}_{cv}(\mathbf{k})|^2 \delta(E_c(\mathbf{k}) - E_v(\mathbf{k}) - \hbar\omega). \quad (5.15)$$

This is the basic expression which connects the band structure with the optical properties; it is preferred over related expressions for other optical constants because it does not depend on the refractive index.

The expression for $\epsilon_1(\omega)$ can be obtained using the dispersion relation of Kramers-Kronig

$$\epsilon_1(\omega) = 1 + \frac{2}{\pi} P \int_0^\infty \omega' \epsilon_2(\omega') \frac{1}{\omega'^2 - \omega^2} d\omega', \quad (5.16)$$

where P indicates the principal part. By direct substitution of Eq. 5.15 into Eq. 5.16,

$$\epsilon_1(\omega) = 1 + \frac{8\pi e^2}{m^2} \sum_{v,c} \int_{BZ} \frac{2d\mathbf{k}}{(2\pi)^3} \frac{|\mathbf{e} \cdot \mathbf{M}_{cv}(\mathbf{k})|^2}{[E_c(\mathbf{k}) - E_v(\mathbf{k})]/\hbar} \frac{1}{[E_c(\mathbf{k}) - E_v(\mathbf{k})]^2/\hbar^2 - \omega^2} \quad (5.17)$$

The relation Eq. 5.15 and Eq. 5.17 allow in principle the computation of all optical constants once the band structure is known.

The optical constants satisfy some general relations which are often used to test the consistency of the approximations involved in their computation. [54], [55], [56] A very useful relation is the sum rule

$$\int_0^\infty \omega \epsilon_2(\omega) d\omega = \frac{\pi}{2} \omega_p^2, \quad (5.18)$$

where the plasma frequency ω_p is given by

$$\omega_p = \left(\frac{4\pi n e^2}{m} \right)^{1/2} \quad (5.19)$$

and n denotes the density of the electrons which take part in the transition. Another useful sum rule is obtained as a particular case of the dispersion relation Eq. 5.16, taking the limit $\omega \rightarrow 0$

$$\epsilon_1(0) = 1 + \frac{2}{\pi} \int_0^\infty \frac{\epsilon_2(\omega)}{\omega} d\omega. \quad (5.20)$$

Two particularly important sum rules on the index of refraction for isotropic media are

$$\int_0^\infty [n(\omega) - 1] d\omega = 0 \quad (5.21)$$

and

$$\int_0^\infty \omega k(\omega) d\omega = \frac{\pi}{4} \omega_p^2. \quad (5.22)$$

5.2.3 Indirect band-to-band transitions: general remarks on electron-phonon interaction

In the previous section, the interaction of the electrons with the radiation field has been considered, and it has been mentioned that only vertical transitions may occur. For a number of materials such as organic solids, semiconductors (silicon, germanium, etc.) and insulators like AgCl, their electronic structure is characterized by the fact that the bottom of the conduction band (HOMO level in case of organic materials) and the top of the valence band (LUMO level for organic materials) are at different points of the Brillouin zone. Transitions between states which are not vertical in an energy band diagram are called indirect transitions. The possibility of indirect transitions is due to the interaction of the electrons with the vibrations of the lattice. The theory was first provided by Bardeen *et al* [57] in order to explain the absorption tail of germanium.

It is well known that one can describe the motion of nuclei in the adiabatic approximation by a system of independent harmonic oscillators. This approximation is valid in the case that the total potential energy is expanded up to second order in the nuclear displacements from the equilibrium position and the normal coordinates are introduced. Corresponding to every normal mode of wave vector \mathbf{q} there is an harmonic oscillator whose energy can be an integer multiple of $\hbar\omega_{\mathbf{q}}$. The frequency $\omega_{\mathbf{q}}$ as a function of momentum gives the classical vibrational dispersion spectrum which is called as phonons. At a given \mathbf{q} vector of the Brillouin zone the phonon states can be classified according to the irreducible representations of the group of vector \mathbf{q} . Their number is given by the number of degrees of freedom of the atoms in the unit cell.

Even in the adiabatic approximation the presence of the phonon field produces an electron-lattice/electron-molecule interaction. In fact, during the vibrations of the lattice/molecules the atoms are displaced from their regular positions, and the actual potential on any of the electrons is consequently changed. To illustrate typical consequences of electron-molecule interaction, we consider a simplified model in which the electron potential is taken as a sum of superimposed atomic-like potentials rigidly following the displacements of the nuclei. In the above approximation the electron-lattice/electron-molecule perturbation Hamiltonian H_{eL} can be written as

$$H_{eL} = \sum_{\mathbf{R}_a} [V(\mathbf{r} - \mathbf{R}_a - \delta\mathbf{R}_a) - V(\mathbf{r} - \mathbf{R}_a)], \quad (5.23)$$

where the sum runs over all the equilibrium atomic positions \mathbf{R}_a in the crystal/molecule, $\delta\mathbf{R}_a$ represents the vibrational displacement, and $V(\mathbf{r} - \mathbf{R}_a)$ is atomic-like potential corresponding to the atom placed at \mathbf{R}_a . We expand Eq. 5.23 in terms of $\delta\mathbf{R}_a$ and retain the first order term

$$H_{eL} = \sum_{\mathbf{R}_a} \delta\mathbf{R}_a \cdot \nabla_{\mathbf{r}} V(\mathbf{r} - \mathbf{R}_a). \quad (5.24)$$

The electron-lattice interaction Eq. 5.24 can be written separately as a sum of terms, each appropriate for a given phonon of a given branch, as an electron-phonon interaction of the type

$$H_{ep} = A(\mathbf{q})e^{-i\omega_{\mathbf{q}}t}V_p(\mathbf{q},\mathbf{r}) + c.c. \quad (5.25)$$

with

$$V_p(\mathbf{q},\mathbf{r}) = \left(\frac{\hbar}{2M\omega_{\mathbf{q}}}\right)^{1/2} \sum_{\mathbf{R}_a} e^{i\mathbf{q}\cdot\mathbf{R}_a} \mathbf{e}_a \cdot \nabla_{\mathbf{r}} V(\mathbf{r} - \mathbf{R}_a).$$

where \mathbf{e}_a is an appropriate polarization vector corresponding to a phonon of momentum \mathbf{q} and frequency ω , M indicates the mass of crystal/molecule unit cell and *c.c.* indicates the complex conjugate of the first term. [51] In the above equation, $A(\mathbf{q})$ and $A^*(\mathbf{q})$ are the annihilation and creation operators respectively. The normalization factor $(\hbar/2M\omega)^{1/2}$ has been introduced so that the matrix elements of $A(\mathbf{q})$ and $A^*(\mathbf{q})$ between multiphonon wave functions satisfy the condition [58]

$$\begin{aligned} \langle n_q - 1 | A(\mathbf{q}) | n_q \rangle &= \sqrt{n_q}, \\ \langle n_q + 1 | A^*(\mathbf{q}) | n_q \rangle &= \sqrt{n_q + 1}, \end{aligned} \quad (5.26)$$

where $|n_q\rangle$ indicates a state with phonon occupation number n_q .

The theory of electronic-vibrational transitions can be developed by considering molecule vibrational energy in addition to its electrical energy,

$$E = E_{eR} + E_{ep}. \quad (5.27)$$

As shown in Fig. 5.6, a series of vibrational levels must be associated with each electronic state. The energy of a vibrational oscillation, E_{ep} with frequency ω_q is equal to $(n_q + \frac{1}{2})\hbar\omega_q$, where n_q is the phonon occupation number. Hence, the electronic-vibrational energy of such molecule, at the electronic state of E_i and vibrational frequency ω_q can be written as $E = E_i + (n_q + \frac{1}{2})\hbar\omega_q$.

Figure 5.6 indicates an optical transition in which an electron is promoted from the ground state, with n_1 excited quanta of frequency ω_1 , to the excited state, with n_2 excited quanta of frequency ω_2 , by absorbing a photon. We assume that the molecule is initially in the $n_1 = 0$ vibrational level of the ground state. Conservation of energy during absorption process yields:

$$\begin{aligned} \hbar\omega_a &= (E_2 + (n_2 + \frac{1}{2})\hbar\omega_2) - (E_1 + \frac{1}{2}\hbar\omega_1) \\ &= \hbar\omega_0 + n_2\hbar\omega_2 \end{aligned} \quad (5.28)$$

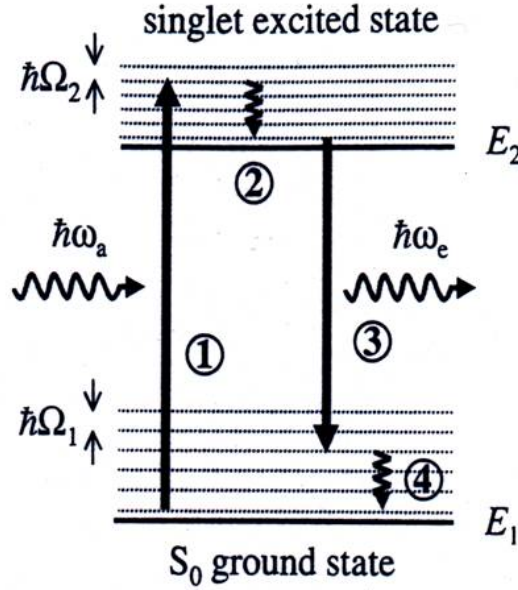


Figure 5.6: Schematic diagram of the vibrational-electronic transitions in a molecule. The four processes indicated are respectively : (1) absorption; (2) non-radiative relaxation; (3) emission and (4) non-radiative relaxation.

where ω_a is the angular frequency of the absorbed photon, and

$$\hbar\omega_0 = (E_2 - E_1 + \frac{1}{2}\hbar(\omega_2 - \omega_1)). \quad (5.29)$$

This absorption process involves both the electron jump to the excited electronic state, and simultaneously creation of vibrational quanta which yield a large amount of vibrational energy. The corresponding vibrational-electronic states consist of a series of discrete lines, since n_2 can only take integer values (Eq. 5.28). Further rapid radiationless relaxation processes, as indicated in Fig. 5.6, brings the molecule to its minimum vibronic energy state. This rapid relaxation occurs by spreading the vibrational energy of the individual excited molecule throughout the rest of the system. This process is followed further by returning the molecule to the ground state during the emission process which produces a photon with energy $\hbar\omega_e$, as shown in Fig. 5.6. Hence, the molecule is left in an excited vibrational level of the ground state. The frequency of the photon is given by:

$$\begin{aligned} \hbar\omega_e &= (E_2 + \frac{1}{2}\hbar\omega_2) - (E_1 + (n_1 + \frac{1}{2})\hbar\omega_1) \\ &= \hbar\omega_0 - n_1\hbar\omega_1 \end{aligned} \quad (5.30)$$

The emission spectrum, as well as absorption one, consists of a series of discrete vibrational-electronic lines with frequencies given by Eq. 5.30. During the further ra-

diationless relaxation process, the molecule finally loses its excess vibrational energy and returns to the $n_1 = 0$ level of the ground state, as shown in Fig. 5.6. Comparison of Eq. 5.28 and Eq. 5.30, depicted that the absorption occurs at a higher energy than the emission, except for the cases when no vibrational state are excited during the electronic transitions. The difference in energy between the maximum absorption and the maximum emission is called the *Stokes shift*. This phenomenon is hence quite different from transitions, during which the absorption and emission frequencies coincide.

5.2.4 The Franck-Condon principle

The *Franck-Condon principle* is a rule in spectroscopy and quantum chemistry that explains the intensity of vibronic transitions. Vibronic transitions are the simultaneous changes in electronic and vibrational energy levels of a molecule due to the absorption or emission of a photon of the appropriate energy. The principle states that during an electronic transition, a change from one vibrational energy level to another will be more likely to happen if the two vibrational wave functions overlap more significantly. As a consequence of the fact that electrons are much lighter than the nuclei and considering the Born-Oppenheimer approximation, the Franck-Condon principle, in classical view, tells that the electronic transitions take place so rapidly that the nuclei do not move significantly during the transition. In the quantum mechanical picture, the vibrational levels and vibrational wavefunctions are those of quantum harmonic oscillators, or of more complex approximations to the potential energy of molecules. The vibronic transition is indicated by a vertical arrow due to the assumption of constant nuclear coordinates during the transition. The Franck-Condon principle is a statement on allowed vibrational transitions between two different electronic states, other quantum mechanical selection rules may lower the probability of a transition or prohibit it altogether. The probability that the molecule can end up in any particular vibrational level is proportional to the square of the (vertical) overlap of the vibrational wavefunctions of the original and final state (see Eq. 5.34).

For the case of a simple molecule with two atoms, Fig. 5.7, photon absorption and emission can be explained according to the Franck-Condon principle. The mean nuclear distance of atoms is r_1 for the ground state. By absorbing a photon, an electron from the ground state is promoted to an excited state without changing the nuclear separation distance, r_1 . The separation of the nuclei relaxes to r_2 before re-emitting a photon. This leaves the molecule in the vibrational ground state (but electronically excited state) with a mean nuclear separation of r_2 . Further rapid relaxation processes occur to complete the cycle and bring the molecule back to its equilibrium separation in the ground state. It should be noted that, the vibrational relaxation typically occurs in less than 1 ps in a solid, which is much faster than the ~ 1 ns taken to re-emit a photon.

As shown in Fig. 5.8, the optical transitions are represented by vertical arrows in configuration diagrams. Photon absorption excites molecular vibronic as well as electronic

states. As represented by the dotted lines in Fig. 5.8, the excess vibrational energy is lost in a rapid relaxation processes. In more complicated molecules with many degrees of freedom, the vibrational motion is described in terms of the normal modes of the coupled system. These vibrational modes are usually represented by a generalized coordinate Q , which has the dimension of a length. The Born-Oppenheimer approximation allows us to produce configuration diagrams in which we plot the electronic energy as a function of Q . Fig. 5.9 is an example of such a configuration diagram. In general, the ground state and the excited state have approximately parabolic minima at different values of the configuration coordinate. The absorption and emission spectra consist of a series of lines with frequencies given by Eq. 5.28 and Eq. 5.30. The relative intensities of the manifold of vibronic transitions can be calculated in the Franck-Condon approximation. The transition probability (Eq. 5.7) for an electric-dipole transition from an initial state Ψ_1 to a final state Ψ_2 is proportional to the square of M_{12} by Eq. 5.8:

$$M_{12} = \int \Psi_2^* (-i\hbar \nabla) \Psi_1 d\mathbf{r} dQ. \quad (5.31)$$

For the coupled vibrational-electronic states that we are considering here, the total wave function will be a product of an electronic wave function that depends only on the electron coordinate \mathbf{r} , and a vibrational wave function that depends only on the configuration

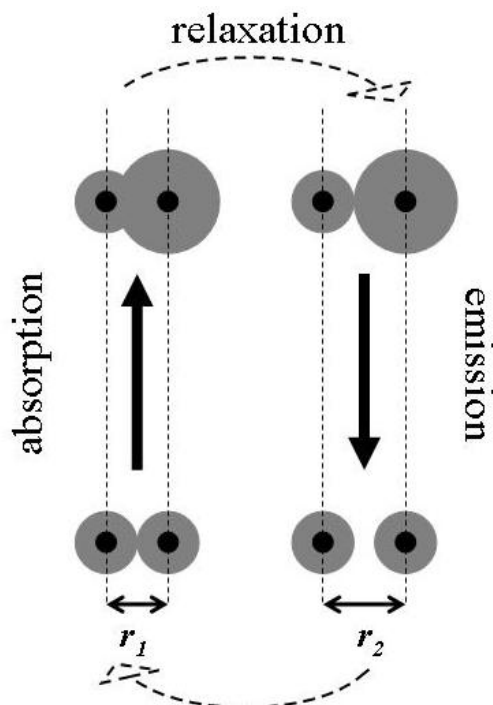


Figure 5.7: Schematic representation of the processes that occur during the absorption and emission of photons by vibronic transitions in a molecule.

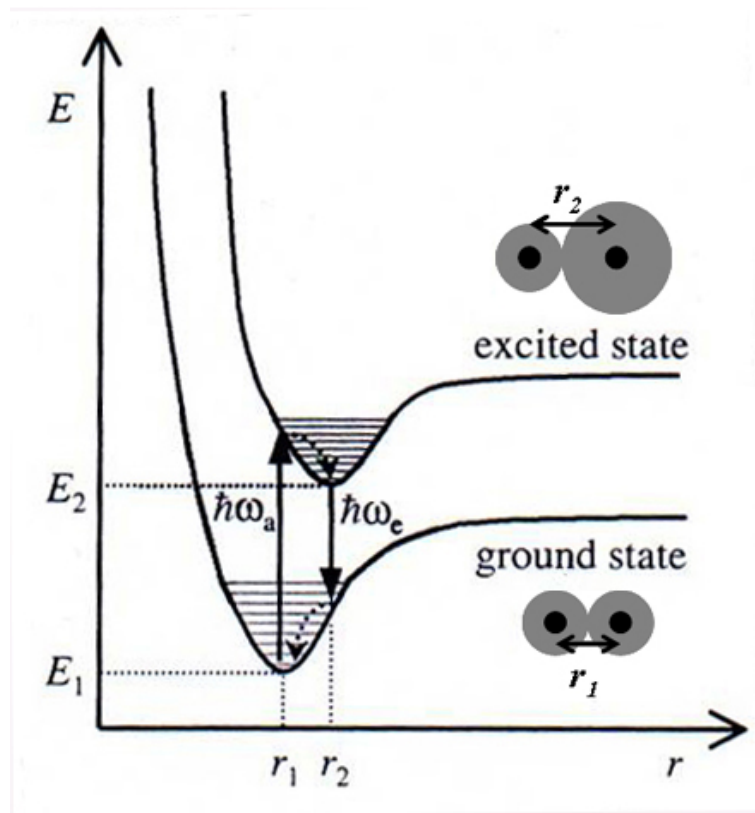


Figure 5.8: Energy level diagram for the ground state and an excited state of a simple diatomic molecule, as a function of the separation between the two nuclei.

coordinate Q . We thus write the vibronic wave function for an electronic state i and a vibrational level n as:

$$\Psi_{i,n}(\mathbf{r}, Q) = \psi_i(\mathbf{r})\varphi_n(Q - Q_0). \quad (5.32)$$

The vibrational wave function $\varphi_n(Q - Q_0)$ is just the wave function of a simple harmonic oscillator centered at Q_0 , the equilibrium configuration for the i th electronic state. By inserting Eq. 5.32 into Eq. 5.31, M_{12} can be separated into two parts:

$$M_{12} \propto \int \psi_2^*(\mathbf{r})\nabla\psi_1(\mathbf{r})d\mathbf{r} \times \int \varphi_{n_2}^*(Q - Q'_0)\varphi_{n_1}(Q - Q_0)dQ. \quad (5.33)$$

In this equation, the first factor which is due to the electronic-dipole moment is assumed to be non-zero. The second factor represents the overlap of the initial and final vibrational wave functions. According to Fermi's golden rule, the transition rate is proportional to the square of M_{12} . Therefore, the intensity of each vibrational transition will be proportional to the *Franck-Condon factor*:

$$I_{n_1, n_2} \propto \left| \int_0^\infty \varphi_{n_2}^*(Q - Q'_0) \varphi_{n_1}(Q - Q_0) dQ \right|^2. \quad (5.34)$$

In the other words, the Franck-Condon factor indicates that the intensity of the transition is proportional to the overlap of the initial and final vibrational wave functions.

5.2.5 Electron-phonon coupling

As it has been discussed in the previous sections, electronic transitions in molecular solids are tightly coupled with the vibronic modes. Hence, a complete understanding of the optical properties requires knowledge of the details of electrons, phonons, and their interaction. The strength of this coupling can be different for different organic molecules. The calculation of the electron-phonon coupling of a series of aromatic molecules shows that electron-phonon coupling behaves inversely to the number of π bonded atoms. The result of these calculations is shown in Fig. 5.10 [59].

In this figure (Fig. 5.10), N_π is the number of atoms involved in the π states of the molecule and V_{el-ph} is a purely intramolecular quantity, describing the strength of the

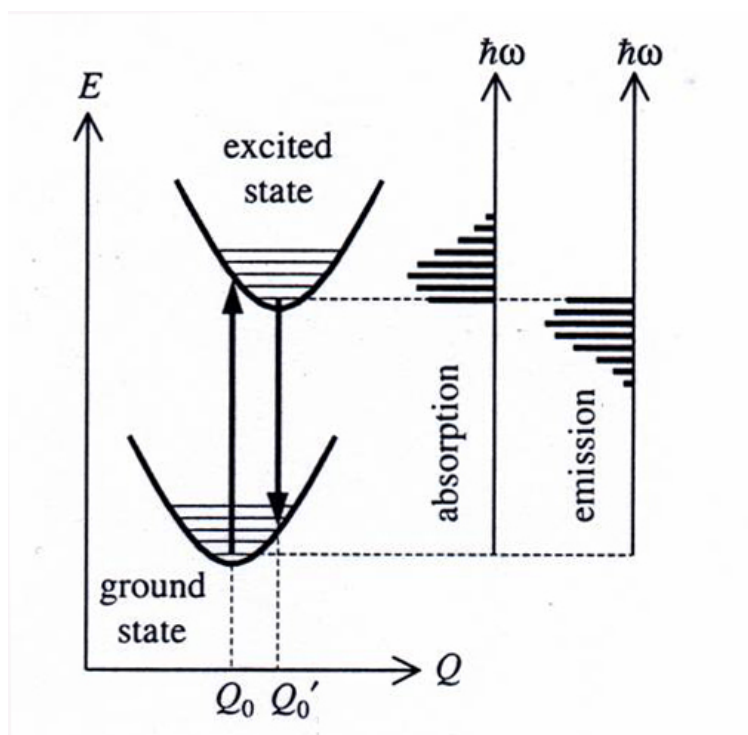


Figure 5.9: Configuration diagram for two electronic states in a molecule. Vibrational-electronic transitions are indicated by the vertical arrows, together with a schematic representation of the absorption and emission spectrum.

electron-phonon coupling as the gain in energy due to this effect. The detailed expression of V derived in ref. [59] is

$$V_{el-ph} = \sum_q \frac{1}{M\omega_q^2} \frac{1}{\nu^2} \sum_{i,j} \left(\frac{\partial M_{ij}}{\partial Q_q} \right)^2, \quad (5.35)$$

in which ν is the degeneracy of the partially filled molecular level which generates the conduction band at the Fermi level, $\partial M_{ij}/\partial Q_q$ is the electron-phonon matrix element between two of its basis states $|i\rangle$ and $|j\rangle$ for the molecular vibrational mode Q_q of frequency ω_q normalized over the whole molecule. The data presented in Fig. 5.10 have been obtained by A. Devos and M. Lannoo performing numerical calculations. For each molecule, a geometry optimization has been performed using quantum-mechanical forces at the *ab initio* level in the local-density approximation (LDA) 2.1.3. The electronic-structure calculation was then performed by two techniques. First, density-functional theory has been used within the local-density approximation (LDA). Also, the electronic

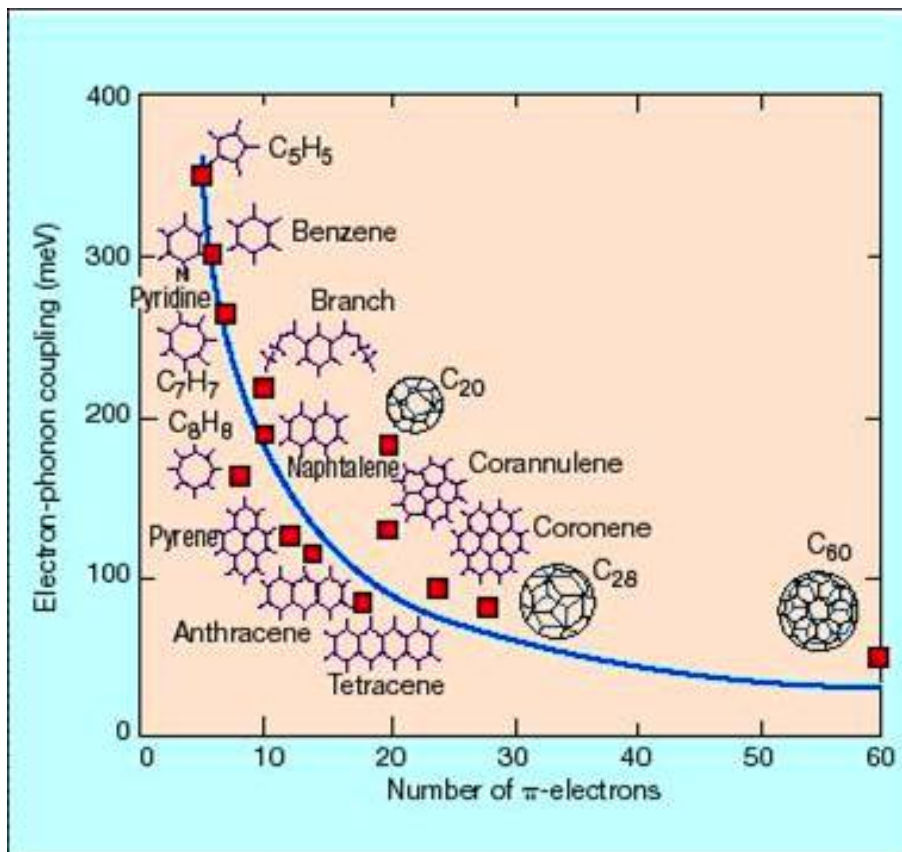


Figure 5.10: The electron-phonon coupling constant for a series of organic molecules is shown as a function of π -electrons associated with their carbon rings. Squares indicate the data obtained by numerical calculations. [59]

structure has been calculated with the nearest-neighbors empirical tight-binding method (TB).

In order to understand the trends of V_{el-ph} for the family of aromatic molecules shown in Fig. 5.10, with their number of atoms N_π involved in the π states of the molecule, the following simple argument is used. According to the Einstein approximation, ω_q^2 in Eq. 5.35 can be replaced by an average value. Then the only quantity left in Eq. 5.35 is $\sum_q (\partial M_{i,j} / \partial Q_q)^2 = \sum_\alpha (\partial M_{i,j} / \partial \mathbf{r}_\alpha)^2$ where \mathbf{r}_α are the components of the atomic displacements. In the tight-binding (TB) model, where $|i\rangle$ and $|j\rangle$ are delocalized over the N_π atomic π states, each individual term $(\partial M_{i,j} / \partial Q_{\mathbf{r}_\alpha})^2$ is of order of $1/N_\pi^2$ and their sum is then of order $1/N_\pi$. This proves that, at least in an average way $V(N_\pi) \propto 1/N_\pi$. This basic behavior has been confirmed analytically, as well, for a simple model of C_nH_n molecules. [59].

5.3 Exciton effect

In the previous section, the absorption of photons by inter-/intra-band transitions has been discussed. This process creates an electron in the conduction/LUMO band and a hole in valence/HOMO band. But the effect of the Coulomb interaction between these pairs has been neglected. In this section, it will be shown that the Coulomb interaction can give rise to the formation of new excitations of the solid, called "excitons". These excitons have interesting optical properties and are important for optoelectronic applications. The optical spectra of organic solids are strongly affected by excitonic effects. Excitonic effects are present in molecular materials because the unpaired electron left in the ground state by an optical transition can be regarded as hole state. This hole acts like a positive charge because it represents the absence of a negative electron. The Coulomb interaction between the electrons and holes has a strong effect on the optical spectra.

5.3.1 The concept of excitons

In materials such as semiconductors, insulators or molecular materials, the absorption of a photon by an interband transition creates an electron in the conduction band and a hole in the valence band. The attractive Coulomb interaction between these two oppositely charged particles increases the probability of the formation of an electron-hole pair. This, in turn, increases the optical transition rate. Moreover, if the right conditions are satisfied, a bound electron-hole pair can be formed. This neutral bound pair is called an exciton. In the simplest picture, the exciton may be conceived as a small hydrogenic system similar to a positronium atom with the electron and hole in a stable orbit around each other. There are two basic types of Excitons, observed in different solids 5.11:

1. *Wannier-Mott excitons*, which are also named as *free excitons* and are mainly observed in inorganic semiconductors.

2. *Frenkel excitons*, which are also called *tightly bound excitons* and are found in insulators and molecular solids.

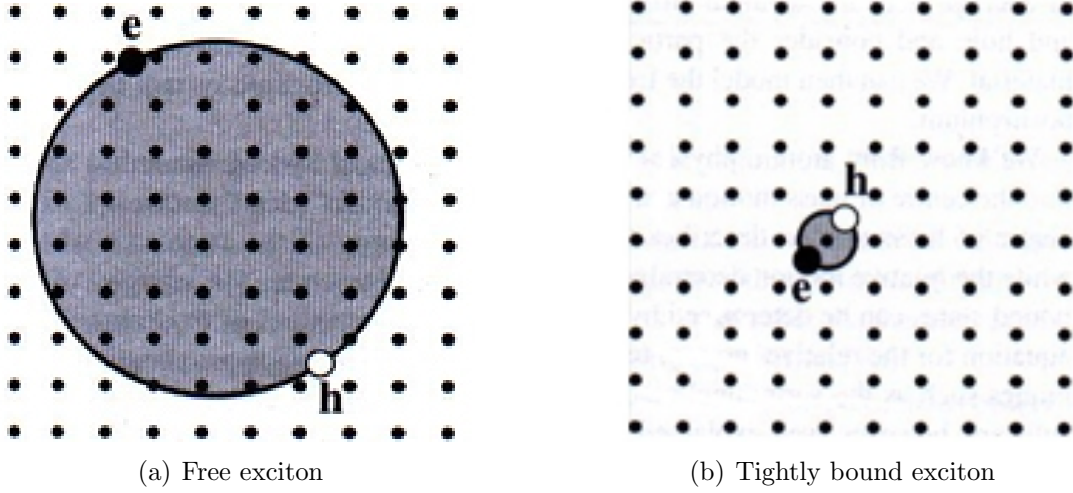


Figure 5.11: Schematic diagram of: (a) a free exciton, and (b) a tightly bound exciton. [8]

5.3.2 Free excitons

The Wannier-Mott type excitons are illustrated schematically in Fig. 5.11(a). The diagram shows an electron and hole orbiting around each other within a crystal. This type of exciton has a large radius that encompasses many atoms. These excitons are delocalized states that can move freely throughout the crystal which are also called 'free' excitons. In a free exciton, the average separation of the electrons and holes is much greater than the atomic spacing. This means that the free exciton is a weakly bound electron-hole pair. Since, the electron-hole separation is so large, it is a good approximation to average over the detailed structure of the atom in between the electron and hole and consider the particles to be moving in a uniform dielectric material. We can then model the free exciton as a hydrogenic system similar to positronium. So, the Bohr model can be applied to the exciton, by taking into account the fact that the electron and hole are moving through a medium with a high dielectric constant ϵ_r . The bound states are characterized by the principal quantum number n . The energy of the n th level relative to the ionization limit is given by

$$E(n) = -\frac{\mu}{m_0} \frac{1}{\epsilon_r^2} \frac{R_H}{n^2} = -\frac{R_X}{n^2}, \quad (5.36)$$

where μ is the reduced mass, R_H is the Rydberg constant of the hydrogen atom (13.6 eV). The quantity $R_X = (\mu/m_0\epsilon_r^2)R_H$ introduced here is the exciton Rydberg constant. The radius of the electron-hole orbit is given by

$$r_n = \frac{m_0}{\mu} \epsilon_r n^2 a_H = n^2 a_X. \quad (5.37)$$

In Eq. 5.37, a_H indicates the Bohr radius of the hydrogen atom ($5.29 \times 10^{-11}m$) and $a_X = (m_0 \epsilon_r / \mu) a_H$ is the exciton Bohr radius. Equation 5.36 and Eq. 5.37 show that for the states with greater quantum number, n , binding energy is less and exciton-radius is larger. Free excitons are typically observed in direct gap semiconductors. These type of excitons are created during direct band-to-band optical transitions between the valence and conduction bands. As discussed in Section 5.2.1 this creates an electron-hole pair in which the electron and hole have the same \mathbf{k} vector. Excitons can only be formed if the electron and hole group velocities v_e and v_h are the same. This is a necessary condition for the electrons and holes to be able to move together as a bound pair. The group velocity of an electron in a band is given by

$$v_g = \frac{1}{\hbar} \frac{\partial E}{\partial \mathbf{k}}. \quad (5.38)$$

The condition $v_e = v_h$ can only be satisfied if the gradients of the conduction and valence bands are the same at the point of the Brillouin zone where the transition take place. Therefore, excitons can be formed during a direct transition at $\mathbf{k} = 0$, since all bands have zero gradient at the zone center. In a direct gap semiconductor these transitions correspond to a photon energies of E_g . Hence, we expect to observe strong excitonic effects in the spectral region close to the fundamental band gap. The energy of the exciton created in a direct transition at $k = 0$ is equal to the energy required to create the electron-hole pair, less the binding energy due to the Coulomb interaction. Therefore, the energy of the exciton could be written by:

$$E_n = E_g - \frac{R_X}{n^2}. \quad (5.39)$$

At the photon energy equal to E_n , excitons can be formed. Since, it is energetically favorable for the exciton states to be formed compared to free electron-hole pairs, the probability of the exciton formation is expected to be high. Therefore, strong optical absorption lines are expected to be observed at energies equal to E_n . This effect is represented schematically in Fig. 5.12, which shows the band edge absorption spectra for a direct gap semiconductor with excitonic effects included. The absorption appears at energies just below the fundamental band gap.

5.3.3 Frenkel tightly bound excitons

Frenkel type excitons, as shown in Fig. 5.11, have a small electron-hole radius which is comparable to the interatomic spacing. This makes them localized states which are

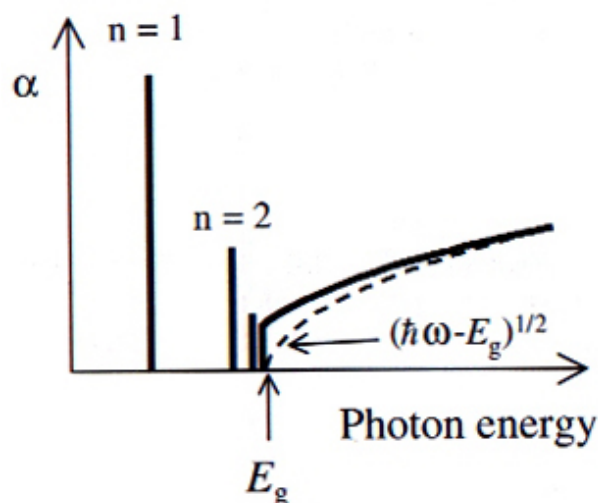


Figure 5.12: Excitonic effect in band edge absorption spectra for a direct gap semiconductor. The dashed line represents the expected absorption when the excitonic effects are ignored. [8]

tightly bound to specific atoms or molecules; hence their alternative name of 'tightly bound' excitons. Tightly bound excitons are much less mobile than free excitons, and they have to move through the crystal by hopping from one atom site to another.

Stable excitons will only be formed if the attractive potential is sufficient to protect the exciton against collisions with phonons. Frenkel excitons are localized on the atom site at which they are created. The excitons may therefore be considered as excited states of the individual atoms or molecules on which they are localized. They have very small radii and correspondingly large binding energies, with values ranging from about 0.1 eV to several eV. Since the maximum energy of a thermally excited phonon at temperature T is $\sim k_B T$, where k_B is Boltzmann's constant, this condition will be satisfied if the exciton binding energy is greater than $k_B T$. Since, $k_B T \sim 0.025$ eV at room temperature, this means that Frenkel excitons are usually stable at room temperature. The excitons can propagate through the solid by hopping from atom site to site in the same way that spin excitations propagate through crystals as magnon waves. These type of excitons can be observed in large band gap materials with small dielectric constants and large effective masses. In these materials, the free exciton model that leads to Eq. 5.36 and Eq. 5.37 breaks down, since the predicted radius becomes comparable to the interatomic spacing. This type of excitons are found in insulator crystals and molecular solids. The theoretical treatment of Frenkel excitons requires techniques more akin to atomic or molecular physics than solid state physics. There is no simple model similar to the one that led to Eq. 5.36 and Eq. 5.37 for free excitons. The calculation of the exciton energies usually follows a tight binding approach, in order to emphasize the correspondence to the atomic or molecular states from which the excitons are derived. The calculation is further complicated by the fact that coupling between the excitons and the crystal lattice is usually very strong. This

leads to 'self-trapping' effects, in which the exciton produces a local distortion of lattice, which then causes further localization of the exciton wave functions.

5.3.4 Molecular crystals and organic thin films

Frenkel excitons have been observed in many inorganic and organic materials. Here, the properties of molecular crystals and organic film structures will be described. In most cases, there is a very strong correspondence between the optical transitions of the isolated molecules and the excitons observed in the solid state. This is a consequence of the fact that the molecular solids are held together by relatively weak van der Waals forces, so that the molecular levels are only weakly perturbed when condensing to the solid state.

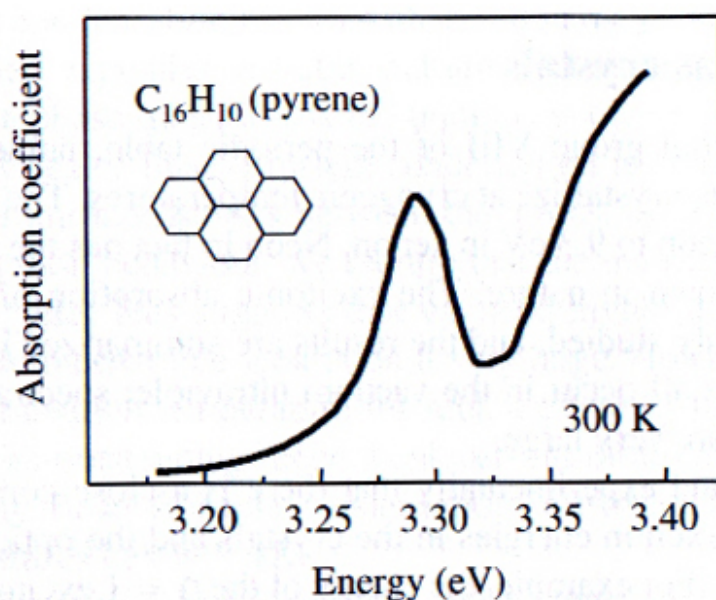


Figure 5.13: Absorption spectrum of pyrene $C_{16}H_{10}$ single crystals at room temperature. [60]

Fig. 5.13 shows the fundamental absorption edge of pyrene crystals at room temperature. The pyrene molecule has a composition of $C_{16}H_{10}$ and is an example of an aromatic hydrocarbon, that is, a carbon-hydrogen compound based on benzene rings. The 4-ring structure of pyrene is given in the inset. The absorption spectrum shows a clear excitonic peak at 3.29 eV. Other aromatic hydrocarbons such as anthracene ($C_{14}H_{10}$) also show very strong excitonic effects, but the optical spectra are more complicated because of the strong coupling to the vibrational modes of the molecule. The pyrene spectrum is relatively simple because the 4-ring structure makes the molecule very rigid and reduces the effects of the vibrational coupling.

Furthermore, Frenkel excitons are very important in conjugated polymers, such as polydiacetylene (PDA) and also small molecules such as Perylene. Single crystals of PDA can

be grown, but the optical properties are often studied by using amorphous films coated onto glass substrates. The strong excitonic effects in conjugated polymers have acquired considerable technological significance in recent years, following the development of organic light emitting diodes for use in display technology. The optical properties of organic semiconductors such as PDA will be discussed in more detail in the following section.

5.4 Optical response of conjugated polymers

In this section, we present more details about the structure and optoelectronic properties of conjugated polymers. Polymers are long-chain molecules which are composed of repeated sequences of monomer unit. Hence, the name *polymer* is the logical progression of the sequence starting from the *monomer* (single molecule), then to the *dimer* (double molecule), and on to *polymer* (many molecules). The monomer units are based on carbon-carbon bonds. The progression which leads to polymer formation is illustrated for ethylene (C_2H_4) in Fig. 5.14. The dimer [C_2H_4], which is cyclobutane (C_4H_8). The polymer is polyethylene, or polythene for short, with a formula of $[CH_2]_n$, where n is a large number.

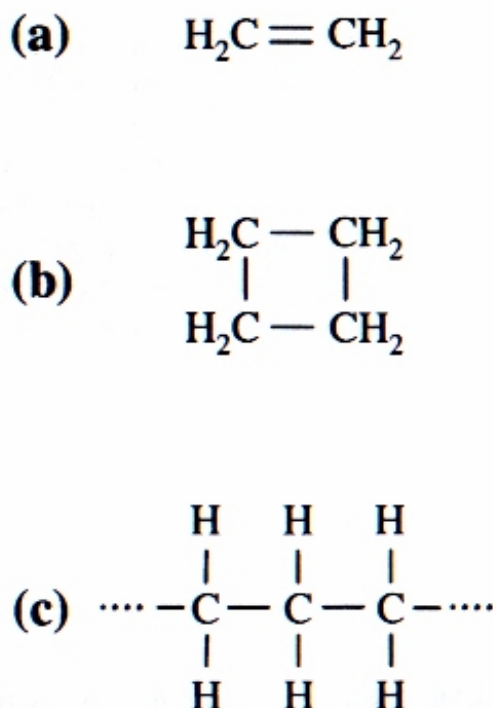


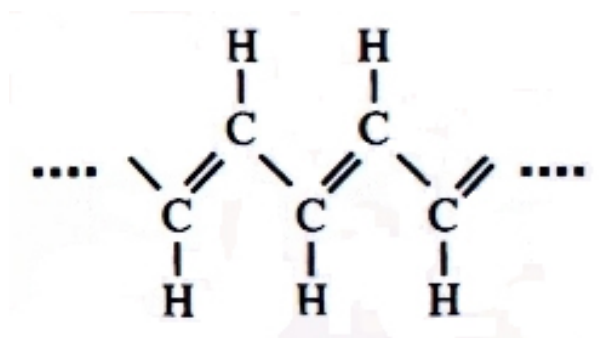
Figure 5.14: An example of monomer, dimer and polymer. (a) Ethylene (C_2H_4) monomer. (b) Ethylene dimer ($[C_2H_4]_2$). (c) Poly-ethylene ($[C_2H_4]_n$).

Polymers such as polythene are called saturated, since all the electrons are incorporated into σ bonds, and are therefore very tightly bound. Optical transitions of this type of polymers are at high energies in the ultraviolet region, and are not of particular interest here. Therefore, in this session we will focus more on conjugated polymers with alternating single-double bounds along the chain.

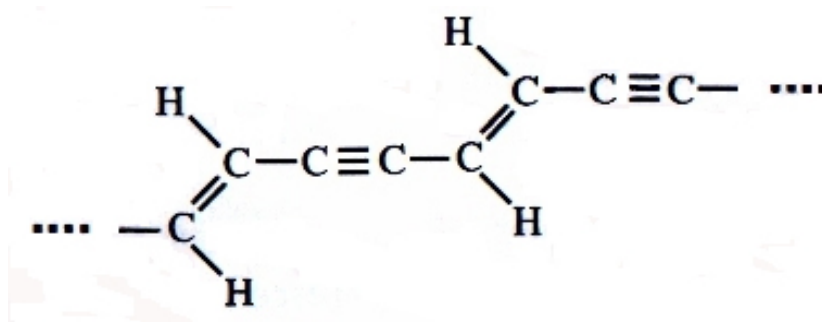
The chemical structure of two conjugated polymers are shown in Fig. 5.15. Polyacetylene, the simplest conjugated polymer, is shown in Fig. 5.15(a). This polymer is formed by combining many acetylene molecules (C_2H_2 , bonding $HC \equiv CH$) into a long chain with alternating single and double bonds between the carbon atoms:



It should be noted that, the depiction of alternating single and double bonds for the conjugated polymers in this figure is , obviously, schematic. In reality, the spare electron of the double bond is shared equally between both bonds in a delocalized Π orbital.



(a) Polyacetylene



(b) Polydiacetylene (PDA)

Figure 5.15: Chemical structure of two conjugated molecules.

Polydiacetylene (PDA) is a slightly more complicated conjugated polymer, demonstrated in Fig. 5.15(b), which incorporates both double and triple bond Π electrons. PDA is one of the most widely studied conjugated polymers because it is able to form high quality

crystals at room temperature. The $\Pi \rightarrow \Pi^*$ transitions occur in the visible spectral region for many of these conjugated polymers.

Fig. 5.16 shows both the absorption and photocurrent spectrum of polydiacetylene (PDA) single crystals. The absorption spectrum shows a broad $S_0 \rightarrow S_1$ absorption band starting at 1.8 eV. The band shows a clear substructure, with two well-resolved vibronic peaks at 1.9 eV and 2.1 eV. The peaks around 3.6 eV are caused by $S_0 \rightarrow S_2$ transitions.

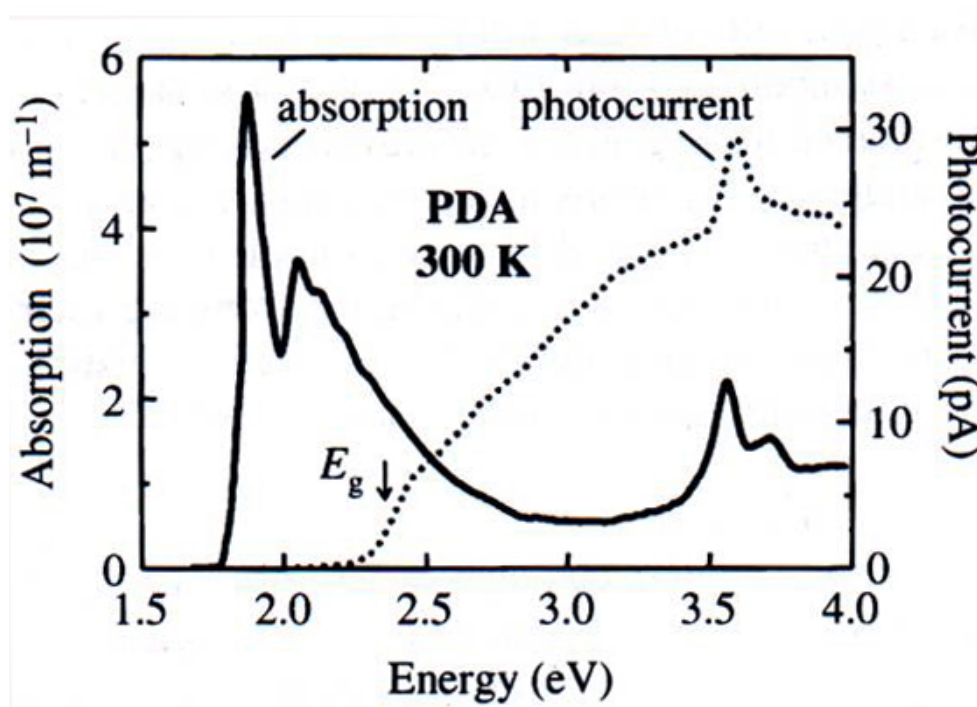


Figure 5.16: Absorption spectrum of polydiacetylene (PDA) crystals at room temperature. The photocurrent spectrum of the same crystal is shown for comparison. [61]

The optical spectra of conjugated polymers like PDA are strongly affected by excitonic effects. As it have been already mentioned in section (5.3), these excitons are tightly bound, Frenkel, type. The excitonic effects create bound states below the band edge and enhance the probability for radiative transitions. The binding energy of the excitons in PDA can be determined by comparing the absorption and photocurrent spectra of the same crystal. As shown in Fig. 5.16, the photocurrent spectra has a threshold at 2.4 eV, which is about 0.5 eV above the absorption edge. This is a clear indication that the absorption line at 1.9 eV is excitonic in character. The creation of the neutral tightly bond excitons does not affect the conductivity, and the photon energy must exceed the HOMO-LUMO band gap at 2.4 eV before free electrons and holes are available to produce a photocurrent. The measurement therefore indicates that the binding energy of the exciton is 0.5 eV.

6 Scientific instruments

This chapter is a review on different scientific instruments which have been used throughout this work. The purpose of this review is to give a simple but brief overview. For more detailed information, the reader may be referred to the extensive literature available for each instrument. The description is not product-related, and also not related to the purpose for which an individual instrument is used in this work. This is described in detail in the "Experimental methods" sections in the subsequent chapters.

6.1 Organic vapor phase deposition (OVPD)

Organic Vapor Phase Deposition (OVPD) was invented by S. Forrest at Princeton University to transfer all the benefits of the gas phase process in the organic electronics applications. [62] [63] The OVPD technology is well suited for thin film deposition of organic materials on large-area substrates. In this process, the organic compound is thermally evaporated and transferred by an inert gas within a hot-walled reactor toward a cooled substrate where condensation occurs.

As shown in Fig. 6.1 the evaporation of the organic material occurs in individual and decoupled quartz pipes. [64] By using the standard Mass Flow Controllers (MFC) a precise amount of carrier gas, for example nitrogen, is added into each quartz pipe to carry the organic molecules. The organic molecules are transported by the carrier gas into the hot wall deposition chamber and are uniformly mixed, in the case that more than one organic material is evaporated simultaneously. Finally the organic molecules in the gas phase diffuse through the boundary layer and are deposited onto the cooled substrate where condensation occurs. One of the advantages of this controlled gas phase transport technique is that no unintended deposition of expensive organic molecules occurs in the hot wall OVPD chamber. Using a carrier gas in OVPD enables the deposition of organic materials in a controlled pressure regime of $10^{-3} - 10^1$ Torr. Thus the OVPD chamber has not to be pumped down to high vacuum conditions like VTE (Vapor Thermal Evaporation).

Compared to vacuum and spin deposition techniques, OVPD gains an extra degree of freedom by using carrier gases to transport source materials to a substrate. Near the sublimation point, the vapor pressure of the organic material varies rapidly with temperature. This makes it difficult to have the accurate control of transport rates by varying

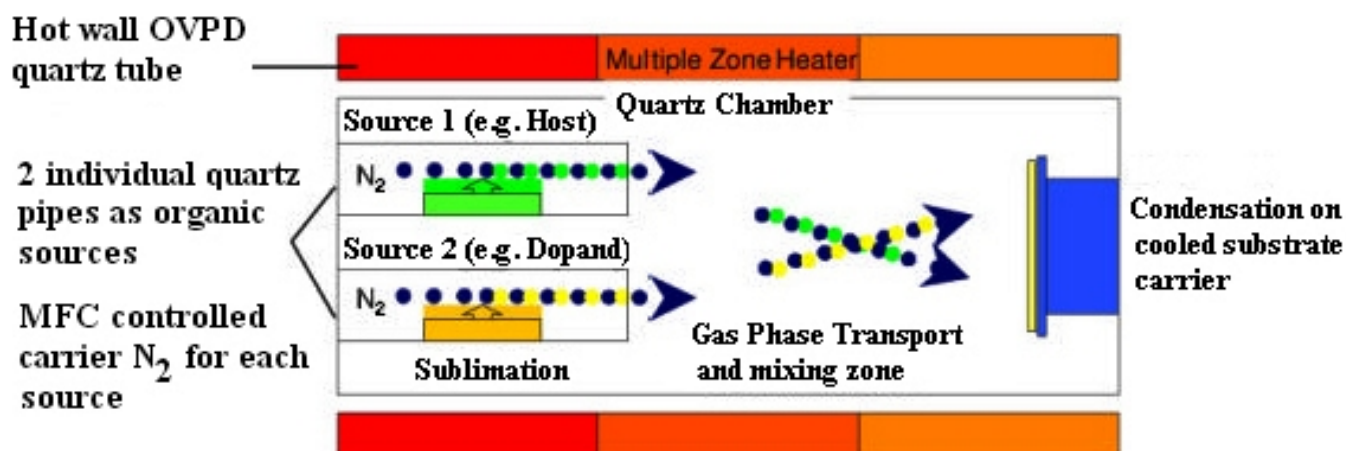


Figure 6.1: OVPD® principle and quartz flow deposition module invented by Forrest. [64]

the source temperature. However, if source temperatures are controlled to within a few degrees, the relative concentrations of organic constituents in the gas stream can be accurately varied by adjusting the carrier gas flow rates. Thus, amongst its other features, OVPD is suited to the fabrication of organic light-emitting devices (OLEDs) and lasers consisting of low concentrations of dopant molecules incorporated into a host matrix. [62] Significantly, OVPD and related techniques [65] are also capable of crystalline growth and generating thin films of stoichiometric organic salts, [66], [67] enabling the exploitation of this wide family of organic materials.

There are two regimes of vapor phase growth. [68] The mass transport limit occurs when the growth rate is determined by the arrival rate of the source materials at the substrate. Due to viscous flow effects, slower moving gas forms a boundary layer close to the substrate through which the source materials must diffuse, as shown in Figure 6.2. In this case, the growth rate is dependent not only upon the concentration of source material, but also upon the shape and depth of the boundary layer. This can often lead to non-uniform film growth. In contrast, in the kinetic limit, the growth rate is determined by the rate at which reactions occur, ultimately reducing the influence of non-uniform boundary layers.

At lower pressures, the diffusion rate of source materials is increased, and growth is more likely to be kinetically rather than mass-transport limited. Thus, lower reactor pressures are commonly used in organometallic vapor phase epitaxy (OMVPE) of semiconductors to improve film uniformity. [68] In addition, lower pressure reduces nucleation of source materials in the gas phase as the number of intermolecular collisions is decreased. Gas flow rates also increase, reducing residence times by minimizing turbulent flow, and eliminating vortices and thermal non-uniformities. For large area depositions, this is particularly

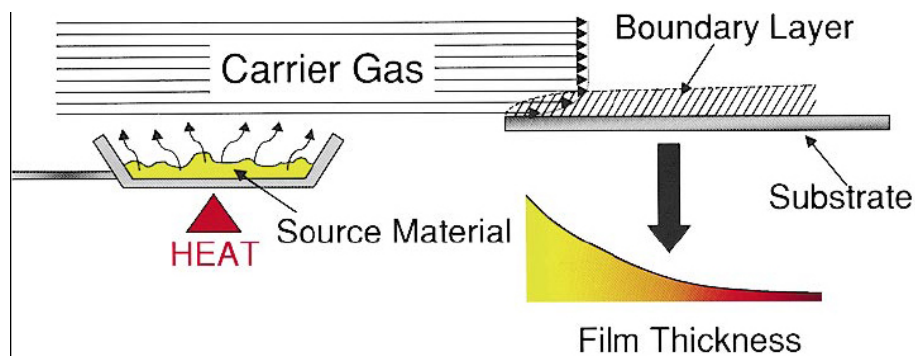


Figure 6.2: Schematic representation of the boundary layer in an LP-OVPD system with a horizontal substrate (from [68])

important because small nonuniformities in growth rates are magnified as the system scale is increased. Hence, it is likely that large vapor deposition chambers will operate at reduced pressures. In our laboratory, therefore, vapor deposition of organic materials is typically performed below atmospheric pressure (9-10 torr) using the modified process of low pressure organic vapor phase deposition (LP-OVPD). [69] Where high growth rates are desired, for example in the deposition of amorphous films used in OLEDs, growth is typically mass-transport limited. This is the result of substrate cooling, which eliminates substrate kinetics by increasing the adhesion of source materials, and correspondingly maximizes growth rates. Consequently, growth rates are principally determined by the diffusion rates across the boundary layer. Thus, even in a laminar flow, low pressure reactor, diffusion-limited growth implies that thickness nonuniformities will accompany high growth rates unless gas dynamics and boundary layer shape are well understood and controlled.¹

6.2 Atomic force microscopy (AFM)

Atomic force microscopy (AFM) can be used for the characterisation and imaging of surfaces in the atomic range but also for the manipulation of matter on the nanoscale. The principle of the AFM is based on the interaction of a fine tip with the sample surface. The tip radii can be as small as one atom and larger than $1\ \mu\text{m}$ [70]. Of most current interest are the smaller tips, where in principle one could directly measure the force between an individual atom and a surface. This adhesion force, which would be necessary to separate the tip and the surface from contact, is in the order of only 10^{-9} to 10^{-10}N . To measure such forces the AFM technology has been developed, using highly sensitive micron-sized force-sensing devices. A variety of laser-optical techniques is also required

¹Sample preparation has been done by AIXTRON AG, Aachen, Germany.

for detecting such small changes in the interaction forces. The obtained sensitivity is then sufficient for measuring adhesion and very short-range forces between molecular-sized tips and surfaces, but not longer range forces.

The principle of the AFM is presented in Fig. 6.3. The tip is moved over the sample surface in a raster scan, similarly to the principle of a Scanning tunnelling microscope (STM). On the contrary to an STM, which requires conducting surfaces, the AFM can also be applied for materials that are not conducting, because the tip and the surface interact via Van-der-Waals forces.

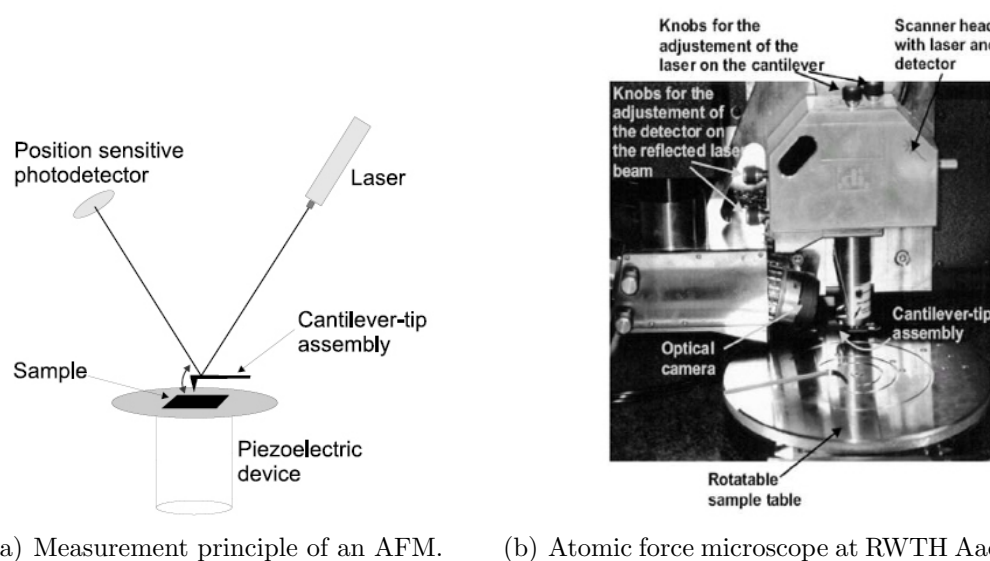


Figure 6.3: Atomic force microscope

Two piezoelectric scanners are used to scan the cantilever in lateral (x and y) direction over the sample (Fig. 6.3). A very fine tip is located underneath the cantilever to scan the topography. A laser is reflected at the back side of the cantilever towards a position-sensitive split photodiode detector that measures the deflection of the cantilever, which is related to the topography. A feedback loop controls a third piezoelectric scanner to re-adjust the height of the cantilever (z coordinate). Two operational modes are most frequently used:

- **Contact mode (constant force mode):** The tip is in continuous contact with the sample surface during scanning. The feedback loop maintains a constant cantilever deflection ('setpoint') and therefore a constant force on the sample. For instance, a hillock on the surface would induce a larger force and therefore a stronger deflection. The feedback loop however counteracts by lifting the scanner by the height of the hillock. Similarly, the feedback loop lowers the scanner by a distance equal to the depth of a depression. Hence, the movement of the scanner exactly reproduces the surface topography. Silicon nitride cantilevers are usually used for contact mode.

- **Tapping mode (constant amplitude mode):** The cantilever is oscillated vertically (normal to the sample surface) by an external periodic force at or near its resonance frequency of about 300 kHz. The oscillation amplitude typically ranges between 20 and 100 nm. The tip 'taps' on the sample surface at each oscillation minimum, which leads to a damping of its oscillation amplitude. The feedback loop maintains this amplitude ('setpoint') at a constant level and therefore, the movement of the scanner reproduces the surface topography as in contact mode: If a *hillock* occurs, the scanner *lifts* the cantilever to prevent an amplitude decrease due to an *increased* damping. On the other hand, if a *depression* occurs, the scanner *lowers* the cantilever to prevent an amplitude *increase* due to a *decreased* damping. For tapping mode, the cantilever and the tip are usually an integrated assembly of single crystal silicon.

The advantage of contact mode is that it can yield atomic resolution. Moreover, mechanical properties of the sample can be measured. However, the disadvantage of this mode is that the tip can damage (scrape) soft samples easily. Hence, contact mode is usually only used for hard samples.

Tapping mode can be used for softer samples because it applies marginal (usually non-damaging) forces to the sample, still at a good resolution.

6.3 X-ray-reflectometry (XRR)

X-rays are sensitive to the changes of the electron density of solid structures. Their wavelength is in the range of 0.1 pm to 10 nm and is therefore comparable to the distances separating atoms in crystals. The interaction between x-rays and matter can be traced back to three different processes, which take place in the electron sheath of the atoms [71]:

- The atom is transferred into an excited state, when the x-ray radiation has enough energy to remove one electron from the inner shell. When the electron returns to a state with a lower energy, a characteristic x-ray radiation is emitted.
- Incoherent scattering occurs, when during an impact between an x-ray quant and an electron the energy of both impact partners is changed. The incoherent radiation thereby has a longer wavelength than the original x-ray radiation.
- The electrons can also start to oscillate, when they are excited by incoming x-rays. Thus, they send out radiation with the same wavelength as the incoming x-rays and coherent scattering occurs.

X-ray-reflectometry (XRR) is a non-destructive technique for thickness determination between 2-200 nm with a precision of about 1-3 Å. In addition to thickness determination,

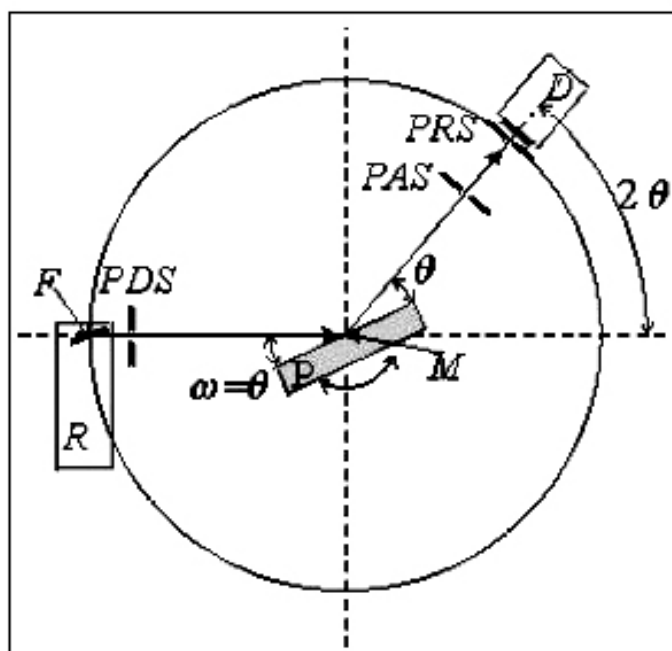


Figure 6.4: $\theta/2\theta$ -Scan: The condition of incident angle $\omega = 2\theta/2 = \theta =$ outgoing angle is satisfied. The detector D rotates at twice the speed around the sample P . This arrangement is sensitive only to the planes parallel to the surface of the sample. The beam makes an incident angle ω with the surface of the sample P . The reflected intensity at angle of 2θ is measured. Both the rotation of the sample ω and the detector (2θ) are about the same axis MP (perpendicular to the drawing). The sample is adjusted so that the rotation axis lies on the sample surface. The Detector circle is fixed through the (programmable) detector slit (PRS , programmable receiving slit). The anode focus, F of the tube lies on the detector circle.

this technique is also employed for the determination of density and roughness of the films and multilayers with a high precision.

XRR method involves monitoring the intensity of the x-ray beam reflected by a sample at grazing angles. A monochromatic x-ray beam of wavelength λ irradiates a sample at a grazing angle ω and the reflected intensity at an angle 2θ is recorded by a detector, see Fig. 6.4 This figure illustrates specular reflection where the condition $\omega = 2\theta/2$ is satisfied. The mode of operation is therefore a $\theta/2\theta$ mode which makes sure that the incident angle is always half of the angle of diffraction. The reflection at the surface and interfaces is due to the different electron densities in the different layers (films), which corresponds to different refractive indexes in classical optics. For incident angles θ below a critical angle θ_c , total external reflection occurs. The critical angle for most materials is less than 0.3° . The density of the material is determined from the critical angle. Above θ_c the reflection from the different interfaces interfere and give rise to interference fringes. Fig. 6.5 The period of the interference fringes and the fall in the intensity are related to

the thickness and the roughness of the layer (layers in case of multilayers). The reflection can be analyzed using the classical theory, i.e. the Fresnel equations. The typical range for these measurements are between 0° and 5° in θ . [71]

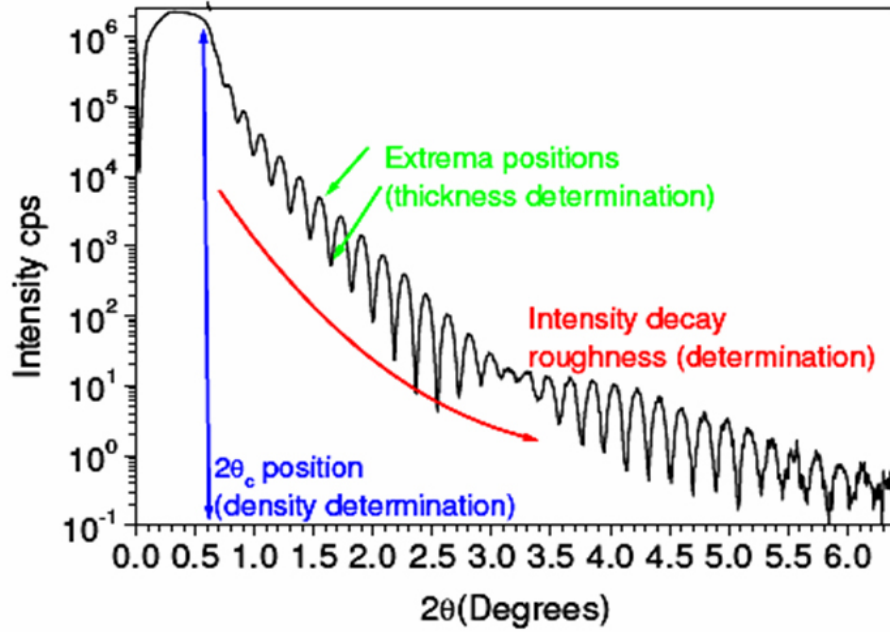


Figure 6.5: An example of XRR spectrum. The period of the interference fringes and the fall in the intensity are related to the thickness and the roughness of the layer. The total reflection edge is related to the film density.

In Fig. 6.5, the oscillations stem from the interference of beams reflected at the air/film and at the film/substrate interface. The refractive index, n , of all materials (except air) in the x-ray region is slightly less than 1, $n = 1 - d$. Hence, a sudden decrease of the intensity in the XRR spectrum is observed at the total reflection edge. By applying Snell's law and the small angle approximation, the critical angle, θ_c , can be related to the film density as follows

$$\theta_c = \sqrt{\frac{r_0 \lambda^2}{\pi} N_A \frac{z + f'}{A} \rho}. \quad (6.1)$$

As can be seen from Eq. 6.1, the critical angle increases with the density of the film.²

²AFM and XRR measurements have been performed by P. Niyamakom and M. Beigmohamadi, respectively.

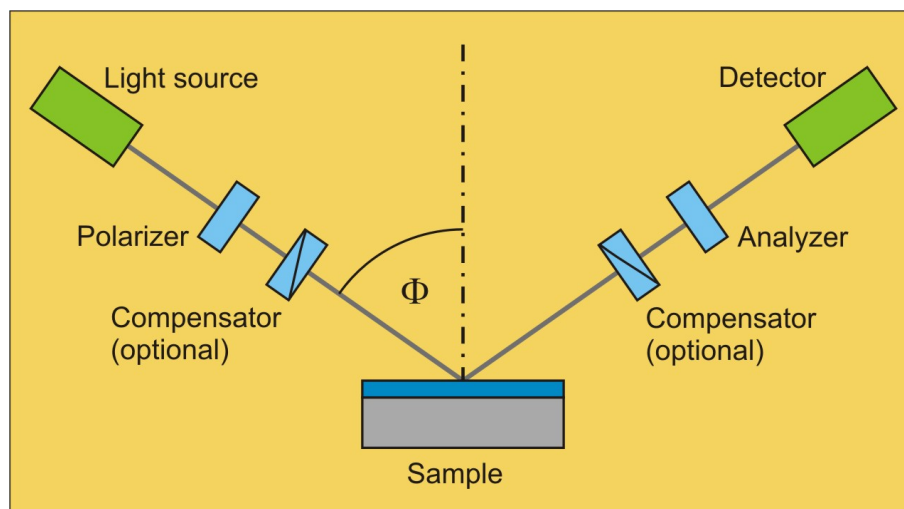


Figure 6.6: Schematic setup of an ellipsometry experiment.

6.4 Spectroscopic Ellipsometry (SE)

Spectroscopic ellipsometry (SE) is a versatile and powerful optical technique for the investigation of the dielectric properties (complex refractive index or dielectric function) of thin films. It has applications in many different fields, from semiconductor physics to microelectronics and biology, from basic research to industrial applications. Ellipsometry is a very sensitive measurement technique and provides unequalled capabilities for thin film metrology. As an optical technique, spectroscopic ellipsometry is non-destructive and contactless.

Upon the analysis of the change of polarization of light, which is reflected off a sample, ellipsometry can yield information about layers that are thinner than the wavelength of the probing light itself, even down to a single atomic layer. Ellipsometry can probe the complex refractive index or dielectric function tensor, which gives access to fundamental physical parameters and is related to a variety of sample properties, including morphology, crystal quality, chemical composition, or electrical conductivity. It is commonly used to characterize film thickness for single layers or complex multilayer stacks ranging from a few angstroms or tenths of a nanometer to several micrometers with an excellent accuracy.

The name "ellipsometry" stems from the fact that the most general state of polarization is elliptic. SE measures the change of polarization upon reflection or transmission. Typically, ellipsometry is done only in the reflection setup. The exact nature of the polarization change is determined by the sample's properties (thickness, complex refractive index or dielectric function tensor). Although optical techniques are inherently diffraction limited, ellipsometry exploits phase information and the polarization state of light, and can achieve angstrom resolution. In its simplest form, the technique is applicable to thin films with thickness less than a nanometer to several micrometers.

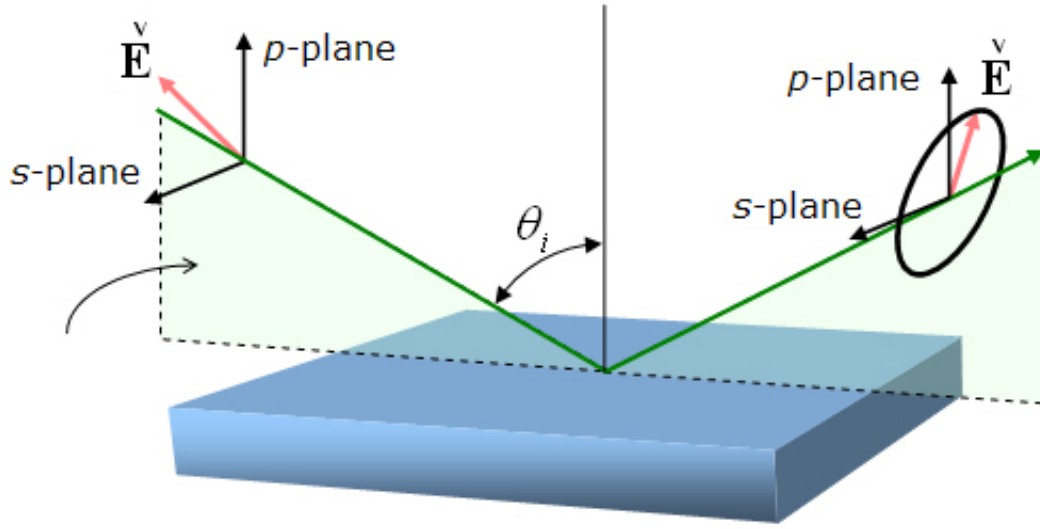


Figure 6.7: Rotation of the polarization ellipsis upon reflection on a surface.

Figure 6.6 shows a schematic view of an ellipsometry setup. Electromagnetic radiation is emitted by a light source and linearly polarized by a polarizer, it can pass an optional compensator (retarder, quarter wave plate), and falls onto the sample. After reflection the radiation passes a compensator (optional) and a second polarizer, which is called analyzer, and falls onto the detector. Instead of the compensators some ellipsometers use a phase-modulator in the path of the incident light beam. Ellipsometry is a specular optical technique (the angle of incidence equals the angle of reflection). The incident and the reflected beam span the plane of incidence. Light, which is polarized parallel or perpendicular to the plane of incidence, is called *p* or *s* polarized, respectively.

(Standard) Ellipsometry measures two of the four Stokes parameters, which are conventionally denoted by ψ and Δ . The polarization state of the light incident upon the sample may be decomposed into an *s* and a *p* component. The *s* component is oscillating perpendicular to the plane of incidence and parallel to the sample surface, and the *p* component is oscillating parallel to the plane of incidence. In the Fig. 6.7, a linearly polarized input beam is converted to an elliptically polarized reflected beam. For any angle of incidence greater than 0° and less than 90° , *p*-polarized light and *s*-polarized will be reflected differently. The amplitudes of the *s* and *p* components, after reflection and normalized to their initial value, are denoted by r_s and r_p , respectively. Ellipsometry measures the ratio of r_s and r_p , which is described by the fundamental equation of ellipsometry:

$$\rho = \frac{r_p}{r_s} = \tan(\psi)e^{i\Delta} \quad (6.2)$$

Thus, $\tan(\psi)$ is the amplitude ratio upon reflection, and Δ is the phase shift (difference), as shown in Fig. 6.8.

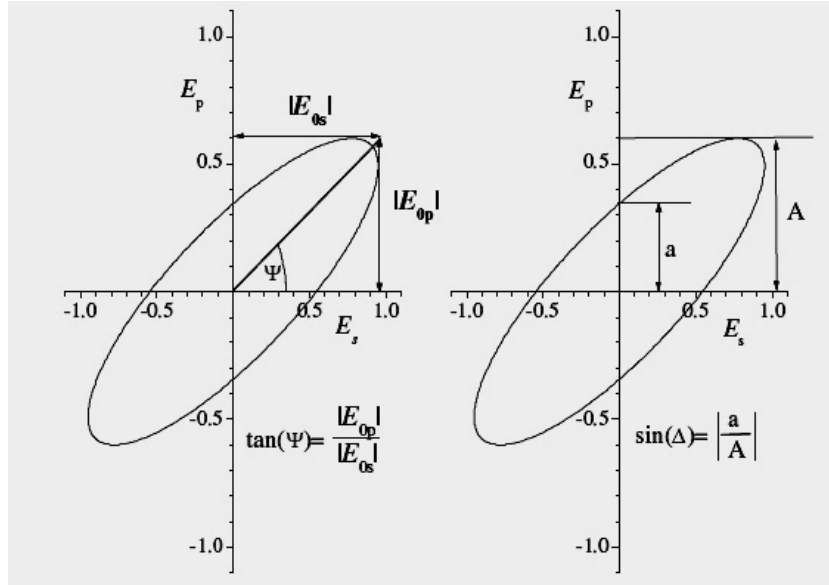


Figure 6.8: The polarization defined by the ratio between s - and p - polarized beam and the phase retardation between these two components.

Because ellipsometry measures the ratio of two values, it can be highly accurate and very reproducible. Since ellipsometry is measuring the ratio (or difference) of two values rather than the absolute value of either, it is very sensitive and reproducible characterization method. The desired information must be extracted through a model-based analysis using equations to describe interaction of light and materials. Using such models it is possible to extract information such as film thickness, dielectric function, surface roughness, anisotropic behavior and crystallinity of the films, from the SE spectra.

7 Optical properties of organic films of Alq_3 and α -NPD

The optical and structural properties of tris(8-hydroxyquinoline) aluminum (Alq_3) and N,N'-diphenyl-N,N'-bis(1-naphthyl)-1-1'-biphenyl-4,4'' diamine (α -NPD) films deposited by organic vapor phase deposition (OVPD) have been studied by spectroscopic ellipsometry (SE). Employing this technique enables the precise determination of the dielectric function as well as the thickness of the organic thin films of each material. This result can be explained by the characteristic features of the electronic states in organic molecules. [72]

7.1 Introduction

Organic light emitting diodes (OLEDs) are among the most promising applications of organic semiconductors. OLEDs offer high luminance, low power consumption, and full color capability. For this application, the highest possible quantum yield is of paramount importance. This yield depends upon the probability of radiative electron-hole recombination which is highest for amorphous materials where the electron and hole mobilities are low. [41] OLED prototypes consisting of sequentially deposited layers of hole- and electron transport materials have been demonstrated with active device thicknesses of only a few hundred nanometers or less. Tris-(8-hydroxyquinoline) aluminum (Alq_3) and N,N'-diphenyl-N,N'-bis(1-naphthyl)-1-1'-biphenyl-4,4'' diamine (α -NPD) are among the most commonly used electron-transport and hole-transport materials. To design Alq_3/α -NPD thin film based devices, the knowledge of the optical properties as well as the structural properties is therefore a necessity.

In recent years, the computation of optical properties has progressed considerably. There exist two computational tools, which are prominent for the calculation of electronic excitations. Calculations based on many-body perturbation theory, employing multivariable Green's functions, are computationally heavy calculations. Hence, computations for complex systems such as amorphous organic thin films are still beyond the present scope of the technique. [73] An alternative computational approach is time-dependent density functional theory (TDDFT), which offers the important practical advantage of a dependence on density rather than the need to use multivariable Green's functions. Although, TDDFT gives promising results for finite systems, it has significant disadvantages in the description of absorption spectra of organic solids. [74] In the electronic excitation of

organic materials, the tightly bound excitonic states, i.e. the Frenkel excitons, play an important role. [8] TDDFT still fails in practice to describe the exact optical response of organic materials due to its deficiency in describing these excitonic states. Hence, the most advanced computation schemes have not yet been adequate for the investigation of the optical properties of organic molecules. Therefore, in this study, we have focused on the precise measurement of optical properties using spectroscopic ellipsometry and the subsequent simulation of the dielectric function.

In this chapter, we report the results of an investigation using spectroscopic ellipsometry (SE) for the determination of optical and structural properties of Alq_3 and α -NPD films. The ellipsometry spectrum is sensitive to several material characteristics such as film roughness, film thickness, density and optical constants. In addition, XRR measurements and AFM have been performed as well to determine several film properties independently with high precision.

7.2 Experiments

Single layers of Alq_3 and α -NPD were deposited by organic vapor phase deposition (OVPD) on 8" Si wafers covered by a native Silicon dioxide (thickness approximately 3-4 nm). For each material, Alq_3 and α -NPD respectively, a series of six samples with different deposition rates, varying from 5.9 Å/s to 24.00 Å/s for Alq_3 and from 3.3 Å/s to 12.7 Å/s for α -NPD, have been investigated. The substrate temperature was kept at 5° C.

7.2.1 Spectroscopic ellipsometry measurements

SE spectra have been measured in the spectral range from 0.7 to 5.0 eV using a variable-angle SE (VASE, Woollam Co.). The ellipsometry spectra were acquired at angles of incidence near the Brewster angle of Si (74°), i.e. angles of 65°, 70°, and 75°, respectively were chosen. The spectra were fitted using the SCOUT software (©Wolfgang Theiss). [75]

An accurate model for the dielectric function, $\epsilon(\omega)$, is necessary for the accurate fitting of SE data or any form of electroreflectance. The dielectric function, $\epsilon(\omega) = \epsilon_1(\omega) + i\epsilon_2(\omega)$ fully describes the optical properties of any homogeneous medium at all photon energies $\hbar\omega$. $\epsilon_1(\omega)$ and $\epsilon_2(\omega)$ are the real and the imaginary part of the dielectric function, respectively. Values for $\epsilon(\omega)$ obtained from experimental data have the serious deficiency that they are not expressed as functions of electronic critical-point energies E_k . The construction of accurate model line shapes is necessary for the accurate determination of critical-point energies E_k , line widths Γ_k and the detailed characterization of optical materials. Such model should be able to describe the properties of the measured film with best precision.

In this study, the optical properties of Alq3 and α -NPD thin films have been modeled using both the standard harmonic oscillator [76] and the modified Kim oscillator model. [77] The harmonic oscillator (HO) model is a phenomenological model that approximate the continuum of transitions possible between band states in a solid, with the resultant critical-point structure, by a small discrete set of transitions. In the standard harmonic oscillator model of Erman *et al.*, the dielectric function, $\epsilon(\omega)$, is given by

$$\begin{aligned}\epsilon(\omega) &= \epsilon_1(\omega) + i\epsilon_2(\omega) \\ &= 1 - \sum_{k=1}^n A_k \left(\frac{1}{\hbar\omega - E_k + i\Gamma_k} - \frac{1}{\hbar\omega + E_k + i\Gamma_k} \right),\end{aligned}\quad (7.1)$$

where E_k is the resonance energy, A_k is the oscillator strength and Γ_k is the line-width broadening (damping) of the harmonic oscillator. Comparing Eq. 7.1 with Eq. 5.15 and Eq. 5.17 shows that HO model is much simpler and describes each single optical transition from a lower band to a higher band by a harmonic oscillator. In practice, the minimum possible number of oscillators is used to represent the dielectric function.

The Kim oscillator is an extension of the simple harmonic oscillator model originally developed to describe line broadening induced by electronic-vibronic interactions, as suggested by Kim *et al.*. This model allows a continuous shift of the line shape between a Gaussian and a Lorentzian profile. The energy-dependent broadening employed in this model is given by the empirical expression:

$$\Gamma'_k(\omega) = \Gamma_j \exp \left(-\frac{1}{1 + \sigma^2} \left(\frac{\hbar\omega - E_j}{\Gamma_j} \right)^2 \right). \quad (7.2)$$

The constant σ is called Gauss-Lorentz switch, which can vary from 0 to infinity. For $\sigma = 0$ a Gaussian lineshape is achieved, and large values of σ ($\sigma > 5$) lead to a Lorentzian broadening. At temperatures above 20 K, the absorption lineshape in molecular crystals is Gaussian and its width increases with temperature. [78] This broadening is due to the exciton-phonon coupling. [79], [80] Therefore, in this study the Gauss-Lorentz-switch, σ , has been set to zero.

7.2.2 XRR and AFM measurements

To independently determine the thin film structure and morphology, AFM and XRR measurements have been performed. The tapping mode of the AFM was employed to determine the surface roughness, including the surface morphology. Figure 7.1 shows an example of an AFM image of an Alq3 film deposited with a rate of 14.0 Å/s. For each sample, three AFM scans at different sample positions have been measured. The rms-roughness, which is defined as the height variance around the mean value, has been calculated for each AFM image.

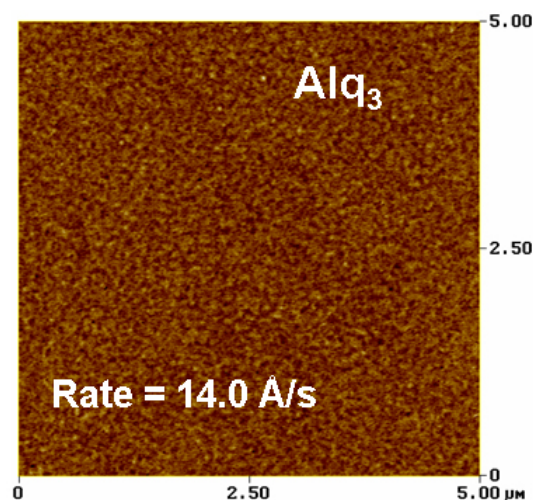


Figure 7.1: AFM image of the Alq_3 sample deposited with a rate of 14.0 \AA/s . The AFM scan size is $5 \mu\text{m} \times 5 \mu\text{m}$ and the gray scale corresponds to 5 nm . This sample is very smooth with an rms-roughness of 0.6 nm .

XRR provides the possibility to determine film density, thickness and surface roughness. XRR experiments were carried out using a Philips X'pert Pro MRD system with a wavelength of 1.54 \AA , (CuK_α). Figure 7.2 depicts the XRR spectrum of the same Alq_3 sample obtained with a deposition rate of 14.0 \AA/s . The decay of the oscillation amplitude of the XRR spectrum is due to the roughness while the period of the oscillations (Kiessig fringes) is related to the thickness of the film.

Often, for inorganic materials on top of typical substrates, the density of the film is higher than the density of the substrate. Therefore, the position of the total reflection edge determines the density of the film. However, in the case of organic films deposited on top of the Si substrate, the film density is less than the density of the substrate. In this case, for very small incidence angles, two critical angles have been observed. The first one is the position of the small dip which is related to the density of the organic film. The second edge, which is the main total reflection edge, is linked to the density of the Si substrate. Hence, in the case of organic films, it is the position of the small dip in the first part of the XRR spectrum which determines the film density. [81] [82]

7.3 Results and discussions

Spectroscopic ellipsometry measurements have been performed for both Alq_3 and α -NPD samples. In order to model and fit the ellipsometry data, the surface roughness has been assessed as the first important parameter which, in general, has an impact on the accuracy and precision of film thickness and optical property determination. The surface roughness has been obtained by AFM and XRR. The roughness values vary from 5 \AA to a maximum

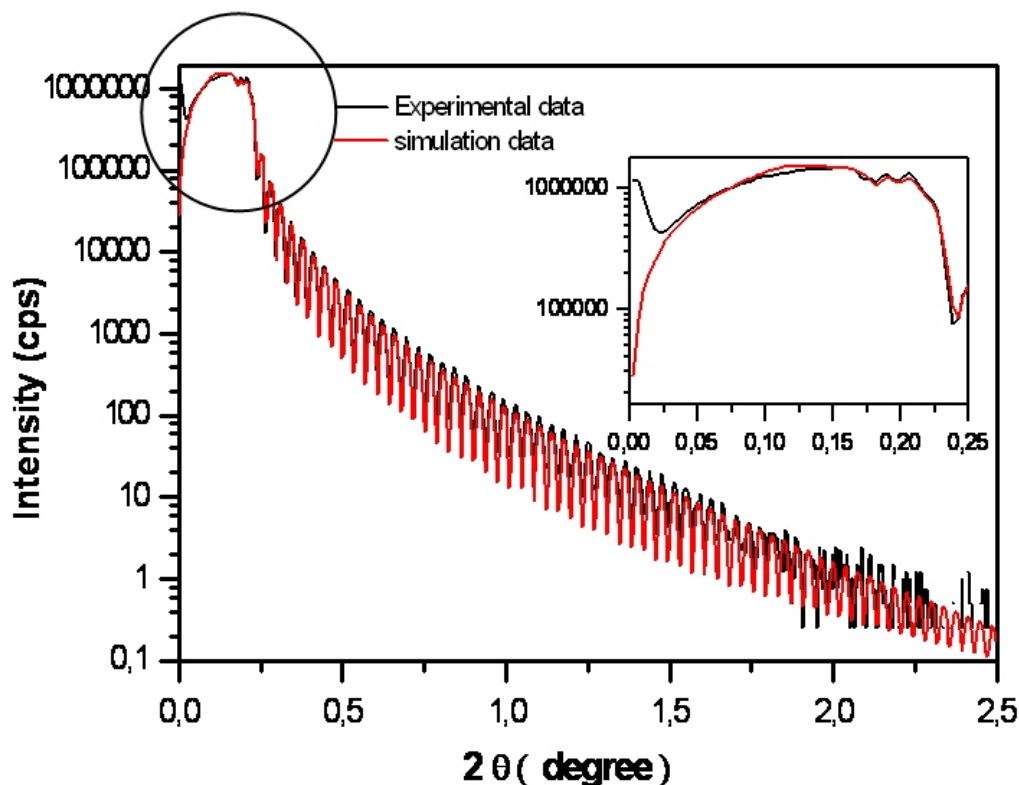


Figure 7.2: XRR spectrum of Alq_3 sample deposited with a rate of 14.0 \AA/s . From the oscillation period the thickness is determined as 141.2 nm . Since the film is extremely smooth (roughness 0.5 nm) there is only a very small decay of the oscillation amplitude. The film density has been determined from the position of the small dip in the first part of the spectrum (see insert).

of 14 \AA , which is very small in comparison with the wavelength of the incident beam used in ellipsometry. Hence, such a small roughness can be neglected in SE modeling without any considerable effect on the resulting accuracy. Therefore, as shown in Fig. 7.3, a three-phase model (organic film/Si-oxide/Si) was employed for the analysis. In this model, the optical constants obtained by Jellison were used for Si. [83] Furthermore, the optical response of the Si-oxide layer was described by a single harmonic oscillator model. The thickness of this layer was determined as 3.7 nm .

The standard harmonic oscillator is the first model considered in this work for the organic film. By using four independent harmonic oscillators, it is possible to derive the optical response and the thickness of the samples. This number of oscillators has been chosen, considering four main peaks in the dielectric function of the point-by-point fit. The data fitting is then applied by adjusting the model parameters to find the best-fit values of HO model parameters and the film thickness. The Marquardt-Levenberg algorithm is most commonly used to quickly determine the model that exhibits the smallest difference

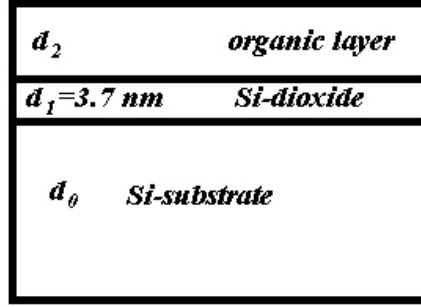


Figure 7.3: The three-phase model (organic film/Si-oxide/Si).

between the measured and calculated values. The difference is quantified by using mean squared error (MSE) defined by

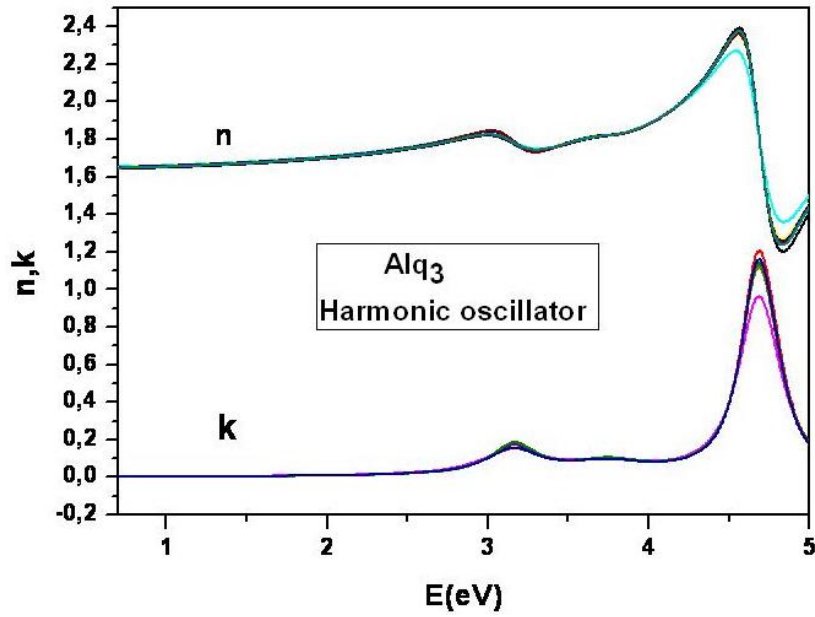
$$MSE = \frac{1}{2N - M} \sum_{i=1}^N \left[\left(\frac{\tan\psi_i^{Mod} - \tan\psi_i^{Exp}}{\sigma_{\psi,i}^{Exp}} \right)^2 - \left(\frac{\cos\Delta_i^{Mod} - \cos\Delta_i^{Exp}}{\sigma_{\Delta,i}^{Exp}} \right)^2 \right], \quad (7.3)$$

where N is the number of $\psi - \Delta$ pairs, and M is the number of variable parameters used in the model.

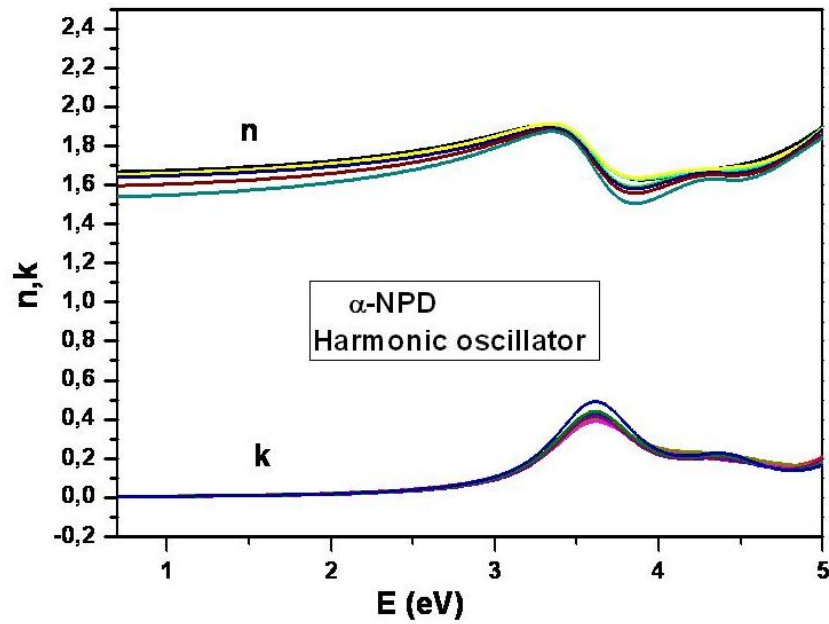
Our fitting results show that MSE of the HO fits (average for all Alq_3 samples) is 0.0061. MSE of the fits (average for α -NPD ones) is 0.0226. The refractive index n and extinction coefficient k are shown in Fig. 7.4 for the series of Alq_3 and α -NPD samples.

The generalized Kim oscillator model has been applied as well to fit the ellipsometry spectrum of these samples. In this model four oscillators with Gaussian broadening have been employed. Fig. 7.5 shows the SE spectrum for an Alq_3 sample deposited with a rate of 14.0 Å/s. The MSE of this fit (Fig. 7.5) using Kim oscillators is 0.0009, while the corresponding value for harmonic oscillators is 0.0029. This shows clearly that using Kim's model improves the quality of the fits. The best-fit parameters employing Kim's model are listed in Table 7.1 and Table 7.2. The dispersion of the optical constants for Alq_3 and α -NPD deposited with different rates is shown in Fig. 7.6. The average of fit deviation from the experimental spectrum (MSE) is 0.0012 for Alq_3 samples and 0.0117 for α -NPD ones, using Kim model.

By using X-ray reflectometry (XRR) it is possible to determine the density of thin films. The film density is related to the optical properties of the film, via the Clausius-Mossotti equation. [8] Table 7.3 and Table 7.4 contain the values derived for the density of Alq_3 and α -NPD films for different deposition rates. These values clearly show that with changing deposition rate the density of the films remains constant within the error bar of $\pm 0.02\text{g/cm}^3$. Therefore the optical constants of the samples are expected to be the



(a) Refractive index n and extinction coefficient k of Alq_3 samples.



(b) Refractive index n and extinction coefficient k of α -NPD samples.

Figure 7.4: Refractive index n and extinction coefficient k , obtained for the harmonic oscillator model of Alq_3 and α -NPD samples deposited with different rates.

same for different deposition rates. This finding is confirmed by the optical constants determined employing the Kim simulation model. Comparing the refractive index n and extinction coefficient k in Fig. 7.6 and Fig. 7.4 shows that by using the Kim model it

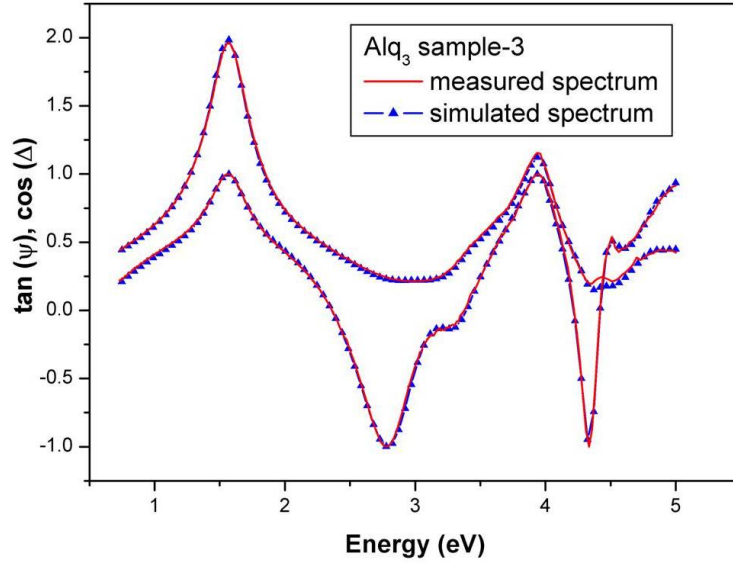


Figure 7.5: Measured and simulated ellipsometry spectra, at an angle of 70° , for the Alq_3 sample deposited with a rate of 14.0 \AA/s employing the Kim model.

is possible to achieve a unique SE fit of the dielectric function for the Alq_3 and α -NPD films, respectively independent of deposition rate. However, this is not the case if the harmonic oscillator model is used.

In the thickness range used here, XRR is considered the most accurate method for thickness determination. [84] Therefore, in this study, the thickness determined from XRR was used as a reference to compare the thickness values derived from the harmonic oscillator and the generalized Kim models. In Table 7.4 and Table 7.3 the thickness values determined by XRR and SE simulations are shown. Although the thickness results derived from the harmonic oscillator model in the case of Alq_3 films seem to show a good agreement with the XRR data, this model does not provide a good agreement for the α -NPD samples. Considering both series of Alq_3 and α -NPD samples, the Kim model can provide the more precise thickness values with very low deviation in comparison with the XRR data. The average multiplication factor of both series is 0.986 ± 0.007 for the Kim model, while for the Harmonic oscillator model it is 1.022 ± 0.016 . This comparison illustrates that the film thickness determined by the generalized Kim model can be con-

Kim oscillator	Resonance energy, $E_k(\text{eV})$	Oscillator strength, $A_k(\text{eV})$	Damping $\Gamma'_k(\text{eV})$
1	3.15	0.81	0.46
2	3.79	0.99	0.89
3	4.64	2.14	0.33
4	6.29	5.93	1.76

Table 7.1: Generalized Kim model parameters for fitting SE spectra of Alq_3 thin film.

Kim oscillator	Resonance energy, $E_k(eV)$	Oscillator strength, $A_k(eV)$	Damping $\Gamma'_k(eV)$
1	3.57	1.94	0.69
2	4.41	1.36	0.67
3	5.69	4.45	0.92
4	6.64	3.74	0.00

Table 7.2: Generalized Kim model parameters for fitting SE spectra of α -NPD thin film.

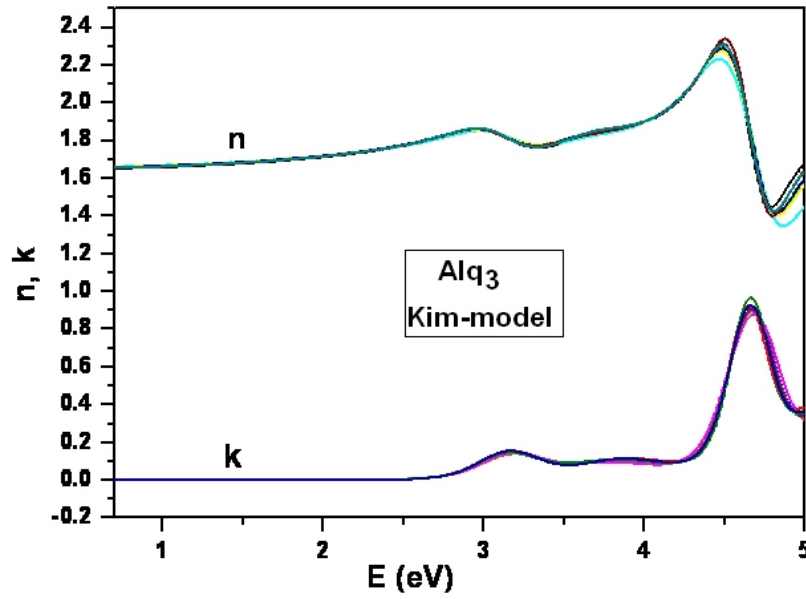
Sample name	Deposition rate ($\text{\AA}/s$)	XRR thickness (nm)	XRR density (g/cm^3)	Harmonic model thickness(nm)	Kim model thickness(nm)
Alq_3 -1	5.9	117.4	1.31	116.4	114.7
Alq_3 -2	10.4	126.4	1.30	124.8	123.4
Alq_3 -3	14.0	141.2	1.31	140.8	139.4
Alq_3 -4	16.5	125.3	1.30	125.0	123.6
Alq_3 -5	20.2	123.3	1.31	122.8	121.3
Alq_3 -6	23.6	119.2	1.31	118.7	116.9
Multiplication factor				0.995 ± 0.004	0.982 ± 0.005

Table 7.3: Density and thickness for different Alq_3 samples.

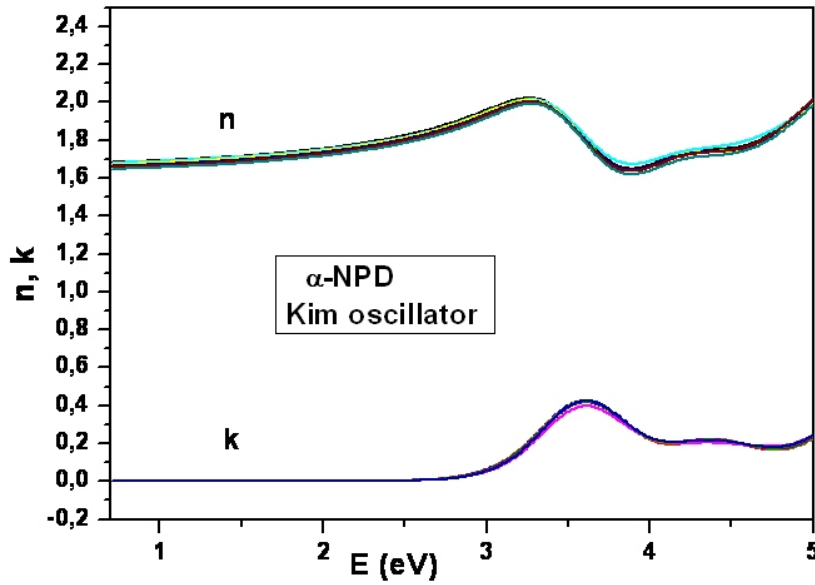
Sample name	Deposition rate ($\text{\AA}/s$)	XRR thickness (nm)	XRR density (g/cm^3)	Harmonic model thickness(nm)	Kim model thickness(nm)
α -NPD-1	3.3	96.7	1.12	96.5	94.0
α -NPD-2	5.4	82.7	1.11	84.9	81.6
α -NPD-3	7.1	87.1	1.12	90.3	87.0
α -NPD-4	8.4	84.8	1.12	90.3	84.3
α -NPD-5	10.4	79.3	1.10	81.9	78.3
α -NPD-6	12.7	64.7	1.13	70.5	64.7
Multiplication factor				1.040 ± 0.029	0.990 ± 0.010

Table 7.4: Density and thickness for different α -NPD samples.

sidered as more precise and accurate. Figure 7.7 demonstrates the excellent agreement of the thickness values derived from the Kim model with respect to the XRR thickness measurements as compared with the Harmonic oscillator model.



(a) Refractive index n and extinction coefficient k of Alq_3 samples.

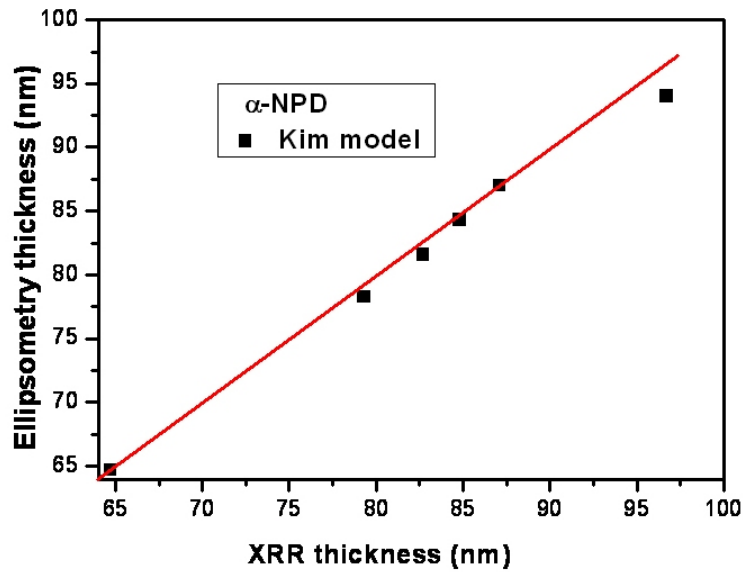


(b) Refractive index n and extinction coefficient k of α -NPD samples.

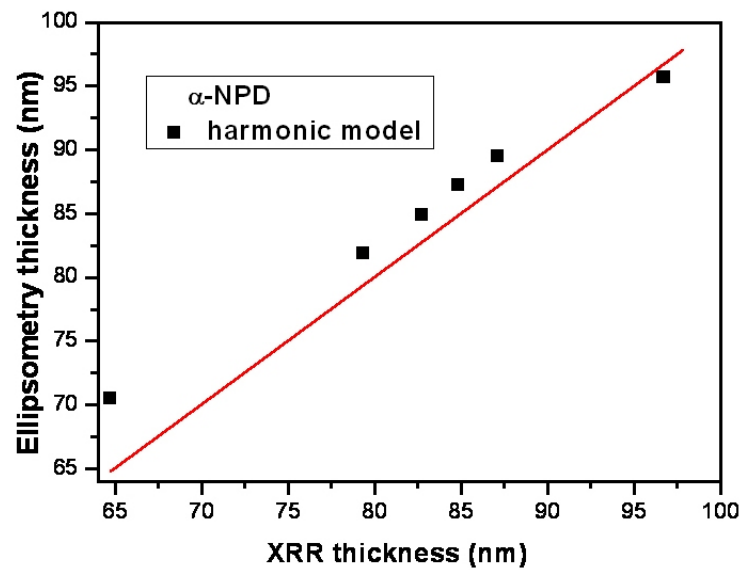
Figure 7.6: Refractive index n and extinction coefficient k , using the generalized Kim model for (a) Alq_3 and (b) α -NPD samples deposited with different rates.

7.4 Conclusions

The dielectric function of Alq_3 and α -NPD films have been determined in the spectral range of 0.7 eV to 5.0 eV by spectroscopic ellipsometry. The optical constants of these



(a) Film thicknesses determined using XRR vs. the film thickness obtained from the generalized Kim oscillator model.



(b) Film thicknesses determined using XRR vs. the film thickness obtained from the Harmonic oscillator model.

Figure 7.7: Comparison of film thicknesses determined using XRR vs. the film thickness obtained from the generalized Kim oscillator model (a) and Harmonic oscillator (b) for α -NPD samples. The straight line with a slope of 1.0 has been plotted as a reference to show the agreement between the film thickness determined by XRR and SE.

samples were determined using the normal harmonic oscillator and the generalized Kim

model with Gaussian broadening. AFM and XRR measurements have been performed for the independent determination of film structure. Employing the Kim oscillator model, the quality of the fit has been improved in average by the factor of 4. Furthermore, using the Kim model the film thickness is reproduced to within 1% accuracy. Moreover, we have shown that by using the generalized Kim model, we can obtain a single dielectric function for all samples of the same material. This is in line with the constant film density values determined by XRR. The superior quality of the fits employing the Kim model seems to be attributed to the better description of electron-phonon coupling in the organic materials.

8 The theory of thin film growth

The study of growth processes has always constituted, explicitly or implicitly, an integral part of solid state physics and materials science. Indeed, most properties of real materials depend crucially on their structure and morphology. Surface and interface roughness are often a relict of the nonequilibrium conditions under which the material has formed. During the last decades the science of thin film growth has progressed rapidly as evidenced impressively by different modern deposition techniques. This allows for the engineering of solid state devices at the level of individual atomic/molecular planes. Nevertheless, the success of these deposition techniques depends crucially on the ability to control the disordering effects of the non-equilibrium growth conditions, and to assess, at least empirically, the relationship between the growth conditions and the resulting structure. Apart from its outstanding technological significance, the growth of solids is of considerable fundamental interest, since it may provide us with important clues to the way in which complex structures form in nature, through the agglomeration of simple, microscopic processes operating in a highly disordered, noisy environment. [85]

8.1 General concepts of thin film growth

8.1.1 Surface free energy

Crystal and thin film growth are enormously rich subjects with many different facets and theoretical approaches. Here we shall only briefly touch on selected aspects which we feel are important in the present context and help to explain the issues related to thin film growth. One approach to describe the various relevant interactions uses the concept of surface and interface energies, γ , similar to what is done for wetting phenomena. Typically, the surface energies, i.e. the relative contributions of the free substrate surface, γ_s , the film surface, γ_f , and the film-substrate interface, γ_i , are then related to the different growth modes.

The common classification of growth modes, based on thermodynamic arguments [86], which has been mainly developed for *epitaxial* growth, [87], [88] treats film growth analogous to the surface tension consideration of a liquid on a solid substrate. This consideration leads to three growth modes that are illustrated in Fig. 8.1.

- Layer-by-layer growth, also called two-dimensional (2D) or Frank-van der Merwe growth, is predicted if the sum of the surface free energy of the deposited film and

the free energy of the film-substrate interface is comparable to the surface free energy of the free substrate surface (Fig. 8.1(a)).

- The case of

$$\gamma_s < \gamma_i + \gamma_f. \quad (8.1)$$

results in the formation of three-dimensional islands also called three-dimensional (3D) or Volmer-Weber growth (Fig. 8.1(b))

- For the condition that

$$\gamma_s > \gamma_i + \gamma_f. \quad (8.2)$$

several monolayers grow in the layer-by-layer mode forming the so-called wetting layer before the formation of 3D islands starts. This growth is called Stranski-Krastanov mode [89] (Fig. 8.1(c)).

Because 'growth' is per definition a non-equilibrium process determined by kinetic phenomena, growth morphologies will deviate more or less from the above thermodynamic picture.

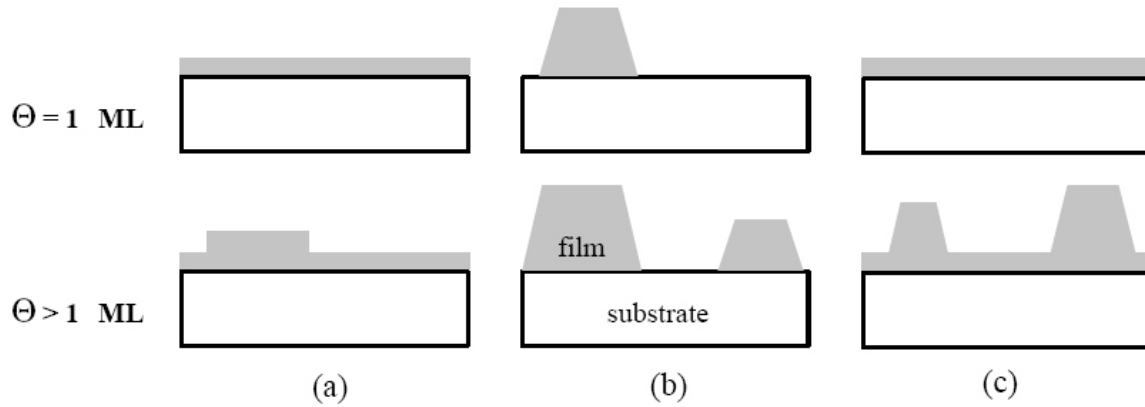


Figure 8.1: The three growth mechanisms close to thermodynamic equilibrium. (a) layer-by-layer growth (Frank-van der Merwe), (b) island growth (Volmer-weber) and (c) layer-plus-island growth (Stranski-Krastanov). The situations are shown in cross-sectional representation for a coverage Θ of one complete layer (top) and for the continuation of growth at higher coverages (bottoms). [90]

8.1.2 Microscopic processes

It should be emphasized that growth is actually a non-equilibrium phenomenon, and equilibrium or near-equilibrium energy considerations alone cannot properly account for all

growth scenarios. Thus, a dynamic description is needed. This description has to take into account the flux of adsorbates towards the surface (corresponding to a certain supersaturation), the adsorption and re-desorption probabilities, and the diffusion processes on the surface (interlayer and intralayer) and their respective barriers. The three main processes which are depicted in Fig. 8.2, are described in the following.

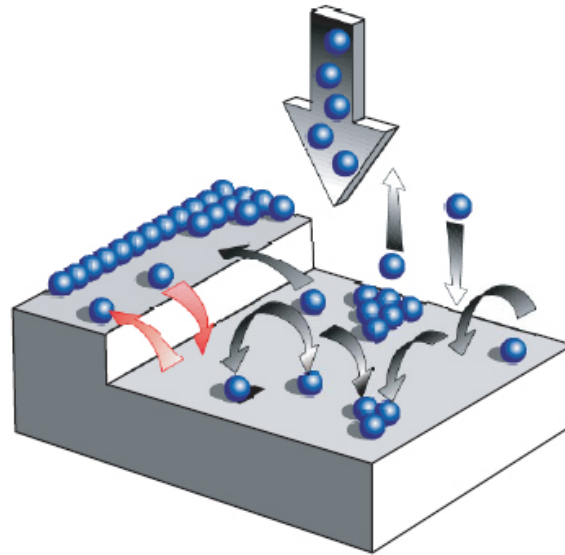


Figure 8.2: Schematic of processes relevant in thin film growth, such as adsorption (as a result of a certain impingement rate), (re-)desorption, intra-layer diffusion (on a terrace), interlayer diffusion (across steps), nucleation and growth of islands. [91]

- **Adsorption:**

A particle from the vapor phase arrives at a random position on the interface, forms bonds with the surface and sticks. This process is termed *adsorption*. There are several methods for the material deposition such as MBE (Molecular Beam Epitaxy), VTE (Vapor Thermal Evaporation), OVPD (Organic Vapor Phase Deposition).

- **Desorption:**

An effect competing with adsorption is desorption during which some particles deposited on the surface leave this interface. The desorption probability depends on how strongly the particle is bonded to the surface. The strength of these bonds depends on the type of particle and the local geometry of the surface where particles stick. The strength of a bond is expressed in terms of the amount of energy needed to break it. The usual procedure for measuring the lifetime of a deposited molecule or atom is to measure the average time τ spent by the atom on the surface from deposition to desorption. According to the Arrhenius law, this life time can be written in the form

$$\tau = \tau_0 \exp\left(\frac{E_D}{KT}\right). \quad (8.3)$$

Here, E_D is the characteristic desorption energy to release an atom from the surface.

- **Surface diffusion:**

From a microscopic point of view, surface diffusion is an activated process. For a particle on the surface to diffuse to the next position, it must overcome the lattice potential existing between two neighboring positions. This excess energy required for diffusion, E_0 , is the microscopic origin of the lattice potential schematically illustrated in Fig. 8.3. In this figure, atom A forms two bonds with the surface atoms which is energetically favorable, corresponding to a minimum of the lattice potential $V(x)$. In order to diffuse, it must move into an intermediate position, such as B , where there is only one strong bond. This is an energetically unstable configuration, corresponding to maximum in the lattice potential.

The magnitude of the diffusion barrier depends both on the substrate orientation and the nature of the diffusing particle. The average number of jumps in a unit time interval has no exponential temperature dependence, given by Arrhenius law

$$N = \omega_D \exp\left(-\frac{E_0}{k_B T}\right), \quad (8.4)$$

where ω_D is the frequency of small atomic oscillations (Deby frequency) and E_0 is the activation energy needed for diffusion. Measuring the number of jumps i.e., the average distance traveled by an atom on the surface is a standard experimental technique used for determining the activation energy E_0 needed for diffusion.

8.2 Quantitative parameters

In the last two decades a theoretical framework has been established, which relates growth mechanisms to different parameters which quantitatively describe surface morphology and a set of scaling exponents for describing the dependence of the surface roughness on film thickness and lateral length scale. Much effort has been spent to theoretically investigate scaling exponents for certain growth models, as well as to determine them experimentally. [92], [93], [94] In this section we will study the quantitative description of the surface morphology.

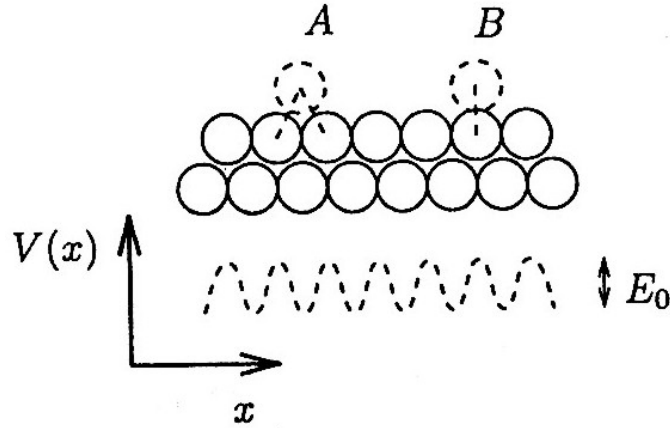


Figure 8.3: Schematic illustration of the lattice potential and its microscopic origin. Position *A* is energetically more favorable and corresponds to a minimum of the lattice potential $V(x)$. Diffusion occurs by moving into the intermediate position *B*, which is an energetically unstable configuration, corresponding to a maximum in the lattice potential.

8.2.1 Surface roughness

It is known that to derive a quantitative information of a surface morphology, [92], [94] one may consider a sample of size L and define the mean height of the growing film \bar{h} by

$$\bar{h}(t) \equiv \frac{1}{L} \int_{-L/2}^{L/2} h(\mathbf{r}, t) d\mathbf{r} \quad (8.5)$$

where $h(\mathbf{r}, t)$ is the height of surface at position \mathbf{r} and time t . If the deposition rate (number of particles arriving on surface) is constant, the mean height increases linearly with time,

$$\bar{h}(t) \sim t. \quad (8.6)$$

The rms-roughness is defined as the rms-fluctuations in the height,

$$R_{rms}(L, t) \equiv \left(\langle (h(\mathbf{r}) - \bar{h})^2 \rangle_{\mathbf{r}} \right)^{1/2}, \quad (8.7)$$

where $\langle \dots \rangle$ denotes an averaging over different positions on the sample.

Another quantity that scales in the same way as the rms-roughness R_{rms} is the height difference correlation function,

$$C(l, t) \equiv \left(\langle (h(\mathbf{r}, t') - h(\mathbf{r}', t' + t)) \rangle_{\mathbf{r}, t'} \right)^{1/2} \quad |\mathbf{r} - \mathbf{r}'| = l. \quad (8.8)$$

where $\langle \dots \rangle$ means the average over all possible pairs in the matrix that are separated by $|\mathbf{r} - \mathbf{r}'| = l$.

8.2.2 Lateral correlation length

Moreover, to quantify structure size on the surface, lateral correlation length can be calculated. Lateral correlation length is the distance over which the heights 'know about' each other or the characteristic distance over which they are correlated. This implies that the different sites of the surface are not completely independent, but depend upon the height of the others. [92] In order to obtain this quantity, the following method can be used. First, function $G(r)$, named height-height correlation function is calculated by

$$\begin{aligned} G(r) &= \langle G(\mathbf{r}) \rangle_{|\mathbf{r}|=r} \\ &\equiv \langle \langle (h(\mathbf{r}' + \mathbf{r}) - \bar{h}) \times (h(\mathbf{r}') - \bar{h}) \rangle_{\mathbf{r}'} \rangle_{|\mathbf{r}|=r}, \end{aligned} \quad (8.9)$$

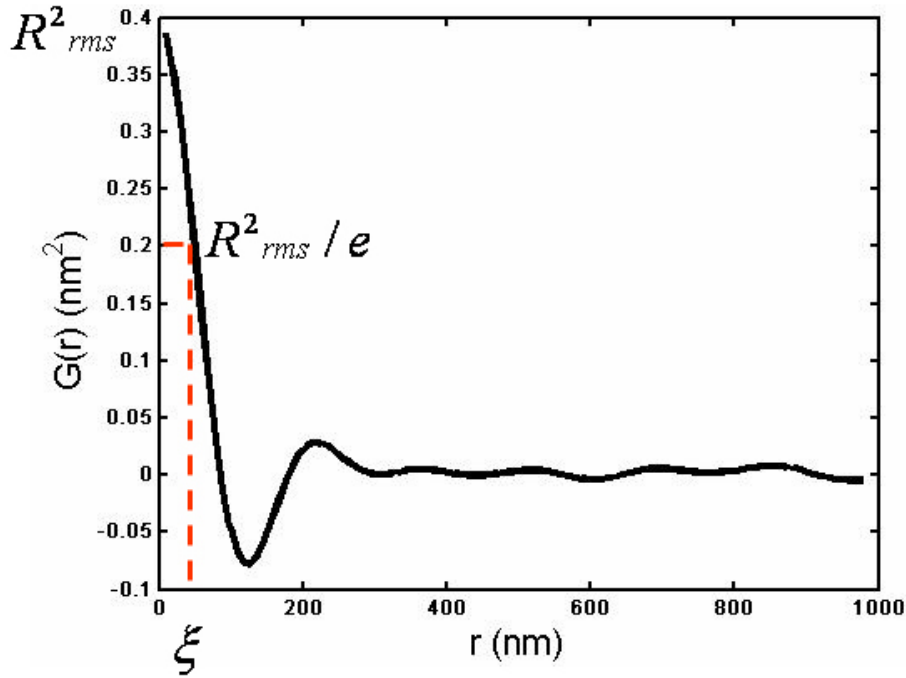


Figure 8.4: Height-height correlation function vs. length scale. Lateral correlation length corresponds to $G(\xi) = R_{rms}^2/e$ and the maximum value, $G(0) = R_{rms}^2$, yields the root mean square roughness.

In this equation (Eq. 8.9), $G(0) = R_{rms}^2$ yields the root mean square roughness. Next, $G(\xi) = R_{rms}^2/e$ defines the lateral length scale ξ in order to obtain *lateral correlation length* as $4 \times \xi$. [90], [88] As an example Fig. 8.4 show height-height correlation function

versus length scale for the height fluctuations of a sample morphology. The lateral length scale at which the height-height correlation function falls off to $1/e$ of its maximum value is shown as ξ . Four times of this value $4 \times \xi$ is called correlation length and depicts the quantified measure of the lateral structure size on the surface.

8.2.3 Scaling concepts and critical exponents

One of the modern concepts used to study various roughening processes is *scaling*. Scaling has a surprising power of prediction, simple manipulations allowing us to connect apparently independent quantities and exponents. We shall see that many measurable quantities obey simple *scaling relations*.

For example, to monitor the roughening process quantitatively, we measure the height difference correlation, $C(l, t)$, as a function of time. By definition, the growth starts from a horizontal line (the substrate); the interface at time zero is simply a straight line, with zero roughness. As deposition occurs, the interface gradually roughness.

A typical plot of the time evolution of the surface height difference correlation function has two regions separated by a 'crossover' time t_x , as shown in Fig. 8.5. It should be noted once again that height difference correlation function, scales in the same way as rms-roughness (Sec. 8.2.1) .

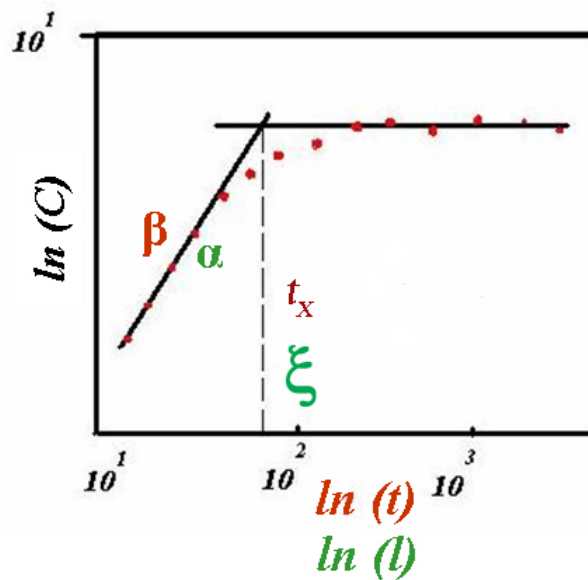


Figure 8.5: Scaling behavior of surface roughness which is shown as height difference correlation function vs. length scale (green) and time (red).

1. Initially, the correlation $C(l, t)$ increases as a power of time,

$$C(l,t) \sim t^\beta \quad [t \ll t_x] \quad (8.10)$$

where t_x is called saturation thickness.

The exponent β which is named the *growth exponent*, characterizes the time-dependent dynamics of the roughening process.

2. The power-law increase in correlation $C(l,t)$ as well as the roughening process do not continue indefinitely, but is followed by a saturation regime, the horizontal region of Fig. 8.5. The crossover time, t_x , is called the saturation time.

Furthermore, as it is shown in Fig. 8.5, the height difference correlation function, $C(l,t)$, has the following behavior with respect to the length scale

$$C(l,t) \sim l^\alpha \quad [l \ll \xi]. \quad (8.11)$$

This power law is only valid for small lengths. $C(l)$ vs. l saturates at the length scale equal to lateral correlation length ξ .

The ratio of exponents α and β is called the *dynamic exponent*:

$$z = \frac{\alpha}{\beta}. \quad (8.12)$$

Studying such scaling relations will allow us to define universality classes. The universality class concept is a product of modern statistical mechanics, and codifies the fact that there are but a few essential factors that determine the exponents characterizing the scaling behavior. Thus different systems which at first sight may appear to have no connection between them, behave in a remarkably similar fashion.

8.3 Different growth models

In this section we will begin the systematic investigation of different growth processes. We will start from the simplest growth model (random deposition) and continue to more complicated ones such as the Raible [95] model. Our main focus will be models which can explain the growth of amorphous thin films. While the models are mainly motivated by their simplicity and should not be expected to precisely describe any specific system, they should be able to explain structural properties of thin films to a good approximation. [92], [93], [85]

8.3.1 Random deposition

In this part, the simplest growth model, called random deposition is introduced. The simplicity of this model makes it possible to construct a continuum growth equation and to determine the scaling exponents exactly. Figure 8.6 demonstrates the schematic view of the discrete RD model in one dimension. From a randomly chosen site over the surface, a particle falls vertically until it reaches the top of the column under it, whereupon it is deposited.

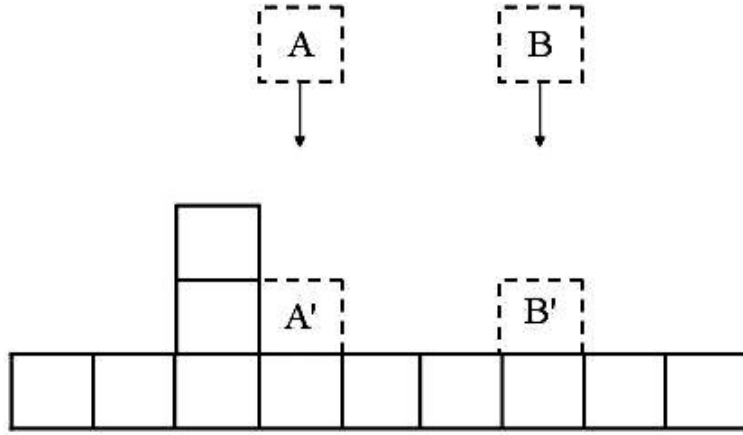


Figure 8.6: The random deposition, RD, model for discrete one dimensional system. Particles A and B are dropped from random positions above the surface and are deposited directly on the top of the column under them.

Because the RD model is simple, it is possible to calculate exactly all the relevant quantities using the microscopic growth rules. [96]. This is not the case for the other growth models which are more complicated. In order to study analytically such growth models, alternative methods have been introduced. One particularly successful approach is to associate a stochastic growth equation with the given growth process.

In order to illustrate this approach, a differential equation for describing RD growth is introduced. The goal is to find the variation with time of the height $h(\mathbf{r}, t)$ at any position \mathbf{r} on the substrate. In general, the growth can be described by the continuum equation:

$$\frac{\partial h(\mathbf{r}, t)}{\partial t} = \Phi_N(\mathbf{r}, t), \quad (8.13)$$

where $\Phi_N(\mathbf{r}, t)$ is the number of particles per unit time arriving on the surface at position \mathbf{r} and time t . Since the particles are deposited on random positions, the particles flux is not uniform and has random nature. Hence, by decomposing Φ_N into two terms, so that Eq. 8.13 becomes

$$\frac{\partial h(\mathbf{r},t)}{\partial t} = F + \eta(\mathbf{r},t) \quad (8.14)$$

The first term is F , the average number of particles arriving at position \mathbf{r} . The second term $\eta(\mathbf{r},t)$ is an uncorrelated random number with zero configurational average which represents the random fluctuations in the deposition process. The noise has no correlations in space and time and its first and second moments are given by

$$\langle \eta(\mathbf{r},t) \rangle = 0,$$

$$\langle \eta(\mathbf{r},t) \eta(\mathbf{r}',t') \rangle = 2D \delta(\mathbf{r} - \mathbf{r}') \delta(t - t'). \quad (8.15)$$

where the brackets denote ensemble averaging and D the fluctuation strength. Using Eq. 8.13, critical exponents can be analytically determined. Thus, for RD model, growth exponent is obtained as

$$\beta = \frac{1}{2}. \quad (8.16)$$

Since, the columns are not correlated and there are no correlations in this model, the correlation length ξ is always zero. Hence, the interface does not saturate and the roughness exponent α is not defined.

8.3.2 Linear theory

In this chapter, we study another growth model that leads to a correlated surface. This model is called *random deposition with surface relaxation* (RDSR). There is no exact solution to the discrete version of the model. In this section a linear equation will be presented to construct the growth equation. This equation can be solved exactly to determine the values of the scaling exponents. [92]

The model of random deposition with surface relaxation (RDSR) is constructed by including surface relaxation in RD model. As it is demonstrated in Fig. 8.7, each particle falls along a single column toward the surface, it reaches the interface, during a finite diffusion along the surface, it relaxes to a nearest neighbor if it has a lower height. As a result of the relaxation process, the final interface will be smooth, compared to the model without relaxation.

The simplest equation describing the fluctuations of an equilibrium interface, called the Edwards-Wilkinson (EW) equation [97], has the form

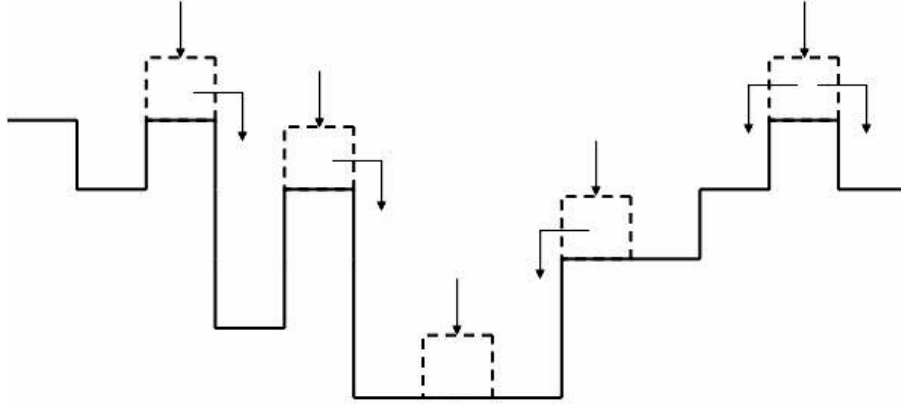


Figure 8.7: Random deposition with surface relaxation (RDSR). The freshly-deposited atoms do not stick irreversibly to the site they fall on, but rather they can 'relax' to a nearest neighbor if it has a lower height.

$$\frac{\partial h(\mathbf{r},t)}{\partial t} = a_1 \nabla^2 h + \eta(\mathbf{r},t). \quad [EW]. \quad (8.17)$$

Here a_1 is sometimes called a 'surface tension'. For the negative values, $a_1 < 0$, the $a_1 \nabla^2 h$ term tends to roughen the interface, however, for the positive values, $a_1 > 0$ this term smoothens the surface. A simple but intuitive geometrical interpretation, shown in Fig. 8.8, illustrates the smoothing effects of the Laplacian term $a_1 \nabla^2 h$ with $a_1 > 0$. Its most important property is smoothing/roughening by 'redistributing' the irregularities on the interface, while maintaining the average height unchanged. For the case of $a_1 > 0$, as shown in Fig. 8.8, materials are taken from the highest point and 'redistributed' on the two sides, which smoothens the surface. For the case of $a_1 < 0$ materials are going to the top hills rather than the lower parts which leads to an increase of the surface roughness.

After, solving EW equation, Eq. 8.17, the critical exponents have the form

$$\alpha = \frac{2-d}{2}, \quad \beta = \frac{2-d}{4}, \quad z = 2. \quad [EW] \quad (8.18)$$

As it is clear from Eq. 8.18, the scaling exponents depends on the dimension of the interface. For $d > 2$, the roughness exponent α becomes negative, which means that the interface is flat. Every noise-induced irregularity which generates nonzero width is suppressed by the surface tension.

8.3.3 Nonlinear models

In the previous section, we have discussed the results of the linear growth in terms of the EW equation. By adding the nonlinear terms to the growth equation, the results

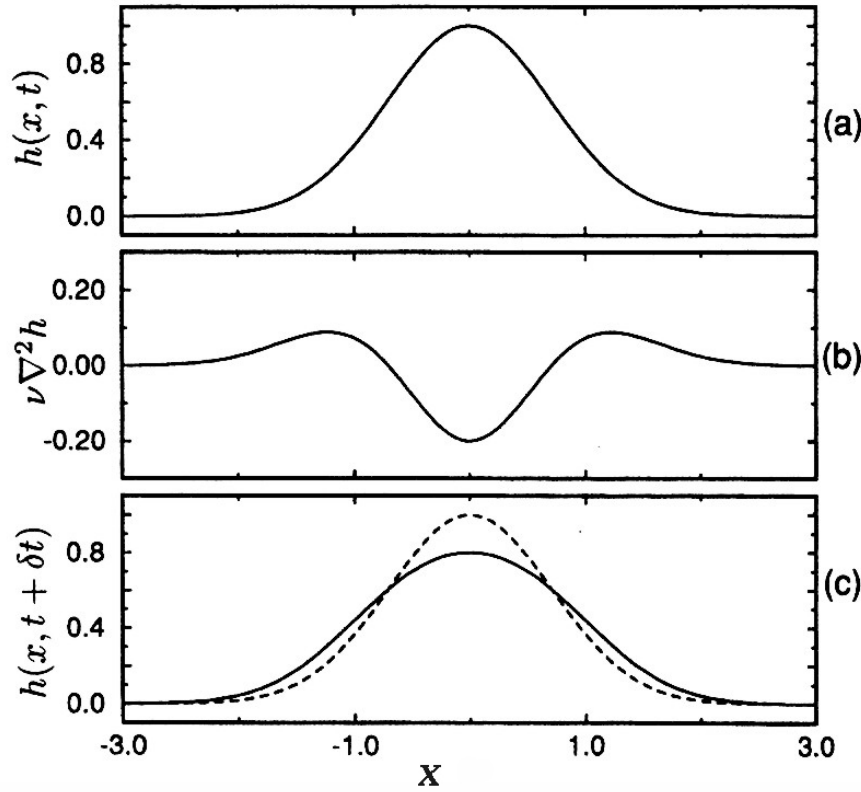


Figure 8.8: The effects of the Laplacian term $a_1 \nabla^2 h$ on surface morphology. (a) Assumed 'bump' in the height profile of the interface at time t . (b) Laplacian term $a_1 \nabla^2 h$ which is negative at the maximum of h . (c) At time $t + \delta t$, with $a_1 > 0$ the height of the original 'bump' reduces by redistributing surface height.

and predictions of this linear theory change. The first extension of the EW equation to include nonlinear terms, suggested by Kadar, Parisi and Zhang, is well known as the KPZ equation. [93]

One example of the systems with nonlinear behavior is *ballistic deposition* (BD). Figure 8.9 illustrates the schematic view of BD. This model is also an extension of RD by considering the new rule that the arriving particles stick to their nearest neighbors. It should be noted that the main difference between the BD model with the RDSR model is that, in RDSR, particles arrive at the surface and then relax, while for BD they stick to the first particle they meet.

The nearest-neighbor (NN) sticking rule in ballistic deposition induced lateral growth which is in Fig. 8.10. This implies that growth occurs in the direction of the local normal to the interface. This nonlinear term is the essential term in order to obtain the KPZ equation from the EW equation.

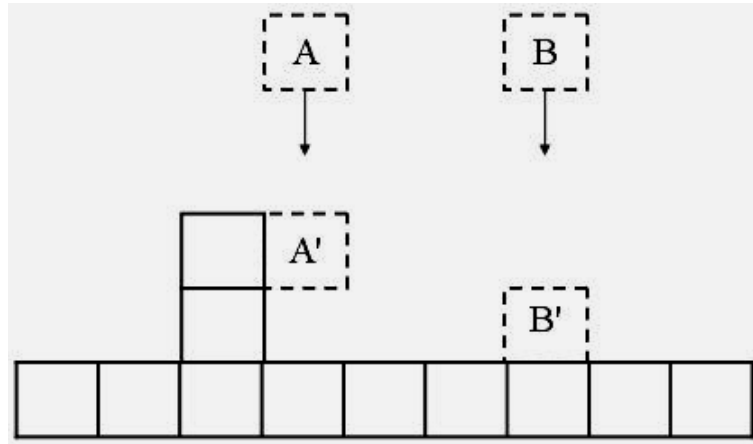


Figure 8.9: The ballistic deposition model with the nearest-neighbor (NN) sticking rule, illustrating two sticking possibilities for the newly-deposited particles.

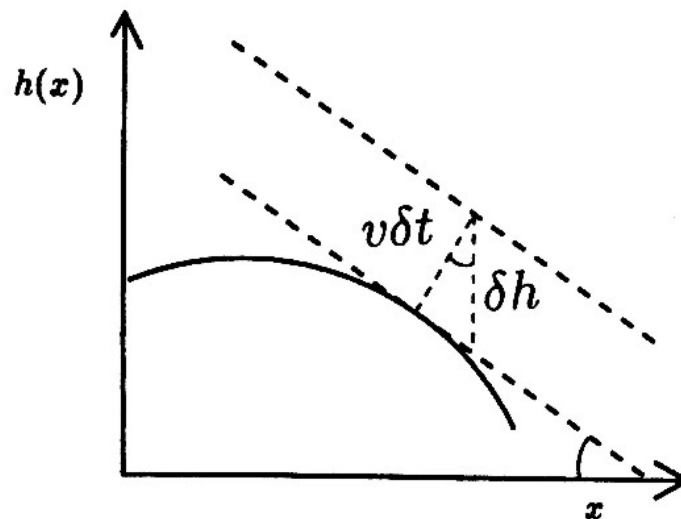


Figure 8.10: The lateral growth in the KPZ equation. Growth occurs along the local normal v .

$$\frac{\partial h(\mathbf{r}, t)}{\partial t} = a_1 \nabla^2 h + a_2 (\nabla h)^2 + \eta(\mathbf{r}, t). \quad [KPZ] \quad (8.19)$$

The first term is the same as in the EW equation and describes smoothening/roughening of the surface caused by particle redistribution. The second term is the nonlinear part of the growth equation. In order to better understand the effect of the nonlinear term, geometrical interpretation of this term has been illustrated in Fig. 8.11. Thus we see that the nonlinear term increases the height of the interface by adding more material to the

parts of the interface where the local slope is larger, and the average height of the surface increases.

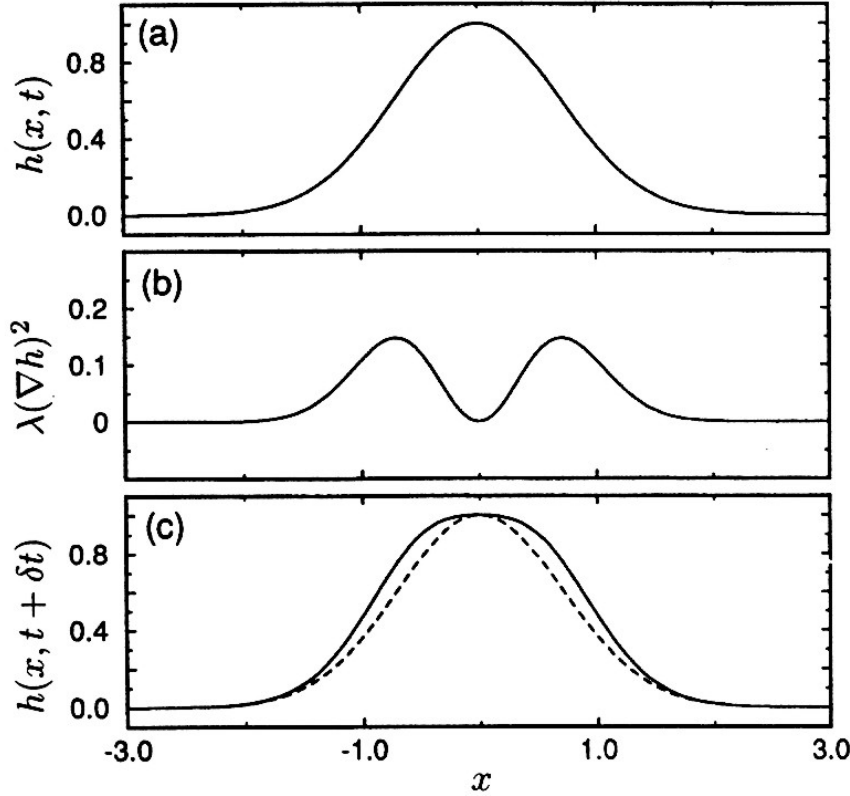


Figure 8.11: The effect of the nonlinear term $a_2(\nabla h)^2$ in the KPZ equation on the morphology of the surface. (a) Assumed 'bump' in the height profile of the interface at time t . (b) Laplacian nonlinear term $a_2(\nabla h)^2$ which is always positive. (c) At time $t + \delta t$, with $a_2 > 0$ the height of the interface increases by adding more 'material' to the parts of the surface where the local slope is larger.

Considering the KPZ model, it is possible to obtain the scaling exponents for this model. An exact analytical solution for this problem is only available for the one dimensional problem. Thus for $d = 1$ the scaling exponents are

$$\alpha = \frac{1}{2}, \quad \beta = \frac{1}{3}, \quad z = \frac{3}{2}. \quad [KPZ] \quad (8.20)$$

However, for dimensions larger than one, ($d > 1$) there is no a precise analytical solution, but the results of calculated simulations are available.

8.3.4 Diffusive growth

We have studied various deposition models in previous sections. In RDSR, particles 'search' for the lowest height position. In BD particles stick to the first point on the surface with which they come in contact. In contrast to these processes, in diffusive growth model, the deposited particles diffuse on the surface, searching for the energetically most favorable position. The diffusion length can be quite large, and depends on the temperature and binding energies (Sec. 8.1.2).

In order to include the surface diffusion in the growth equation, the simplest scenario is considered: particles are deposited on a surface, whereupon they diffuse. The goal is to find a continuum equation that describes the variations in the interface height $h(\mathbf{r}, t)$ in the following form

$$\frac{\partial h}{\partial t} = F(h, \mathbf{r}, t). \quad (8.21)$$

Surface diffusion implies that the deposited particles generate a macroscopic current $j(\mathbf{r}, t)$, which is a vector parallel to the average surface direction. By neglecting the desorption, the diffusing particles can never leave the surface. Thus the local changes in the surface height are the result of the nonzero currents along the surface. Since the total number of particles remains unchanged during the diffusion process, the current must obey the continuity equation

$$\frac{\partial h}{\partial t} = -\nabla \cdot j(\mathbf{r}, t). \quad (8.22)$$

The surface current is driven by the differences in the local chemical potential $\mu(\mathbf{r}, t)$

$$j(\mathbf{r}, t) \propto -\nabla \mu(\mathbf{r}, t). \quad (8.23)$$

Surface diffusion is an activated process. The motion of an atom does not depend on the local height of the interface, but only on the number of bonds that must be broken for diffusion to take place. The number of bonds that a particle may form increases with the local curvature of the interface at that position. As it is shown in Fig. 8.12, if the local radius of curvature R is positive, the particle has a large number of neighbors, and moving away from the site will be difficult. In contrast, if R is negative, the atom has a few neighbors, and is able to diffuse easily. The simplest assumption is that the chemical potential controlling the diffusion probability is proportional to $-1/R$, which in turn is proportional to $\nabla^2 h(\mathbf{r}, t)$. Hence, the chemical potential can be written as

$$\mu(\mathbf{r}, t) \propto -\nabla^2 h(\mathbf{r}, t). \quad (8.24)$$

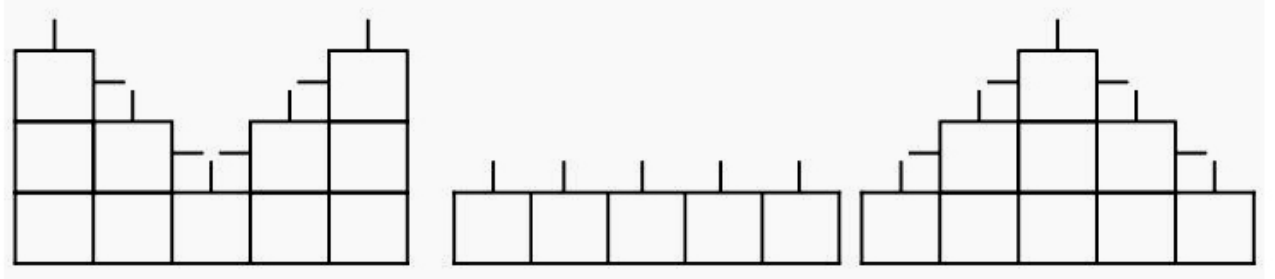


Figure 8.12: Schematic illustration of the three possible local geometries on the surface according to the number of bonds with the neighboring particles.

Hence, the equation describing the surface diffusion has the form

$$\frac{\partial h}{\partial t} = a_3 \nabla^4 h(\mathbf{r}, t) + \eta(\mathbf{r}, t). \quad (8.25)$$

where a_3 is negative. The growth Eq. 8.25 is a stochastic differential equation, similar to the EW equation. The difference comes in the linear term in the EW equation, $a_1 \nabla^2$, while in Eq. 8.25 there is $a_3 \nabla^4 h$ with $a_3 < 0$. This difference affects the value of the scaling exponents. From the Eq.8.25, the scaling exponents are determined as

$$\alpha = \frac{4-d}{2}, \quad \beta = \frac{4-d}{8}, \quad z = 4. \quad (8.26)$$

8.3.5 Raible's model for amorphous growth

Till now, we have presented different models for describing growth mechanisms. Although all these models have their differences, they are similar in the sense that they all provide a description of the growth process which describes the dynamics and morphology of an interface at large scales (larger than the typical interatomic distance) and for large times (after the deposition of several monolayers). Here, we want to present a more general model for the evolution of the surface morphology of amorphous thin films in the presence of potential density variations. This model has been initially suggested by Raible *et. al.* to explain the formation of moundlike surface structure of amorphous thin films on a mesoscopic length scale. [98], [95], [99] Figure 8.13 shows a sketch of an amorphous film on a substrate. The generalized Raible model consists of all the different contributions of the previous models, considering the intra-particle attractions and density inhomogeneities, in the following form

$$\frac{\partial h}{\partial t} = a_1 \nabla^2 h + a_2 (\nabla h)^2 + a_3 \nabla^4 h + a_4 \nabla^2 (\nabla h)^2 + \eta(\mathbf{r}, t). \quad (8.27)$$

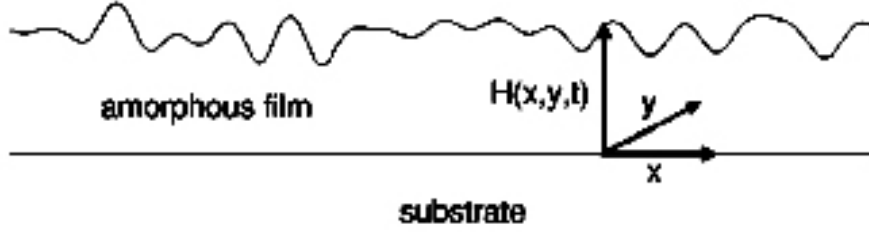


Figure 8.13: Sketch of amorphous film on a substrate.

The first term on the rhs of Eq. 8.27 is related to the deflection of the initially perpendicular incident particles caused by inter-particle attraction. When the particles are close to the surface, their trajectories are bent towards the surface. As a consequence, more particles arrive at places with $\nabla^2 < 0$ than at places with $\nabla^2 > 0$. In a simplified model, this deflection (in a direction perpendicular to the surface) happens instantaneously when a particle arrives at a distance b from the surface, as shown in the upper part of Fig. 8.14. Distance b characterizes the typical range of interparticle forces. A detailed mathematical analysis of this simplified model yields the explicit relation $a_1 = -Fb$, where F is the deposition rate. [98] The negative coefficient $a_1 < 0$ represents the growth instability (Sec. 8.3.2) that results for the growth of top-hills.

The second term is the nonlinear term of Eq. 8.27, the same as discussed in Sec. 8.3.3. It is responsible for the increase of the height of the interface by adding more 'material' to the sides of the hills. This term is related to the density variation.

The third term on the rhs of Eq. 8.27 represents the surface diffusion suggested in Sec. 8.3.4. The particles arrive at the surface, diffuse there and relax at surface sites that offer a sufficiently strong binding. Because these binding places are mainly areas on a surface with positive curvature $\nabla^2 h$, the surface diffusion results in a current of the form $j \propto \nabla(\nabla^2 h)$, as shown in the middle part of Fig. 8.14. This surface current adds the term $-\nabla \cdot j \propto -\nabla^4 h$ to the growth equation. Therefore, the sign of a_3 is negative.

The fourth term on the rhs of Eq. 8.27 is related to the equilibration of the inhomogeneous concentration of the diffusing particles on the surface. If only the just deposited particles diffuse before their relaxation, their surface concentration is weighted by the surface inclination, as shown in lower part of Fig. 8.14.

This model may exhibit different values of scaling exponents depending on which systems of molecules or atoms are studied.

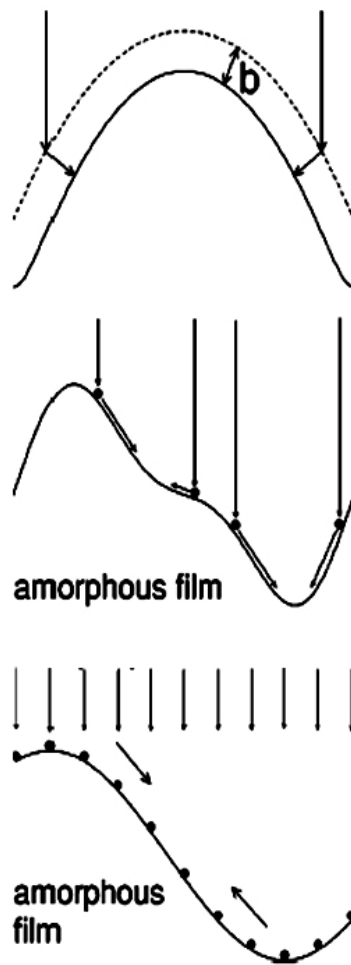


Figure 8.14: Microscopic effects of amorphous thin film growth. Upper part: Deflection of the particles due to the inter-particle forces. Middle part: Surface diffusion of deposited particles to places with larger curvature. Lower part: Equilibration of the inhomogeneous particle concentration due to the inhomogeneous particle concentration due to the geometry of the surface.

8.4 Quantifying deterministic and random influences on the surface morphology

In Sec. 8.2 some of the important quantitative parameters of the surface morphology have been introduced. Later, in Sec. 8.3, different growth models have been explained. These models provide a quantitative description of height evolution during growth time. In this section, the method which provide complete analysis on morphology of a surface at a specific time ($t = \text{const.}$) will be introduced. This method, proposed by the group of Rahimi Tabar, provide the general equation which governs surface morphology and height

8.4 Quantifying deterministic and random influences on the surface morphology¹¹³

fluctuations, $h(r)$, as a function of r at $t = \text{const.}$ [100], [101] As it has been shown, in addition to being highly accurate, the method is quite general and it is capable of providing a rational explanation for complex features of the surface morphology, without requiring scaling feature. [102], [103]

In the following the steps that lead to the development of a stochastic equation, based on the (stochastic) height fluctuations, is described.

8.4.1 The Markov nature of height fluctuations

As the first step we check whether the data follow a Markov chain and, if so, estimate the Markov length scale l_M . As is well-known, a given process with a degree of randomness or stochasticity may have a finite or an infinite Markov length scale. The Markov length scale is the minimum interval over which the data can be considered as a Markov process (a process without memory). [104], [103], [105] To determine the Markov scale l_M , we note that a complete characterization of the statistical properties of the height fluctuation requires the evaluation of joint probability density functions (PDFs), $P(h_1, r_1; \dots; h_N, r_N)$ for any arbitrary N . If the process is a Markov process (a process without memory), an important simplification arises. For this type of process the N -point joint PDF, P_N , is generated by a product of the conditional probabilities $P(h_{i+1}, r_{i+1} | h_i, r_i)$ for $i = 1, \dots, N-1$. As a necessary condition for being a Markov process, the Chapman-Kolmogorov (CK) equation, [106]

$$P(h_2, r_2 | h_1, r_1) = \int dr_3 P(h_2, r_2 | h_3, r_3) P(h_3, r_3 | h_1, r_1), \quad (8.28)$$

should hold for any value of $r_2 < r_3 < r_1$. One should check the validity of CK equation for different r_1 by comparing the directly-evaluated conditional probability distributions $P(h_2, r_2 | h_1, r_1)$ with the ones calculated according to right side of Eq. 8.28. The simplest way to determine l_M for stationary or homogeneous data is the numerical calculation of the quantity, $S = |P(h_2, r_2 | h_1, r_1) - \int dr_3 P(h_2, r_2 | h_3, r_3) P(h_3, r_3 | h_1, r_1)|$, for given h_1 and h_2 , in terms of, for example, $r_3 - r_1$ and considering the possible errors in estimating S . Then, Markov length is $l_M = r_3 - r_1$ for that value of $r_3 - r_1$ for which S vanishes or is nearly zero (achieves a minimum).

8.4.2 Governing equation of height fluctuations

Deriving an effective stochastic equation that describes the fluctuations of the quantity $h(r)$ constitutes the second step. The CK equation yields an evolution equation for the change of the distribution function $P(h, r)$ across the scales x . The CK equation, when formulated in differential form, yields a master equation which takes the form of a Fokker-Planck equation:

$$\frac{d}{dr}P(h,r) = \left[-\frac{\partial}{\partial h}D^{(1)}(h,r) + \frac{\partial^2}{\partial h^2}D^{(2)}(h,r) \right] P(h,r). \quad (8.29)$$

Kramers-Moyal coefficients of $D^{(1)}(h,r)$ and $D^{(2)}(h,r)$ are estimated directly from the data using the following equation:

$$D^{(k)}(h,r) = \frac{1}{k!} \lim_{\Delta r \rightarrow 0} \frac{1}{\Delta r} \left\langle [h(r + \Delta r) - h(r)]^k \right\rangle |_{h(r)=h} \quad (8.30)$$

We note that this Fokker-Planck equation is equivalent to the following Langevin equation [100]:

$$\frac{d}{dr}h(r) = D^{(1)}(h,r) + \sqrt{D^{(2)}(h,r)}f(r), \quad (8.31)$$

where $f(r)$ is a random force with zero mean and Gaussian statistics, δ -correlated in r , i.e., $\langle f(r)f(r') \rangle = 2\delta(r - r')$. It turns out the resulting deterministic and random part coefficients, directly estimated from the morphology data, are linear and quadratic functions of h , respectively.

Furthermore, with this last expression (Eq. 8.31), it becomes clear that we are able to separate the deterministic and the noisy components of the surface height fluctuations in terms of the coefficients $D^{(1)}$ and $D^{(2)}$. Equation 8.31 enables us to regenerate rough surfaces which are similar to the original one (in the statistical sense).

9 Growth and morphology of α -NPD amorphous thin films

In order to tailor and modify thin film properties to be suitable for desired applications, e.g. organic light emitting devices (OLED) in this case, it is necessary to study and understand the influence of deposition parameters on thin film growth. The chosen material is N,N'-diphenyl-N,N'-bis(1-naphthyl)-1-1'-biphenyl-4,4''diamine (α -NPD) processed by organic vapor-phase deposition (OVPD). Film growth in OVPD is controlled by three independent parameters which are deposition rate, substrate temperature and chamber pressure. Our study is focused on the influence of deposition rate and substrate temperature on film morphology. A remarkable dependence of the film morphology upon deposition rate and substrate temperature is observed. A detailed quantitative morphology analysis provides excellent description of the growth mechanism of OLED films. [107]

9.1 Introduction

During the past decade, enormous progress has been made in growing ultrathin organic films and multilayer structures with a wide range of exciting optoelectronic properties. [41], [63] One of the most advanced applications of molecular organic materials are light-emitting diodes (OLEDs). These devices have a multilayer structure and consist of several thin films of organic materials. For a better understanding and design of such devices, it is necessary to know and understand the morphology, structure and growth modes of the organic films. Therefore, to tailor and control the surface morphology, understanding of the influence of deposition parameters on the organic film growth mechanism is very important.

In this work, we perform a systematic study on morphology and growth of amorphous organic thin films of α -NPD (N,N'-diphenyl-N,N'-bis(1-naphthyl)-1-1'-biphenyl-4,4''diamine). These thin films are deposited by Organic Vapor Phase Deposition, OVPD (Sec. 6.1). By controlling the deposition rate, substrate temperature and reactor chamber pressure, the film growth can be modified in OVPD which in turn, strongly affects the device performance. [63], [108] In this chapter, our investigation is focused on the influence of deposition rate and substrate temperature on the morphology of organic thin films. For this purpose, the surface morphology was measured by Atomic Force Microscopy (AFM). A remarkable dependence of the film morphology upon deposition rate and substrate

temperature has been observed. Performing a detailed analysis of surface morphology as well as investigating the initial growth stage an in-depth description of the film growth has been enabled.

9.2 Experiments

α -NPD thin films have been deposited on top of silicon substrates using (OVPD). The silicon substrate is covered with a thin layer (~ 2 nm) of native silicon dioxide. The roughness of the silicon substrate is 0.40 nm, measured by AFM. The deposition technique is OVPD (Sec. 6.1). At the constant reactor chamber pressure, series of α -NPD films have been deposited with different deposition rates and substrate temperatures. The expected film thickness is around 50 nm for all samples. The deposition rate, R , was varied between 2 Å/s and 17 Å/s. The substrate temperature (T), was set to temperatures of 5°C, 25°C, 45°C and 65°C, respectively.

In order to investigate the initial stage of the growth, ultra-thin samples have been deposited at both the highest and the lowest substrate temperatures, i.e. 65°C and 5°C. The thickness of these ultra thin samples are about 2-3 nm and their deposition rate was kept at the lower range between 2 Å/s and 4 Å/s.

For each sample, at least three AFM scans at three different positions on the surface have been performed. The AFM images and their corresponding quantitative information are shown in the following sections.

9.3 Results and discussions

AFM images for different deposition rates and substrate temperatures are shown in Fig. 9.1. This matrix of AFM images depicts a clear trend for the morphology of the films at different deposition rates and substrate temperatures. As can be seen from Fig. 9.1, the films have a rough morphology at the two off-diagonal corners of this AFM matrix. These two corners represent the one deposited at low substrate temperature (5°C) with the high deposition rate (17 Å/s) and the other one deposited at high substrate temperature (65°C) with the low deposition rate (2 Å/s). However, films are relatively smooth around the main diagonal which consists of the samples with the low deposition rate at 5°C, the intermediate deposition rate at 25°C and 45°C, and the high deposition rate at 65°C.

9.3.1 Quantitative analysis

To derive quantitative information of the surface morphology, as the first quantity, the corresponding rms-roughness (Sec. 8.2) has been extracted from the AFM images of each

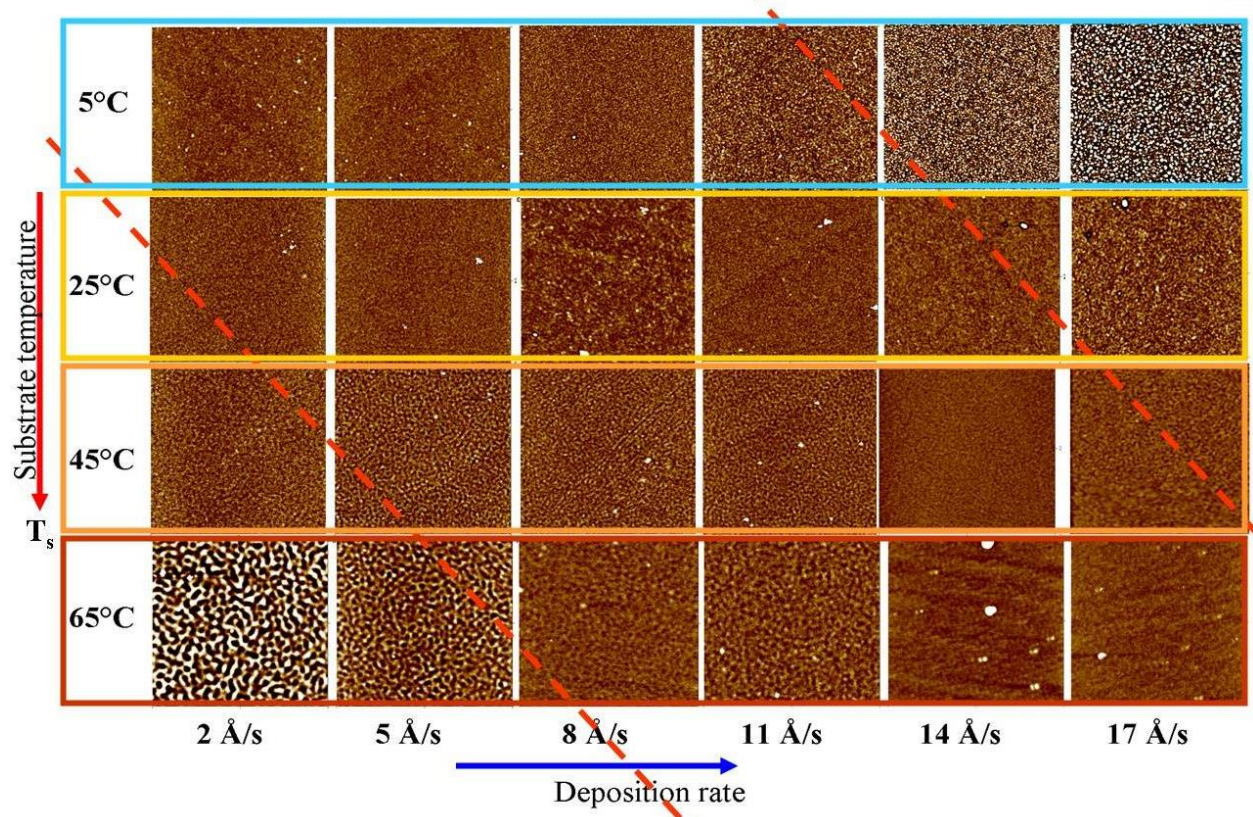


Figure 9.1: AFM images of α -NPD films on Si-substrate deposited by OVPD for different deposition rates and substrate temperatures. In this matrix the deposition rate varies from 2 Å/s to 17 Å/s, and the substrate temperature varies from 5°C to 65 °C. The AFM scan is $5\mu\text{m} \times 5\mu\text{m}$ and the color height scale corresponds to 5 nm. At the two off-diagonal corners, the films have a rough morphology.

sample. Figure 9.2 shows the rms-roughness as a function of deposition rate at different substrate temperatures. At low substrate temperature (5°C), the rms-roughness increases with deposition rate. On the contrary, for the highest substrate temperature (65°C), the films become smoother with increasing deposition rate. At the two moderate substrate temperatures (25°C and 45°C) films are relatively smooth and there are rather small changes in rms-roughness upon increasing deposition rate. Hence the rms-roughness is clearly effected by the substrate temperature (Fig. 9.2).

Furthermore, the roughness exponent α (Sec. 8.2.3) of all samples has been calculated. The result of these calculations is shown in Fig. 9.3. The scaling exponent α is clearly different at different substrate temperatures, however, it has the same trend for different deposition rates. It should be noted that, a large α is consistent with the picture that the surface diffusion generates a rough surface, at large length scales. [92]

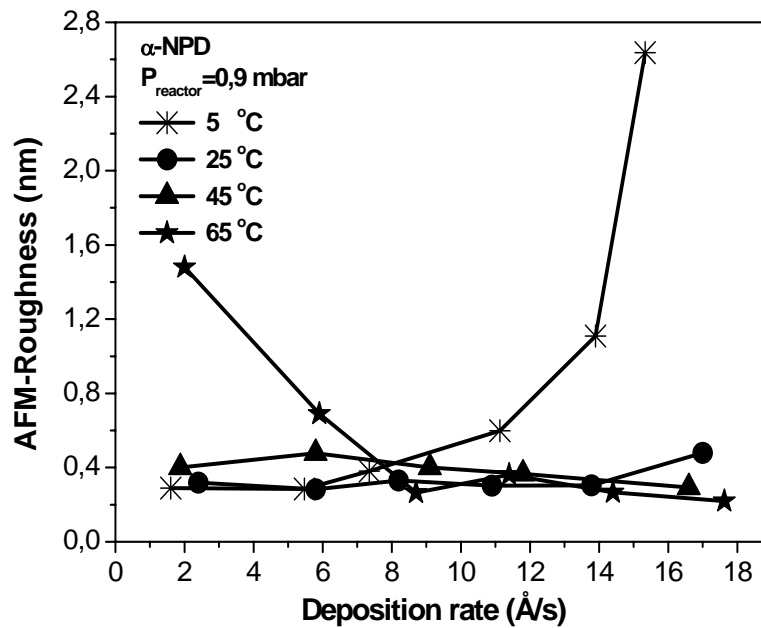


Figure 9.2: Rms-roughness as a function of deposition rate at different substrate temperature. Both the samples deposited at low substrate temperature (5°C) and the highest rates (14 Å/s and 17 Å/s) and the films deposited at the highest temperature (65°C) and low deposition rate (2 Å/s) show a high rms-roughness.

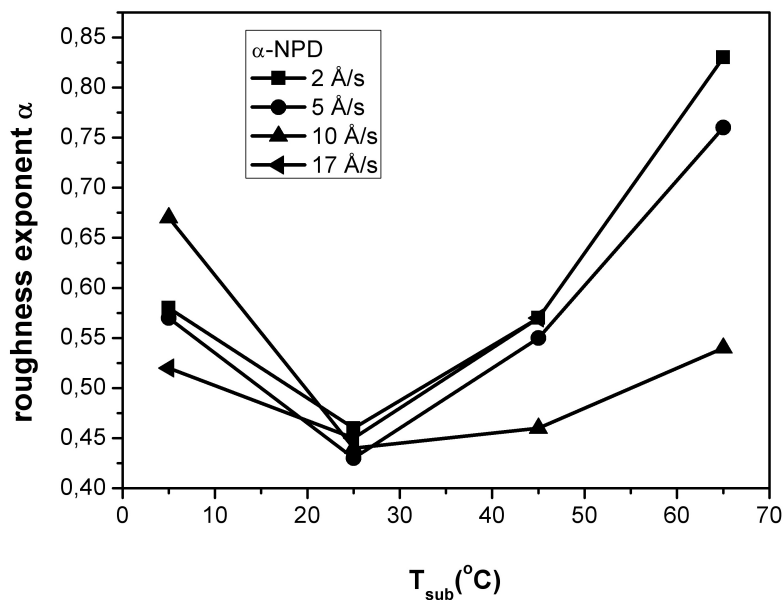


Figure 9.3: Roughness exponent α as function of substrate temperature.

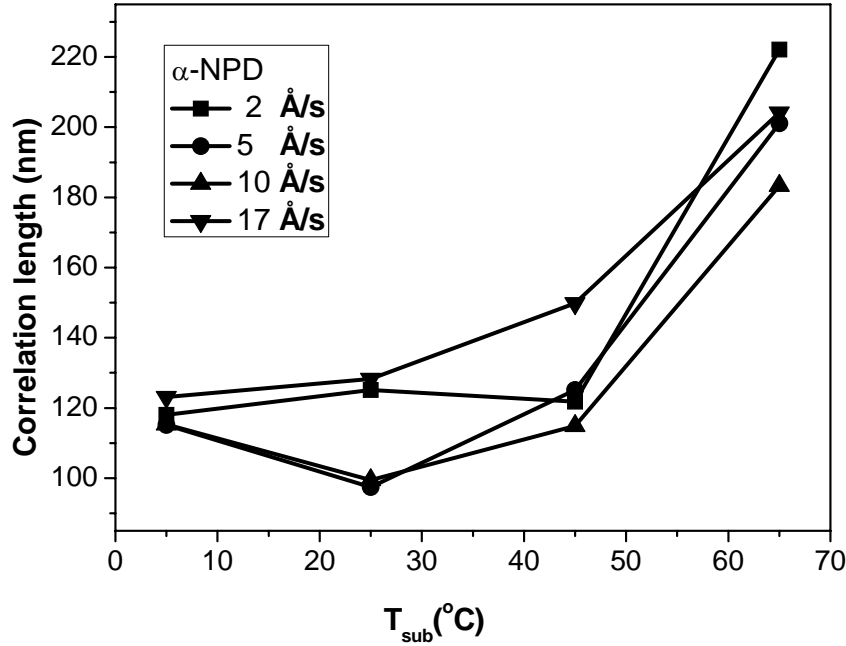


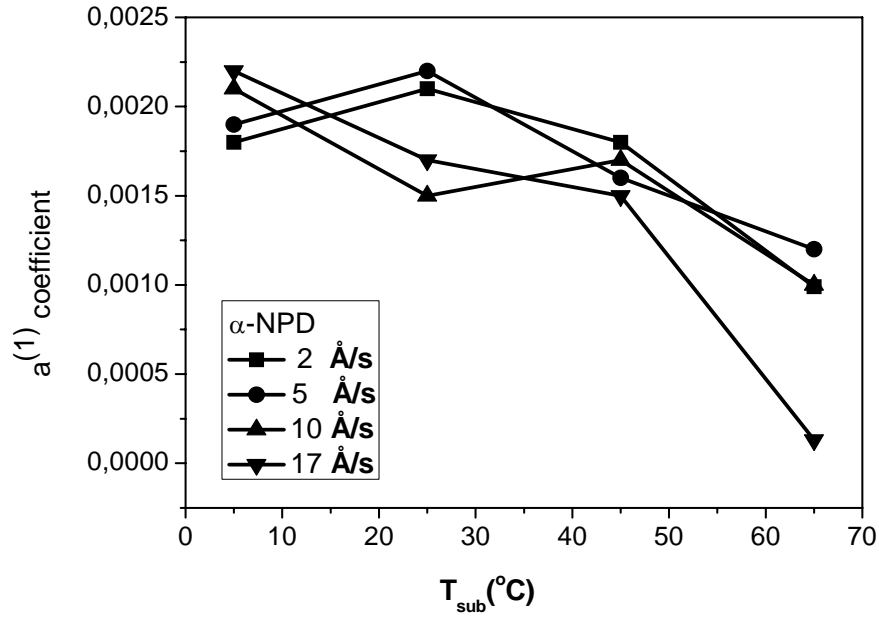
Figure 9.4: Correlation length as a function of substrate temperature for different deposition rates. The largest correlation length is observed at the highest temperature of 65°C.

In order to quantify the lateral structure size on the surface, the lateral correlation length (Sec. 8.2.2) has been calculated. Figure 9.4 displays the calculated correlation length for different substrate temperatures and deposition rates. This plot shows a clear increase of the correlation length with substrate temperature.

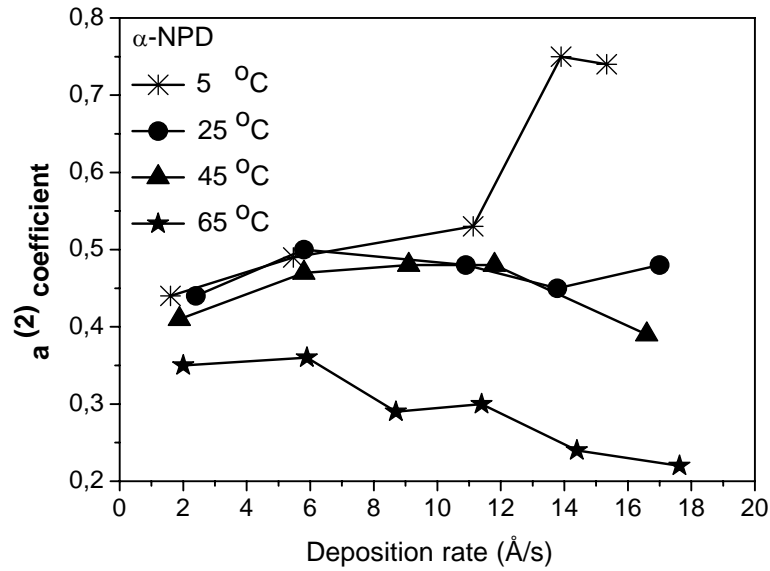
The trends of rms-roughness, roughness exponent and correlation length depict a strong effect of the substrate temperature. One can see that, at the low substrate temperature (5°C), due to lower diffusion possibility, films become rough with deposition rate, and they are smooth only at low deposition rates (2 $\text{\AA}/\text{s}$ -10 $\text{\AA}/\text{s}$). At high substrate temperature (65°C), surface diffusion is playing a more important role to make larger structures on the surface, which indeed increases the lateral correlation length and rms-roughness of the films respectively.

In order to achieve a complete characterization of the surface morphology and to construct the governing equation of the height fluctuation, a series of calculations have been done, based on the model proposed in Sec. 8.4. In the first step, the Markov length scale, l_M has been estimated for each sample. The result of these calculations are demonstrated in Table 9.1

The next step is to calculate the deterministic and the random noise coefficients of $D^{(1)}(h,r)$ and $D^{(2)}(h,r)$ directly from the data, using Eq. 8.30. These two coefficients are linear and quadratic functions of h , respectively, and are well-presented as the approximations,



(a) Deterministic coefficient ($A^{(1)}$) as a function of substrate temperature calculated from AFM images for different deposition rates. There is an obvious decrease of this coefficient with substrate temperature.



(b) Random noise coefficient ($A^{(2)}$) as a function of deposition rate for different substrate temperature calculated from AFM images of α -NPD samples. At low substrate temperature increasing deposition rate rises these fluctuations. However, for the highest temperature the contrary effect is observed.

Figure 9.5: Determined deterministic coefficient ($A^{(1)}$), and Random noise coefficient ($A^{(2)}$) for α -NPD samples with different deposition rates and substrate temperature.

$$D^{(1)}(h) = -A^{(1)}h, \quad D^{(2)}(h) = A^{(2)} - B^{(2)}h + C^{(2)}h^2 \quad (9.1)$$

In order to estimate the coefficients $A^{(1)}, A^{(2)}, B^{(2)}$ and $C^{(2)}$, the functions $D^{(1)}(h, r)$ and $D^{(2)}(h, r)$ vs. h need to be fitted by a linear and quadratic function of h , respectively. As well as morphology, coefficients $D^{(1)}$ and $D^{(2)}$ are also dependent on deposition parameters, substrate temperature, T , and deposition rate, R . Hence, $D^{(1)}, D^{(2)}$ and their consisting terms have been calculated for all samples with different deposition parameters. The corresponding results for these coefficients are demonstrated in Table 9.1. In Fig.9.5(a), the $A^{(1)}$ coefficient of the deterministic term $D^{(1)}$, is plotted as a function of substrate temperature for different deposition rates. This term shows an obvious decrease upon the increase of temperature and demonstrates an inverse trend as the correlation length in Fig. 9.4.

sample	l_M (nm)	$A^{(1)}$	$A^{(2)}$	$B^{(2)}$	$C^{(2)}$
$T_{sub} = 5^\circ C$					
$Rate = 2\text{\AA}/s$	39.08	0.0018	0.44	0.0037	7.81×10^{-6}
$Rate = 5\text{\AA}/s$	39.08	0.0019	0.49	0.0041	8.80×10^{-6}
$Rate = 10\text{\AA}/s$	29.31	0.0021	0.53	0.0042	9.43×10^{-6}
$Rate = 14\text{\AA}/s$	29.31	0.0024	0.75	0.0050	10.80×10^{-6}
$Rate = 17\text{\AA}/s$	39.04	0.0022	0.74	0.0044	12.50×10^{-6}
$T_{sub} = 25^\circ C$					
$Rate = 2\text{\AA}/s$	29.31	0.0021	0.44	0.0039	9.20×10^{-6}
$Rate = 5\text{\AA}/s$	29.31	0.0022	0.50	0.0047	9.19×10^{-6}
$Rate = 10\text{\AA}/s$	48.85	0.0015	0.48	0.0040	8.73×10^{-6}
$Rate = 14\text{\AA}/s$	48.85	0.0017	0.45	0.0038	8.39×10^{-6}
$Rate = 17\text{\AA}/s$	48.85	0.0017	0.48	0.0039	8.12×10^{-6}
$T_{sub} = 45^\circ C$					
$Rate = 2\text{\AA}/s$	39.08	0.0018	0.41	0.032	6.86×10^{-6}
$Rate = 5\text{\AA}/s$	68.39	0.0016	0.47	0.0039	8.57×10^{-6}
$Rate = 10\text{\AA}/s$	58.62	0.0017	0.48	.0040	8.64×10^{-6}
$Rate = 14\text{\AA}/s$	-	-	-	-	-
$Rate = 17\text{\AA}/s$	58.62	0.0015	0.39	0.0034	7.62×10^{-6}
$T_{sub} = 65^\circ C$					
$Rate = 2\text{\AA}/s$	87.93	0.0018	0.35	0.0020	4.72×10^{-6}
$Rate = 5\text{\AA}/s$	87.93	0.0019	0.36	0.0029	6.17×10^{-6}
$Rate = 10\text{\AA}/s$	87.93	0.0021	0.30	0.0025	5.43×10^{-6}
$Rate = 14\text{\AA}/s$	48.85	0.0024	0.24	0.0024	5.12×10^{-6}
$Rate = 17\text{\AA}/s$	39.08	0.0022	0.22	0.0018	3.96×10^{-6}

Table 9.1: Markov length scale (l_M), deterministic coefficient ($A^{(1)}$) and random noise coefficients ($A^{(2)}, B^{(2)}, C^{(2)}$) for all samples at different substrate temperature and deposition rate.

The second term in the Eq. 8.30 for the height fluctuation is $D^{(2)}$, the coefficient of random noise which has a quadratic form as seen from Eq. 9.1. According to our calculations (Table 9.1), the first and second order terms of this quadratic equation are very small. Hence, the constant part, $A^{(2)}$, is considered as the representative quantity for $D^{(2)}$. Figure 9.5(b) shows $D^{(2)}$ as a function of deposition rate for different substrate temperatures. The trend observed is different at various substrate temperatures. At 5°C, an increasing deposition rate yields an increase of the random noise term. However, at 65°C, the random coefficient decreases upon rising rate. Furthermore, at a constant deposition rate, by increasing the temperature $D^{(2)}$ decreases. Hence, from this observation, we infer that the more efficient surface diffusion the smaller the resulting surface randomness.

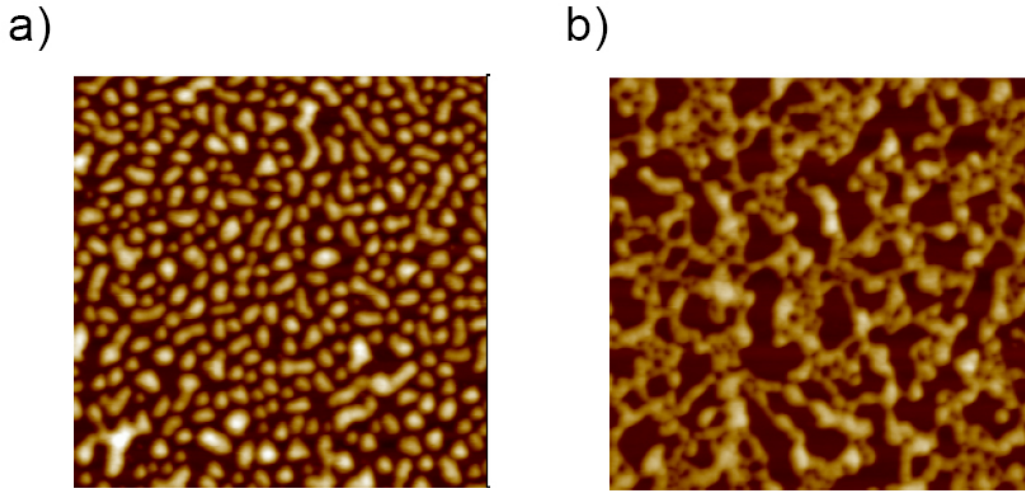


Figure 9.6: AFM images of ultra thin films (3-4 nm) of α -NPD. (a) with the deposition rate of 2 Å/s at the highest substrate temperature (65°C). (b) with the deposition rate of 4 Å/s at the lowest substrate temperature (5°C). Increasing the substrate temperature increased surface diffusion of molecules and this leads to more molecular agglomeration. The color height scale is 20 nm for both images. The image size is $2.5\mu m \times 2.5\mu m$.

9.3.2 Initial stages of growth

In order to confirm the effect of diffusion in the growth of α -NPD samples, the morphology at the initial stages of growth has been investigated. For this purpose, two ultra thin samples were deposited at both the highest and the lowest substrate temperatures, i.e. 65°C and 5°C.

The AFM images of these samples (Fig. 9.6) show that for the sample deposited at 65°C (Fig. 9.6(a)) molecules tend to rather agglomerate together than to the substrate. However, at the substrate temperature of 5°C (Fig. 9.6(b)) molecules spread over the substrate. This is due to the fact that at the highest substrate temperature of 65°C

molecules surface diffusion is more favorable; hence, they can travel easily on the substrate and coexist to form separate islands. In this case, it is more energetically favorable for molecules to stick together than to wet the substrate. However, at the lowest substrate temperature of 5°C, the diffusion process is less probable, hence, molecules prefer to stick at the positions nearby the area at the time of arrival and spread over the surface. Hence, Fig. 9.6 shows a clear effect of surface diffusion in the initial stage of the growth, which has been additionally confirmed by further annealing of the sample Fig. 9.6(a) up to 100°C for 10 min. The AFM image of the annealed sample is displayed in Fig. 9.7. One can see that the size of the initial islands has been increased upon annealing. This is due to further diffusion of molecules on the surface which yields larger agglomerated islands.

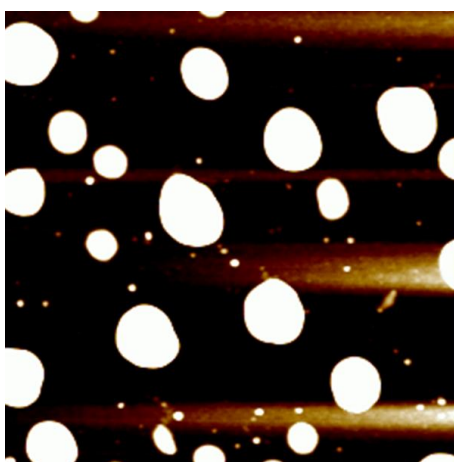


Figure 9.7: AFM image of the annealed sample of Fig. 9.6(a) up to 100°C. The color height scale is 20 nm and the image size is $2.5\mu m \times 2.5\mu m$.

9.4 Conclusion and outlook

Considering both the detailed characterization of the full coverage films (with thickness ~ 50 nm) and the investigation of the initial growth stages, makes it possible to explain the growth of α -NPD films. A clear change in the calculated critical exponents α vs. substrate temperatures (Fig. 9.3) indicates that there can be different modes which govern the growth of α -NPD films at different substrate temperatures. At the two extreme temperatures, 5°C and 65°C, rms-roughness values vs. deposition rate, depicts quite reverse trends. At the lowest temperature of 5°C we have observed the increase of rms-roughness with deposition rate, while at 65°C films become smoother with deposition rate. These results indicate that surface diffusion and random fluctuations govern the film growth mechanism.

Taking into account the initial growth stages Fig. 9.6(a), at high substrate temperature, due to high surface diffusion, there is distinct island formation. This, in turn, increases the

correlation length and surface roughness for the thicker films. However, at high temperature, increasing deposition rate, decreases diffusion time for each molecule. According to the non-wetting growth model, [88] this raises the number of islands but reduces islands size, which leads to smoother surface morphology at high coverage. Therefore, we can make the statement that the growth model at high substrate temperature is similar to the one for metal on metal growth.

On the other hand, at 5°C, surface diffusion is less important (Fig. 9.6(a)) and molecules are adsorbing on the surface in more spread. At this temperature, surface roughness increases with deposition rate. This observation can be explained considering the growth model of Raible *et.al.* As mentioned in Sec. 8.3.5, in case of negligible diffusion coefficients, there is a pronounced tendency for the molecules to go on the top-hills rather than valleys. Since the corresponding coefficient $a_1 = -Fb$ of Eq. 8.27 is proportional to deposition rate. Hence, film instabilities and morphology random fluctuations increases with deposition rate.

However, at two moderate temperatures of 25°C and 45°C, there is a compromise between deposition rate and diffusion process. For these samples, the substrate temperature is insufficient for molecular agglomeration; contrastingly, it is a driving force for smoothening of the surface. These moderate temperatures can be considered as the optimum substrate temperature for producing smooth films at different deposition rate in the production lines.

Furthermore, besides deposition rate and substrate temperature, film growth in OVPD is controlled by the third independent parameter which is chamber pressure. Hence, the aim of our further study is to investigate the influence of OVPD chamber pressure on surface morphology of organic thin films. [109]

10 Summary and outlook

Molecular organic compounds are employed as active materials in a variety of applications, including organic light emitting diodes (OLEDs) and organic thin film transistors (OTFTs). These devices consisting of sequentially deposited layers of organic materials have been demonstrated with active device thicknesses of only a few hundred nanometers or less. For a better understanding and design of such devices, it is necessary to understand the structural and optical properties of the organic thin films employed.

In this work, the structural and optical properties of organic thin films have been investigated. Our investigation is focused on the two types of organic materials, crystalline and amorphous. For several applications including electronic devices such as transistors, the highest possible electron mobilities are required. This property is only found in the films with ultimate structural order and crystalline properties. For other applications such as light emitting devices, the highest possible quantum yield is most important. This yield depends upon the probability of radiative electron-hole recombination which is highest for amorphous materials where the electron and hole mobilities are low.

Oligomers based on the family of five-membered thiophene conjugated ring and its derivate, due to their self-assembling nature, have been considered as one of the most common conducting organic oligomers used in OTFT devices. We have studied the single molecules of 3-nitrothiophene/selenophen/tellurophen and the adsorption of these molecules on Cu(110) surface, utilising *ab initio* calculations. These calculations provide a basic understanding and forecasting of intra- and inter-molecular interactions present in the observed structures. Our results for single molecules shows that in the gas phase molecules have a planar geometry. The comparison of the different conjugated rings (thiophene/selenophen/tellurophen) indicates that by increasing the atomic radius, from sulfur to selenium and tellurium atoms, the C-S/Se/Te bond length increases while the angle between these bond decreases. According to these results, the C-S bond in the thiophene ring has the smallest length and the C-S-C angle has the largest value.

Adsorption of the molecules on the surface breaks the planarity of single molecules. Monolayers of 3-nitrothiophene/selenophen/tellurophen on a Cu(110) surface are well ordered with the aromatic ring perpendicular to the surface, in a close packed structure. Due to the strong lateral interaction between the hydrogen atoms of the neighboring conjugated rings, they rotate relative to the nitro ($-NO_2$) group. The optimum rotation angles are obtained as 23° (for thiophene ring) to 25° (for selenophen ring) and 26° (for tellurophen ring). The optimization calculations show that the total energy of the rings consisting of larger atoms (selenium, tellurium) is more sensitive to the rotation angle of the ring.

Based on these results, it is possible to optimize geometry and structure of many other interesting π -conjugated molecules. The most straight forward calculations can be done for the molecules with similar conjugated rings such as longer chain of thiophene derivatives which are widely being used as self assembled monolayers (SAM). Furthermore, it will be interesting to investigate the adsorption of the different types of π -conjugated organic molecules on the surface, such as the ones containing benzene ring in their structures. Perylene and Pentacene are the two examples of such molecules which have been experimentally investigated as well, at our institute, I. Physikalisches Institut, Physik neuer Materialien (IA), RWTH-Aachen. [110]

As the next type the organic materials, amorphous ones, tris-(8-hydroxyquinoline) aluminum (Alq_3) and N,N'-diphenyl-N,N'-bis(1-naphthyl)-1-1'-biphenyl-4,4''diamine (α -NPD) have been investigated. These molecules are among the most commonly used electron-transport and hole-transport materials suitable for OLED applications. The optical and structural properties of the thin films of these materials deposited by organic vapor phase deposition (OVPD) have been studied by spectroscopic ellipsometry (SE). Employing this technique enables the precise determination of the dielectric function as well as thickness of the organic thin films of each material. This result can be explained by the characteristic features of electronic states in organic molecules. The dielectric function of Alq_3 and α -NPD films have been determined in the spectral range of 0.7 eV to 5.0 eV by spectroscopic ellipsometry. The optical constants of these samples were determined using the normal harmonic oscillator and the generalized Kim model with Gaussian broadening. AFM and XRR measurements have been performed for the independent determination of film structure. Employing the Kim oscillator model, the quality of the fit has been improved on average by the factor of 4. Furthermore, using the Kim model the film thickness is reproduced to within 1% accuracy. Moreover, we have shown that by using the generalized Kim model, we can obtain a single dielectric function for all samples of the same material. This is in line with the constant film density values determined by XRR. The superior quality of the fits employing the Kim model seems to be attributed to the better description of electron-phonon coupling in the organic materials.

In order to tailor and modify thin film properties to be suitable for desired applications, e.g. organic light emitting devices (OLED) in this case, it is necessary to study and understand the influence of deposition parameters on thin film growth. Our study is focused on the influence of deposition rate and substrate temperature on (α -NPD) film morphology and growth. The expected film thickness is around 50 nm for all samples. The deposition rate, R , was varied between 2 Å/s and 17 Å/s. The substrate temperature (T), was set to temperatures 5°C, 25°C, 45°C and 65°C, respectively. A remarkable dependence of the film morphology on deposition rate and substrate temperature is observed. A detailed quantitative morphology analysis provides an excellent description of the growth mechanism of OLED films. In order to investigate the initial stage of the growth, ultra thin samples have been deposited at both the highest and the lowest substrate temperatures, i.e. 65°C and 5°C. The thickness of these ultra thin samples are about 2-3 nm and their deposition rate was kept at the lower range between 2 Å/s and 4 Å/s.

Considering both of the detailed characterization analysis of the full coverage films (with thickness ~ 50 nm) and investigation of the initial growth stages, makes it possible to explain the growth of α -NPD films. At the two extreme temperatures, 5°C and 65°C, rms-roughness values vs. deposition rate, depict quite reverse trends. At the lowest temperature of 5°C we have observed the increase of rms-roughness with deposition rate, while at 65°C films become smoother with deposition rate. Also, at the moderate substrate temperatures (25°C and 65°C) films are relatively smooth and there are rather small changes in morphology upon deposition rate. A clear change in the calculated critical exponents α vs. substrate temperatures is observed. This indicates that there can be different modes which govern the growth of α -NPD films at different substrate temperatures. The obtained results are indicative for a clear effect of surface diffusion and random fluctuations on the film growth mechanism.

Taking into account the initial growth stages, at high substrate temperature, due to high surface diffusion, there is distinct island formation. This, in turn, increases the correlation length and surface roughness for the thicker films. However, at high temperature, increasing deposition rate, decreases the diffusion time for each molecule. According to the non-wetting growth model, this raises the number of islands but reduces islands size, which leads to smoother surface morphology after high coverage. Therefore, we can make an statement that the growth model at high substrate temperature is similar to the one for metal on metal growth. On the other hand, at 5°C, surface diffusion is less important and molecules are adsorbing on the surface in more spread. At this temperature, surface roughness increases with deposition rate. This observation can be explained considering the growth model of Raible. In case of negligible diffusion coefficients, there is a pronounced tendency for the molecules to go on the top-hills rather than valleys. Hence, film instabilities and random morphology fluctuations increase with deposition rate. However, at two moderate temperatures of 25°C and 45°C, there is a compromise between deposition rate and diffusion process. For these samples, the substrate temperature is insufficient for molecular agglomeration; contrastingly, it is a driving force for smoothening of the surface. These moderate temperatures can be considered as the optimum substrate temperature for producing smooth films at different deposition rate in the production lines.

Besides deposition rate and substrate temperature, which were considered in this thesis, film growth in OVPD is controlled by the third independent parameter which is chamber pressure. Chamber pressure is considered as the characteristic deposition parameter in OVPD in comparison with VTE (vacuum thermal evaporation) where we are in the vacuum regime. Hence, the aim of our further study is to investigate the influence of OVPD chamber pressure on surface morphology of organic thin films. [109]

In this work, we have studied film growth and morphology at two different range of film thicknesses, i.e. ~ 50 nm and ~ 2 -3 nm. Morphology evolution upon thickness variation between these two extremes is the next interesting subject we are investigating. This study

will provide more detailed information about growth mechanism versus film thickness. Furthermore, it will be possible to calculate the growth exponent β for such thin films.

It is highly desirable to study the correlation between surface morphology and device efficiency. In general, to obtain high efficiency of devices, suitable for OLEDs, both of amorphous and smooth films are mainly preferable; whereas, in some other applications, such as organic sensors, rough interfaces could be desired. This statement admit the existence of a correlation between roughness of the films and the device properties. Moreover, it arises the important challenging question that how this correlation could be specified. For this purpose, besides AFM and XRR (for structure and morphology characterization), photoluminescence, PL, and electrical measurements (for characterizing device efficiency) can be performed. Our goal is to carefully investigate the relation between PL and electrical measurements and the film morphology.

List of Figures

2.1	Schematic illustration of an all-electron and pseudoelectron valence wave-function and potentials.	15
3.1	Flowchart of the iterative procedure for the calculation of the electronic energy.	23
3.2	Loop-structure schemes in the EStCoMPP -program.	31
4.1	Schematic view of the 3-nitrothiophene/selenophen/tellurophen molecule. .	35
4.2	Schematic view of the optimized structures of single molecules in gas phase.	37
4.3	Schematic view of the high coverage adsorption of molecules on Cu(110) surface.	38
4.4	Energy (with respect to the minimum) vs. rotation angle	39
4.5	Ring rotation for the 'bridge' configuration.	41
4.6	Ring rotation for the 'top' configuration.	42
4.7	Side view of the adsorbed 3-nitrothiophene on Cu(110).	43
4.8	Side view of the adsorbed 3-nitroselenophen on Cu(110).	43
4.9	Side view of the adsorbed 3-nitrotellurophen on Cu(110).	44
5.1	Examples of an aromatic hydrocarbon and a conjugated polymer.	49
5.2	The benzene molecule (C_6H_6).	50
5.3	Schematic energy level diagram for HOMO and LUMO states.	51
5.4	The ground state S_0 , the first singlet state S_1 and the first triplet state T_1 .	52
5.5	Level energy diagram for the anthracene molecule.	52
5.6	Schematic diagram of the vibrational-electronic transitions in a molecule. .	59
5.7	Schematic representation of the absorption and emission in a two atoms molecule.	61
5.8	Energy level diagram of a simple diatomic molecule, as a function of the separation between the two nuclei.	62
5.9	Configuration diagram for two electronic states in a molecule.	63
5.10	The electron-phonon coupling constant for a series of organic molecules as a function of π -electrons number.	64
5.11	Schematic diagram of a free a tightly bound exciton.	66
5.12	Excitonic effect for a direct gap semiconductor.	68
5.13	Absorption spectrum of pyrene $C_{16}H_{10}$ single crystals at room temperature.	69
5.14	An example of monomer, dimer and polymer.	70

5.15	Chemical structure of two conjugated molecules.	71
5.16	Absorption and the photocurrent spectra of polydiacetylene (PDA) crystals.	72
6.1	OVPD® principle and quartz flow deposition module invented by Forrest. [64]	74
6.2	Schematic representation of the boundary layer in an LP-OVPD system with a horizontal substrate.	75
6.3	Atomic force microscope	76
6.4	$\theta/2\theta$ -Scan in XRR.	78
6.5	An example of XRR spectrum.	79
6.6	Schematic setup of an ellipsometry experiment.	80
6.7	Rotation of the polarization ellipsis upon reflection on a surface.	81
6.8	Rotation of the polarization ellipsis upon reflection on a surface.	82
7.1	AFM image of the Alq ₃ sample deposited with a rate of 14.0 Å/s.	86
7.2	XRR spectrum of Alq ₃ sample deposited with a rate of 14.0 Å/s.	87
7.3	The three-phase model (organic film/Si-oxide/Si).	88
7.4	Refractive index n and extinction coefficient k , obtained for the HO model of (a) Alq ₃ and (b) α – NPD samples.	89
7.5	Measured and simulated ellipsometry spectra, for an Alq ₃ sample employing the Kim model.	90
7.6	Refractive index n and extinction coefficient k , using the Kim model for Alq ₃ and α – NPD samples.	92
7.7	Comparison of film thicknesses determined using XRR vs. the film thickness.	93
8.1	The three growth mechanisms close to thermodynamic equilibrium.	96
8.2	Adsorption, (re-)desorption probabilities, diffusion, nucleation and island growth processes.	97
8.3	Schematic illustration of the lattice potential and its effect on diffusion process.	99
8.4	Height-height correlation function vs. length scale.	100
8.5	The scaling behavior of surface roughness.	101
8.6	The random deposition, RD, model.	103
8.7	Random deposition with surface relaxation (RDSR).	105
8.8	The smoothening effects of the Laplacian term $a_1 \nabla^2 h$ with $a_1 > 0$	106
8.9	The ballistic deposition model.	107
8.10	The lateral growth in the KPZ equation.	107
8.11	The effect of nonlinear term in KPZ.	108
8.12	Schematic illustration of the three possible local geometries on the surface according to the number of bonds with the neighboring particles.	110
8.13	Sketch of amorphous film on a substrate.	111
8.14	Microscopic effects of amorphous thin film growth.	112

9.1	The matrix of AFM images α -NPD films for different deposition rates and substrate temperatures.	117
9.2	Rms-roughness as a function of deposition rate at different substrate temperature.	118
9.3	Roughness exponent α as function of substrate temperature.	118
9.4	Correlation length as a function of substrate temperature for different deposition rates.	119
9.5	Determined deterministic coefficient ($A^{(1)}$), and Random noise coefficient ($A^{(2)}$).	120
9.6	AFM images of ultra thin films (3-4 nm) of α -NPD.	122
9.7	AFM image of the annealed sample of Fig. 9.6(a) up to 100° C.	123

List of Tables

4.1	The bond lengths in the conjugated ring and the nitro group for the optimized configurations of single molecules.	36
4.2	The angles in the conjugated ring and the nitro group for the optimized configurations of single molecules.	36
4.3	Optimum rotation angle for the thiophene, selenophen and tellurophen rings.	40
4.4	The angles in the conjugated ring and the nitro group for the optimized configurations of the adsorbed molecules of the adsorbed molecules.	41
4.5	The bonds in the conjugated ring and the nitro group for the optimized configurations of the adsorbed molecules.	45
4.6	Comparison of the two anchoring groups, nitro and carboxylate.	45
7.1	Generalized Kim model parameters for fitting SE spectra of Alq_3 thin film.	90
7.2	Generalized Kim model parameters for fitting SE spectra of α -NPD thin film.	91
7.3	Density and thickness for different Alq_3 samples.	91
7.4	Density and thickness for different α -NPD samples.	91
9.1	Markov length scale (l_M), deterministic coefficient ($A^{(1)}$) and random noise coefficients ($A^{(2)}, B^{(2)}, C^{(2)}$) for all samples at different substrate temperature and deposition rate.	121

Bibliography

- [1] MITZI, D. B. ; CHONDROUDIS, K. ; KAGEN, C. R.: In: *IBM J. Res. and Dev. , organic electronics* 45 (2001), S. 29
- [2] DRESNER, J.: In: *RCA Rev.* 30 (1969), S. 322
- [3] WAKIMOTO, T. ; OCHI, H. ; KAWAMI, S. ; OHATA, H. ; NAGAYAMA, K. ; MURAYAMA, R. ; OKUDA, Y. ; NAKADA, H. ; TOHMA, T. ; NAITO, T. ; ; ABIKO, H.: In: *J. Soc. Info. Display* 5 (1997), S. 235
- [4] SHAHEEN, S. E. ; JABBOUR, G. E. ; KIPPELEN, B. ; PEYGHAMBARIAN, N. ; ANDERSON, J. D. ; MARDER, S. R. ; R.ARMSTRONG, N. ; BELLMANN, E. ; GRUBBS, R. H.: In: *Appl. Phys. Lett.* 74, 3212 (1999). 74 (1999), S. 3212
- [5] BALDO, M. A. ; LAMANSKY, S. ; BURROWS, P. E. ; THOMPSON, M. E. ; FORREST, S. R.: In: *Appl. Phys. Lett.* 75 (1999), S. 4
- [6] NELSON, S. F. ; LIN, Y. Y. ; GUNDLACH, D. J. ; JACKSON, T. N.: In: *Appl. Phys. Lett* 72 (1998), S. 1854
- [7] DIMITRAKOPOULOS, C. D. ; PURUSHOTHAMAN, S. ; KYMISSIS, J. ; CALLEGARI, A. ; SHAW, J. M.: In: *Science* 283 (1999), S. 822
- [8] FOX, M.: *Optical Properties of Solides.* OXFORD UNIVERSITY PRESS, 2003
- [9] JONES, R. O. ; O.GUNNARSSON: In: *Rev. Mod. Phys.* 61(3) (1989), S. 689
- [10] MARTIN, Richard M.: *Electronic structure: basic theory and practical methods.* Cambridge University Press, 2004
- [11] HARTREE, D. R.: In: *Proceedings of the Cambridge Philosophical Society* 24 (1928), S. 89
- [12] LEVY, M.: In: *Proce. Nat. Acad. Sci.* 76 (1979), S. 6062
- [13] CEPERLEY, D. ; ADLER, B.: In: *Phys. Rev. Lett* 45 (1980), S. 566
- [14] PERDEW, J. P. ; ZUNGER, A.: In: *Phys. Rev. B* 23 (1981), S. 5048
- [15] GOEDECKER, S. ; TETER, M. ; HUTTER, J.: In: *Phys. Rev. B* 54 (1996), S. 1703

-
- [16] GUNNARSSON, O. ; LUNDQVIST, B. I.: In: *Phys. Rev. B* 13 (1976), S. 4274
- [17] GUNNARSSON, O. ; JONSON, M. ; LUNDQVIST, B. I.: In: *Phys. Rev. B*. 20 (1979), S. 3136
- [18] PERDEW, J. P. ; WANG, Y.: In: *Phys Rev. B* 33 (1986), S. 8800
- [19] PERDEW, J. P. ; BRUKE, K. ; ERNZERHOF, M.: In: *Phys. Rev. Lett.* 77 (1996), S. 3865
- [20] VON BARTH, U. ; HEDIN, L.: In: *J. Phys. Chem.* 5 (1972), S. 1629
- [21] CHADI, D. J. ; COHEN, M. L.: In: *Phys. Rev. B* 8 (1973), S. 5747
- [22] JOANNOPOULOS, J. D. ; COHEN, M. L.: In: *J. Phys. C* 6 (1973), S. 1572
- [23] PACK, J.D. ; MONKHORST, H.J.: In: *Phys. Rev. B* 16 (1977), S. 1748
- [24] BACHELET, G.B. .. ; HAMANN, D. .. ; SCHLÜTER, M.: In: *Phys. Rev. B* 26(8) (1982), S. 4199
- [25] HAMANN, D. R. ; SCHLUETER, M. ; CHIANG, C.: In: *Phys. Rev. Lett.* 43 (1979), S. 1494
- [26] BLOECHEL, P. E.: In: *Phys. Rev. B* 41(8) (1990), S. 4514
- [27] KROMEN, W.: *Die Projector Augmented Wave-Methode: Ein schnelles Allelektronenverfahren für die ab-initio-Molekulardynamik*, RWTH Aachen, Diss., 2001
- [28] ENGELS, B.: *Ab initio Berechnung der (110 Oberfläche von II-V Halbleitern: Simulation von Rastertunnelmikroskopie-Aufnahmen*, RWTH Aachen, Diss., 1992
- [29] RICHARD, P.: *Banddiskontinuitäten an III-V Halbleitergrenzflächen : Verspannungsabhängigkeit und Einfluß von Zwischenschichten*, RWTH Aachen, Diss., 1996
- [30] BERGER, R.: *Brechnung von Stufenkanten auf der As-bedeckten Si(111)-Oberflaeche mit einem parallelierten ab initio Programm*, RWTH Aachen, Diss., 2002
- [31] ANTONS, A.: *First Principles investigations of the Initial Stages of Surfactant Mediated Growth on the Si(111) Substrate*, RWTH-Aachen, Diss., 2002
- [32] ATODIRESEI, N.: *First Principles Theory of Organic Molecules on Metal Surfaces: Formate, 3-Thiophene-carboxylate and Glycinate on Cu(110)*, RWTH-Aachen, Diss., 2004
- [33] EWALD., P.P.: In: *Ann. Phys.* 64 (1921), S. 253
- [34] IHM, J. ; ZUNGER, A. .. ; COHEN, M.L.: In: *J. Phys. Chem. : Solid State Physics* 12 (1979), S. 4409

-
- [35] DAVIDSON, W.E.: In: *J. Comput. Phys.* 17 (1975), S. 87
- [36] KOSUGI, N.: In: *J. Comp. Phys.* 55 (1984), S. 426
- [37] FLETCHER, R.: *Practical Methods of Optimization*. John Wiley and sons, New York, 1987
- [38] MALLIARAS, G. G. ; FRIEND, R. H.: In: *Phys. Today* 58 (2005), S. No. 5, 53
- [39] DIMITRAKOPOULOS, C. D. ; MALENFANT, P. R. L.: In: *Adv. Mater* 14 (2002), S. 99
- [40] KOWARIK, S. ; GERLACH, A. ; SELLNER, S. ; SCHREIBER, F. ; CAVALCANTI, L. ; KONOVALOV, O.: In: *Phys. Rev. Lett.* 96 (2006), S. 125504
- [41] FORREST, S.: In: *Chem. Rev.* 97 (1997), S. 1793
- [42] LIU, Xiangdong: *Functional Modification in Ultrathin Films: from Metastable Magnets to Molecular Materials*, RWTH-Aachen, Diss., 2004
- [43] PEISERT, H. ; SCHWIEGER, T. ; AUERHAMMER, J. M. ; KNUPFER, M. ; GOLDEN, M. S. ; FINK, J. ; BRESSLER, P. R. ; MAST, M.: In: *J. App. Phys* 90 (2001), S. 466
- [44] FORREST, S. R. ; BURROWS, P. E.: In: *Supramolecular Science* 4 (1997), S. 127
- [45] CHEN, Q. ; RADA, T. ; MCDOWALL, A. ; RICHARDSON, N. V.: In: *Chemistry of Materials* 14 (2002), S. 743
- [46] ULMAN, A.: *An Introduction to Ultrathin Organic Films from Langmuir-Blodgett to Self-Assembly*. Academic Press, New York, 1991
- [47] FREDERICK, B. G. ; CHEN, Q. ; BARLOW, S. M. ; CONDON, N. G. ; LEIBSLE, F. M. ; RICHARDSON, N. V.: In: *Surface Science* 352 (1996), S. 238
- [48] CHEN, Q. ; FREDERICK, B. G. ; RICHARDSON, N. V.: In: *J. Chem. Phys.* 108 (1998), S. 5942
- [49] CHEN, Q. ; HAQ, S. ; FREDERICK, B. G. ; RICHARDSON, N. V.: In: *Surf. Scien.* 368 (1996), S. 310
- [50] ATODIRESEI, N. ; ET AL: In: *in preperation* (2007)
- [51] BASSANI, Pastori P.: *Electronic States and Optical Transitions in Solids*. Pergamon press
- [52] ABELES, F. (Hrsg.): *Optical Properties of Solids*. North-Holland, 1972

-
- [53] GREENAWAY, D. L. ; HARBEKE, G.: *Optical properties and Band Structure of Semiconductors*. Pergamon Press, 1968
- [54] STERN, F.: In: *Solid State Physics* 15 (1963), S. 300
- [55] ALTARELLI, M. ; DEXTER, D. L. ; M.NUSSENZVEIG, H. ; SMITH, D. Y.: In: *Phys. rev. B* 6 (1972), S. 4502
- [56] M.ALTARELLI ; SMITH, D. Y.: In: *Phys. Rev. B* 9 (1974), S. 1290
- [57] BARDEEN, J. ; BLATT, F. J. ; HALL, A. R.: In: *Photoconductivity Conference* Wiley (1957), S. 146
- [58] ZIMAN, J. M.: *The Principle of the Theory of Solids*. Cambridge University Press, 1972
- [59] DEVOS, A. ; LANNOO, M.: In: *Phys. rev. B* 58 (1998), S. 8236
- [60] MATSUI, A. ; NISHIMURA, H.: In: *J. Phys. Soc. Jap.* 49 (1980), S. 657
- [61] MOELLER, S. ; WEISER, G.: In: *Chemical Physics* 246 (1999), S. 483
- [62] BALDO, M. ; DEUTSCH, M. ; BURROWS, P. ; GOSSENBERGER, H. ; BAN, M. Gerstenberg V. ; FORREST, S.: In: *Adv. Mat.* 10 (1998), S. 1505
- [63] FORREST, S. R.: In: *Nature* 428 (2004), S. 911
- [64] HEUKEN, Michael ; MEYER, Nico: *Review about Organic Vapor Phase Deposition for Organic Electronics*. Wiley-VCH, Weinheim, Germany, 2006
- [65] LAUDISE, R. A. ; BRIDENBAUGH, P. M. ; KLOC, C. ; JOUPPI, S. L.: In: *J. Cryst. Growth* 178 (1997), S. 585
- [66] BURROWS, P. E. ; FORREST, S. R. ; SAPOCHAK, L. S. ; SCHWARTZ, J. ; FENTER, P. ; BUMA, T. ; BAN, V. S. ; FORREST, J. L.: In: *J. Cryst. Growth* 156 (1995), S. 91
- [67] FORREST, S. R. ; BURROWS, P. E. ; STROUSTRUP, A. ; STRICKLAND, D. ; BAN, V. S.: In: *Appl. Phys. Lett.* 68 (1996), S. 1326
- [68] STRINGFELLOW, G. B.: *Organometallic Vapor-Phase Epitaxy*. Academic, London, 1989
- [69] BALDO, M. A. ; KOZLOV, V. G. ; BURROWS, P.E. ; FORREST, S. R. ; BAN, V. S. ; KOENE, B. ; THOMPSON, M.E.: In: *Appl. Phys. Lett.* 71 (1997), S. 3033
- [70] ISRAELACHVIL, J.: *Intermolecular and surface forces*. Academic Pres, 1992
- [71] CALLITY, B. D.: *Elements of x-ray diffraction*. Addison-Wesley, 1978

- [72] FARAHZADI, Azadeh ; BEIGMOHAMADI, Maryam ; NIYAMAKOM, Phenwisa ; KREMERs, Stephan ; MEYER, Nico ; HEUKEN, Michael ; SCHWAB, Holger ; WUTTIG, Matthias: In: *preparation* (2007)
- [73] ONIDA, G. ; REINING, L. ; RUBIO, A.: In: *Rev. Mod. Phys.* 74 (2002), S. 601
- [74] REINING, L. ; OLEVANO, V. ; RUBIO, A. ; ONIDA, G.: In: *Phys. Rev. Lett.* 88 (2002), S. 066404
- [75] THEISS, W.: *SCOUT (Spectroscopic Objects and Utilities), A Windows application*. W.Theiss Hard- and Software, <http://www.mtheiss.com>, 1998
- [76] ERMAN, M. ; THEETEN, J. B. ; VODJDANI, N. ; DEMAY, Y.: In: *Vac. Sci. Technol. B* 1 (1983), S. 328
- [77] KIM, C. C. ; GARLAND, J. W. ; RACCAH, P. M.: In: *Phys. Rev. B* 45 (1992), S. 011749
- [78] BURLAND, D. M. ; COOPER, D. E. ; FAYER, M. D. ; GOCHANAOUR, C.R.: In: *Chem. Phys. Lett.* 52 (1977), S. 279
- [79] TOYOZAWA, Y.: In: *J. Phys. Chem. Solids* 25 (1964), S. 59
- [80] SPANO, F. C.: In: *Annu. Rev. Phys. Chem.* 57 (2006), S. 217
- [81] TOLAN, M.: *X-Ray Scattering from Soft-Matter Thin Films*. Springer tracts in modern physics, Vol. 148, 1999
- [82] BEIGMOHAMADI, Maryam, RWTH-Aachen, Physics 1a, Diss., 2007
- [83] JELLISON, G. E.: In: *Opt. Mater* 1 (1992), S. 41
- [84] ALBERTINI, V. R. ; PACI, B. ; GENEROSI, A.: In: *J. Phys. D : Appl. Phys.* 39 (2006), S. 462
- [85] KRUG, J.: In: *Adv. Phys.* 46 (1997), S. 139
- [86] BAUER, E.: In: *Z. Kristallogr.* 110 (1958), S. 372
- [87] OHRING, Milton: *The materials science of thin films*. ACADEMIC PRESS, INC., 1991
- [88] MICHELY, T. ; KURG, J.: *Island, Mounds and atoms*. Springer, 2003
- [89] STRANSKI, I.N. ; KRASTANOV, L.: In: *Akad. Wien, Math. Nat. Kl. IIb* 146 (1937), S. 797
- [90] TEICHERT, Ch.: In: *Phys. Rep.* 365 (2002), S. 335

- [91] SCHREIBER, F.: In: *Phys. Stat. Sol. (a)* 201 (2004), S. No. 6, 1037
- [92] BARABASI, A. L. ; STANLEY, H. E.: *Fractal concepts in Surfaces Growth* (Cambridge University Press, New York, 1995). Cambridge University Press, New York, 1995
- [93] KARDAR, Mehran ; PARISI, Giorgio ; ZHANG, Yi-Cheng: In: *Phys. Rev. Lett.* 56 (1986), S. 889
- [94] MARSILLI, M. ; MARITAN, A. ; TOIGOEND, F. ; BANAVAR, J. R.: In: *Rev. Mod. Phys.* 68 (1996), S. 963
- [95] RAIBLE, Martin ; LINZ, Stefan J. ; HÄNGGI, Peter: In: *Phys. Rev. E* 64 (2001), S. 031506
- [96] WEEKS, J. D. ; GILMER, G. H. ; JACKSON, K.: In: *J. Chem. Phys.* 65 (1976), S. 712
- [97] EDWARDS, S. F. ; WILKINSON, D. R.: In: *Proc. R. Soc. London A* 381 (1982), S. 17
- [98] RAIBLE, Martin ; LINZ, Stefan J. ; HÄNGGI, Peter: In: *Phys. Rev. E* 62 (2000), S. 1691
- [99] RAIBLE, M. ; MAYR, S. G. ; LINZ, S. J. ; MOSKE, M. ; HÄNGGI, P. ; SAMWER, K.: In: *Euro. Phys. Lett.* 50 (2000), S. 61
- [100] JAFAR, G. R. ; FAZELI, S. M. ; GHASEMI, F. ; ALLAEI, S. M. V. ; TABAR, M. R. R. ; ZAD, A. I. ; KAVEI, G.: In: *Phys. Rev. Lett.* 91 (2003), S. 226101
- [101] SANGPOUR, P. ; JAFARI, G. R. ; AKHAVAN, O. ; MOSHFEGH, A. Z. ; TABAR, M.R. R.: In: *Phys. Rev. B* 71 (2005), S. 155423
- [102] GHASEMI, F. ; PEINKE, J. ; SAHIMI, M. ; TABAR, M.R. R.: In: *Eur. Phys. J. B* 47 (2005), S. 411
- [103] FRIEDRICH, R. ; PEINKE, J. ; RENNER, C.: In: *Phys. Rev. Lett.* 84 (2000), S. 5224
- [104] FRIEDRICH, R. ; PEINKE, J.: In: *Phys. Rev. Lett.* 78 (1997), S. 863
- [105] FRIEDRICH, R. ; GALLA, Th. ; NAERT, A. ; PEINKE, J. ; SCHIMME, Th. ; J. PARISI (Hrsg.) ; MULLER, S.C. (Hrsg.) ; ZIMMERMANN, W. (Hrsg.): *A Perspective Look at Nonlinear Media*. Springer, Berlin, 1997
- [106] RISKEN, H.: *H. Risiken*. Springer, Berlin, 1984
- [107] FARAHZADI, A. ; NIYAMAKOM, P. ; BEIGMOHAMADI, M. ; GHASEMI, F. ; MEYER, N. ; KEIPER, D. ; HEUKEN, M. ; SCHWAB, H. ; TABAR, M. R. R. ; MICHELY, T. ; WUTTIG, M.: In: *preparation* (2007)

-
- [108] YANG, F. ; SHTEIN, M. ; FORREST, S. R. F.: In: *J. App. Phys.* 98 (2005), S. 014906
- [109] NIYAMAKOM, P. ; BEIGMOHAMADI, M. ; FARAHZADI, A. ; JESSEN, F. ; KALISCH, H. ; JANSEN, R. ; N. ; MEYER ; KEIPER, D. ; KUNAT, M. ; HEUKEN, M. ; EFFERTZ, C. ; SCHULZ, P. ; SCHWAB, H. ; MICHELY, T. ; WUTTIG, M.: In: *preparation* (2007)
- [110] BEIGMOHAMADI, M.: *Growth, structure and morphology of organic thin films*, RWTH-Aachen, Diss., 2007
- [111] BASSANI, F.: in Proceeding of the International School of physics "Enrico Fermi" (Academic Press, 1968), vol 34, P. 33
- [112] FEHRENBACH, G. W. ; SCHAEFER, W. ; ULBRICH, R. G.: In: *J. Luminescence* 30 (1985), S. 154
- [113] SHTEIN, M. ; GOSSENBERGER, H. F. ; BENZIGER, J. B. ; FORREST, S. R.: In: *J. App. Phys.* 89 (2001), S. 1470
- [114] STRANSKI, I.N. ; KRASTANOV, L.: In: *erratum, ibid* 147 (1938), S. 153

Acknowledgments

This work would not have been possible without the contributions from many people. Therefore, I am deeply indebted to them all and I would like to take this opportunity to acknowledge them.

In particular I would like to express my sincere thanks to my supervisor Prof. Dr. Matthias Wuttig for giving me the supportive encouragement and permission to work on my PhD research for the last three and a half years at the institute of physics (IA) at RWTH-Aachen, Germany. I am grateful to his continuous and trustful support, including many important suggestions and constructive ideas during the whole period of this work. Moreover, I would like to express my appreciation towards him for a lot of warm-hearted help and understanding all along this exciting and inspiring time. I have learnt a lot from him.

I would like to express my special thanks to Prof. Dr. Stefan Blügel for examining my thesis, his guidance and suggestions and for giving me the opportunity to spend one year of my PhD work at the institute of solid state research (IFF-Th1) in research center Jülich, where I have become familiar with the density functional theory.

I am also indebted to Prof. Dr. Thomas Michely for many helpful discussions about thin film growth and for his supportive help and fruitful suggestions.

My warm thanks pass towards Prof. Dr. M. Reza Rahimi-Tabar for his great help and guidance, being supportively continuous from my Bachelor and Master studies up to now and still never-endingly showering me with many new creative ideas.

My special warm thanks go to my friends, colleagues and the best officemates ever, Phen-wisa Niyamakom and Maryam Beigmohamadi. Our friendly, energetic, motivating and instructive discussions on scientific, social, cultural and many other different interesting issues have been the main inspiration for my daily work and finally for this thesis.

A special thank goes to everyone who contributed to this work by their assistances and guidance: in Aachen, to the organic group members, for their great atmosphere and team work, their kind supports and useful discussions. I would like to specially thank Stephan Kremers, Christian Effertz and Philip Schulz. In Jülich in particular to Prof. Kurt Schröder and Nicolae Atodiresei for introducing me into plane wave methods and the EStCoMPP code. From Sharif University to Fatemeh Ghasemi and M. Dehghan Niri for their instructive discussions about statistical analysis of surface morphology. Among the members of the FONO project, to Prof. M. Heuken, Dr. H. Schwab, Dr. D. Bertram, Dr. N. Meyer, Dr. D. Keiper and F. Jessen for the several discussions, introducing me to OVPD system and their assistance in sample preparation.

I would like to thank all the institute members whom I had the pleasure to work with in the last three and a half years, Aachen: Julia Steiner, Christoph Steimer, Martin

Salinga, Kyung-Min Chung, Fahri Uslu, Daniel Wamwangi, Kostas Sarakions, Daniel Klöckner, Christian Klever, Daniel Severin, Henning Dieker, Wojciech Welnic, Stephan Hermes, Michael Huppertz, Oliver Lehmann and Josefine Elbert, and Jülich: Samir Lounis, Manfred Niesert, Marjana Lezaic, Daniel Wortmann, Phivos Mavropoulos, Christoph Friedrich, Ute Winkler and Gustav Bihlmayer.

Moving to another country is an experience that could have been more challenging without the great help and accompany of the best friends and the family. Among them, I would like to start to thank from dear Sara Farahzadi, for all her kind warm-hearted support and for the unique aunt-friendship experience that we have from the 1st of January 2004, the exact date of my arrival to Cologne-Bonn international airport. Subsequently, I would like to thank Shahin Rajinia and Cyrus Gordji-nejad, for all their sympathy during the last two years. My special thanks go to the friends together with whom we have experienced living in a new country, Maryam Beigmohamadi and Mohammad Amiri. I have always been grateful, happy and feeling safe to have them here. I would definitely thank all friends who have assisted me in different crucial situations, especially Colette Knight for her kind help during the first days and Thorsten Auth for all his gentle supportive manner.

Till now, I have thanked who helped me getting through these years. I would like to honourably mention those who have spent all the precious time of their life to light up my life, my dearest parents Behjat Golar and Hossein Farahzadi, to whom I dedicate this thesis. I would gratefully pass forwards my appreciation to them for all their incredible efforts, motivation, support, love and compassion, including the special thanks to my brother, Sina Farahzadi, whose eagerness has been the best encouragement for me through my work.

Last and the best: the PhD journey that I started alone at the first day of the year 2004, was finally being accompanied with the love of my life, Ali Gordji-nejad, to whom my heartfelt admiration and gratitude goes. His passion, great support and patience during all the happy and tough moments of my PhD phase was the best motivation for my work as well as the invaluable experience of my life.

Curriculum Vitae

Azadeh Farahzadi

Date and place of birth:	9 April 1979	Ray, IRAN
Marital status:	Married	
9/1992-6/1996 :	Farzanegan High School	under the supervision of NODET (National Organization for Development of Exceptional Talents) Karaj, Tehran, IRAN
	High School diploma	Mathematics and Physics
9/1996 - 1/2001:	Sharif University of Technology Physics Department	Tehran, IRAN
	B.Sc. degree	Solid State Physics
9/2001 - 9/2003:	Iran University of Science and Technology Physics Department	Tehran, IRAN
	M.Sc. degree	Solid State Physics Thesis: The 2-dimensional Anderson localization
1/2004-	RWTH-Aachen Physics Institute (IA)	Aachen, GERMANY
	PhD degree	

